

ABSTRACT

Title of Document: KINETICS AND MORPHOLOGY OF
METALLOCENE CATALYZED
SYNDIOSPECIFIC POLYMERIZATION OF
STYRENE IN HOMOGENEOUS AND
HETEROGENEOUS REACTION SYSTEMS

Joong Jin Han, Doctor of Philosophy, 2008

Directed By: Professor Kyu Yong Choi
Department of Chemical and Biomolecular
Engineering

Syndiotactic polystyrene (sPS) is a semicrystalline thermoplastic polymer with many advantageous properties such as excellent heat resistance with a high melting point of 270-272°C, strong chemical resistance against acids, bases, oils and water, and low dielectric constant. The relatively fast crystallization rate makes sPS a promising material for a large number of applications in the automotive, electrical and packaging industries.

In this study, the kinetics of syndiospecific polymerization of styrene is investigated through experimentation and theoretical modeling using homogeneous and heterogeneous $\text{Cp}^*\text{Ti}(\text{OCH}_3)_3/\text{MAO}$ catalysts. During sPS slurry polymerization, the physical phase changes of reaction mixture occur. With an increase in total solid content, sPS slurry undergoes a series of physical changes from clear liquid to a wet

cake or paste-like material. A detailed reaction kinetic model based on a two-site kinetic mechanism has been developed to predict the polymerization rate and polymer molecular weight distribution. The monomer partition effect is incorporated into kinetic models to account for the nonlinear dependence of polymerization rate on the bulk phase monomer concentration. Quite satisfactory agreement between the model simulation results and experimental data has been obtained.

The morphological development of nascent sPS particles during the polymerization has also been investigated. Most notably, it was found that sPS particles grow with the nanofibrillar morphology with either homogeneous or silica-supported metallocene catalyst. The analysis of nascent morphology of sPS using X-ray diffraction (XRD), scanning electron microscopy (SEM), and energy dispersive X-ray (EDS/EDX) analysis, revealed that there is a strong correlation between the formation of sPS nanofibrillar structure and sPS crystallization. A mechanism for the growth of sPS particles is also proposed based on the experimental observations and analysis.

Ultrahigh molecular weight sPS has also been synthesized in silica nanotube reactors (SNTRs) and the morphological characteristics of sPS produced in the nanotube reactors have been analyzed. A new mechanism is proposed for the formation and growth of sPS nanofibrils extruding out from the nanotube reactors. Also, a kinetic analysis is presented to interpret the observed molecular weight enhancement effect that is believed to be caused by the constrained reaction environment inside the nanotubes.

KINETICS AND MORPHOLOGY OF METALLOCENE CATALYZED
SYNDIOSPECIFIC POLYMERIZATION OF STYRENE IN HOMOGENEOUS
AND HETEROGENEOUS REACTION SYSTEMS

By

Joong Jin Han

Dissertation submitted to the Faculty of the Graduate School of the
University of Maryland, College Park, in partial fulfillment
of the requirements for the degree of
Doctor of Philosophy
2008

Advisory Committee:
Professor Kyu Yong Choi, Chair
Professor F. Joseph Schork
Professor Richard V. Calabrese
Professor Chunsheng Wang
Professor Bongtae Han

© Copyright by
Joong Jin Han
2008

Acknowledgements

I would like to express my deep and sincere gratitude to my advisor, Prof. Kyu Yong Choi for his guidance and support throughout the study. His novel idea and enthusiasm made my study successful. I wish to express my sincere thanks to Prof. Sang Bok Lee for his invaluable advice. With his support, I could successfully finish my study. I also would like to thank thesis committee, Profs. F. Joseph Schork, Richard Calabrese, Chunsheng Wang, and Bongtae Han for their valuable suggestion and advice of this project.

I am thankful to my lab mates, Yuesheng Ye, Yunju Jung, Inhak Baick, and Carla Luciani and visiting scholars, Yong Jeon Kim, Sung Won Kim, Kyu Hwang Lee, and Hyung Joong Kim. I also express my thanks to Dr. Hyung Woo Lee for his help and advice during my initial startup of this study. The supports from all the faculties and staffs in the department of Chemical & Biomolecular Engineering are gratefully appreciated. I am truly thankful to Korean friends in the department of Chemical & Biomolecular Engineering who helped and supported me in many ways. Financial support during my PhD study at the University of Maryland from LG Chemical Co., Ltd. is very much appreciated.

My deepest gratitude goes to my family in Korea. Thank my parents, Eungtae Han and Jungsook Oh, for their endless love and support throughout my life.

Table of Contents

Acknowledgements	ii
Table of Contents	iii
List of Tables	v
List of Figures	vi
Chapter 1: Introduction	1
1.1 Background and Motivations	1
1.1.1 Syndiotactic polystyrene	1
1.1.2 Synthesis of syndiotactic polystyrene	4
1.1.3 Polymorphism of syndiotactic polystyrene	10
1.1.4 Thermoreversible gelation	14
1.2 Research Objectives	16
Chapter 2: Kinetics of Syndiospecific Polymerization of Styrene over Homogeneous Metallocene Catalysts	18
2.1 Introduction	18
2.2 Experimental	21
2.2.1 Materials	21
2.2.2 Styrene polymerization with homogeneous metallocene catalyst	25
2.3 Results and Discussion	26
2.3.1 Polymerization Rate Analysis	26
2.3.2 Physical transitions during sPS polymerization	34
2.3.3 Modified polymerization model for sPS polymerization over homogeneous catalyst	39
2.4 Conclusions	44
Chapter 3: Kinetics of Syndiospecific Polymerization of Styrene over Heterogeneous Metallocene Catalysts	46
3.1 Introduction	46
3.2 Experimental	48
3.2.1 Materials	48
3.2.2 Preparation of silica-supported metallocene catalysts	51
3.2.3 Styrene polymerization with silica-supported Cp*Ti(OCH ₃) ₃ /MAO catalyst	52
3.3 Results and Discussion	55
3.3.1 Polymerization rate analysis	55
3.3.2 Physical changes during polymerization	70
3.3.3 Molecular weight distribution analysis	80
3.3.4 Two-site model	86
3.4 Conclusions	93
Chapter 4: Nascent Morphology of Syndiotactic Polystyrene in Homogeneous and Heterogeneous Reaction Systems	95
4.1 Introduction	95
4.2 Experimental	98
4.3 Results and Discussion	100

4.3.1 Particle morphology	100
4.3.2 Crystalline structure of sPS	110
4.3.3 Macroscopic growth of sPS particles synthesized over silica-supported metallocene catalyst	118
4.3.4 Particle growth mechanism in silica-supported catalyst system	124
4.4 Conclusions	127
Chapter 5: Syndiotactic Polystyrene Nanofibrils in Silica Nanotube Reactors	128
5.1 Introduction	128
5.2 Experimental	133
5.2.1 Preparation of silica nanotube reactor (SNTR)	133
5.2.2 Polymerization in SNTRs	136
5.2.3 Polymer analysis	137
5.3 Results and Discussion	138
5.3.1 Morphology and properties of sPS synthesized in SNTRs	138
5.3.2 Modeling of monomer diffusion and reaction in SNTRs	155
5.3.3 Modeling of molecular weight distribution (MWD)	158
5.4 Conclusions	166
Chapter 6: Summary	168
Bibliography	170

List of Tables

Table 1.1 Three different stereo-isomers of polystyrene: structures and properties	2
Table 1.2 Physical properties of sPS in comparison with PS and PMMA [5]	4
Table 1.3 Density and crystal cell dimensions of sPS polymorphs [36, 37].....	14
Table 2.1 syndiotactic polystyrene polymerization with different types of catalysts	19
Table 2.2 Yields and polymerization rates of syndiospecific polymerization of styrene over homogeneous metallocene catalyst	27
Table 2.3 Initial polymerization rates at different catalyst concentrations	30
Table 2.4 sPS polymerization experimental data for physical phase change in an agitated reactor.....	35
Table 2.5 The solubility parameters of reaction mixture	36
Table 3.1 Reaction conditions and experimental data of sPS polymerization with silica-supported metallocene catalyst	56
Table 3.2 Solubility parameters of solvents, styrene monomer [74]	71
Table 3.3 sPS polymerization data in different solvents.....	73
Table 3.4 Adsorption experimental data	76
Table 3.5 The reaction rate constants (single site).	83
Table 3.6 Two-site model parameters.	90
Table 4.1 Solvents used for crystallization and the morphology of sPS films.....	97
Table 4.2 Experimental sPS polymerization data	99
Table 4.3 Polymerization and re-crystallization conditions for making crystalline sPS film.....	100
Table 4.4 Degree of crystallinity and melting temperature of sPS produced over silica-supported catalyst.....	113
Table 4.5 Turnover frequency of silica-supported catalyst.....	124
Table 5.1 Basic properties of anodized aluminum oxide (AAO) porous film	134
Table 5.2 Reaction conditions of sPS polymerization in SNTRs	137
Table 5.3 the model parameters for MWD calculation.....	162
Table 5.4 MWD calculation without chain transfer rate constant change	162
Table 5.5 MWD calculation with chain transfer constant rate change	166

List of Figures

Figure 1.1 The properties and applications of syndiotactic polystyrene (sPS).....	3
Figure 1.2 Examples of Ti based metallocene catalysts for sPS polymerization.	5
Figure 1.3 The mechanism of active site formation in syndiospecific polymerization of styrene; R: alkyl [8].	6
Figure 1.4 Steric control in propagation of syndiospecific polymerization of styrene [1].	8
Figure 1.5 Syndiotactic polystyrene conformations; (b) and (c): drawing based on Materials Studio® modeling package (Accelrys Software Inc.).	11
Figure 1.6 Summary of the polymorphic structures of sPS. [35]	13
Figure 1.7 Thermoreversible gel of sPS; toluene is used as solvent.	15
Figure 2.1 Styrene monomer purification apparatus and procedure; (a) solvent purification system, (b) styrene and calcium hydride in the three-neck flask, (c) styrene distillation, (d) styrene transfer to a storage bottle.	23
Figure 2.2 Solvent purification apparatus and procedure; (a) solvent purification system, (b) loading of solvent, sliced sodium, and benzophenone into the three-neck flask, (c) purified solvent.	24
Figure 2.3 monomer conversion profiles vs. reaction time at different initial monomer concentrations.	28
Figure 2.4 Initial polymerization rate vs. initial monomer concentrations ($T = 70^{\circ}\text{C}$, $[\text{Ti}] = 0.165 \text{ mmol-Ti/L}$, $\text{Al/Ti mol ratio} = 500$, symbol: experimental data, line: regression result).	29
Figure 2.5 Initial polymerization rate vs. initial catalyst concentrations (bulk polymerization, $[\text{M}]_{\text{b}0} = 8.73 \text{ mol/L}$, $T = 70^{\circ}\text{C}$, $\text{Al/Ti} = 500$).	31
Figure 2.6 Propagation rate constant vs. initial monomer concentration ($T = 70^{\circ}\text{C}$, $[\text{Ti}] = 0.165 \text{ mmol-Ti/L}$, $\text{Al/Ti mol ratio} = 500$).	32
Figure 2.7 (a) Modified polymerization rate changes, (b) effective propagation rate constant with reaction time, solid curve: the exponential regression curve; $T = 70^{\circ}\text{C}$, $[\text{Ti}] = 0.165 \text{ mmol-Ti/L}$, $\text{Al/Ti mol ratio} = 500$	33
Figure 2.8 Physical phase changes of reaction mixture with different initial styrene to <i>n</i> -heptane ratio (Homogeneous reaction system, $\text{st/hep} = \text{v/v ratio}$, $T = 70^{\circ}\text{C}$, $[\text{Ti}] = 0.160 \text{ mmol/L}$, $\text{Al/Ti} = 500$).	38
Figure 2.9 Physical phase changes during sPS polymerization over homogeneous catalyst, diluent = <i>n</i> -heptane, $[\text{M}]_0 = 5.02 \text{ mol/L}$, $[\text{Ti}] = 0.16 \text{ mmol-Ti/L}$, $T = 70^{\circ}\text{C}$	39
Figure 2.10 Polymerization rate analyses by adopting sorption kinetics; (a) Test of eq. (2-7), (b) Initial polymerization rate vs. initial monomer concentration (line: model calculation from eq. (2-6)).	42
Figure 2.11 Test of eq. (2-9)	43
Figure 2.12 Polymer yields vs. reaction time (symbols: experimental data, lines: simulation results).	44
Figure 3.1 Methods for supporting metallocenes. [69]	48
Figure 3.2 (a) SEM image of Davison 952 silica gel particle and (b) the pore size distribution (Courtesy of W.R. Grace and Company).	50

Figure 3.3 Mechanism of supporting step of $\text{Cp}^*\text{Ti}(\text{OCH}_3)_3$ on silica pretreated with MAO ($\text{X} = \text{CH}_3$).	51
Figure 3.4 Preparation of silica-supported catalyst.....	53
Figure 3.5 The schematic diagram of 100 mL glass reactor system.....	54
Figure 3.6 Effect of initial monomer concentration on polymer yield, monomer conversion, and polymerization rate at 70 °C (symbols - data (●, 0.81 mol/L; ○, 2.02 mol/L; ▼, 3.24 mol/L; Δ, 4.86 mol/L), lines - model).....	58
Figure 3.7 Initial polymerization rates vs. initial monomer concentration (■, data; dashed line, model calculations from eq. (3-20)).....	59
Figure 3.8 Polymerization rate vs. initial catalyst concentration ($[\text{M}]_{\text{b}0} = 2.03$ mol/L, Reaction time = 15 min, $T = 70^\circ\text{C}$, $\text{Al/Ti} = 350$).....	60
Figure 3.9 Polymer yield profiles vs. reaction time calculated with reversible active site formation mechanism (lines: simulation results, symbols: experimental data). ..	66
Figure 3.10 Test of eq. (3-27).	68
Figure 3.11 photo-images of phase changes during sPS polymerization in different solvents with silica-supported $\text{Cp}^*\text{Ti}(\text{OCH}_3)_3/\text{MAO}$ catalyst.	72
Figure 3.12 Schematic illustration of the sPS slurry polymerization process.	74
Figure 3.13 The photographs of physical phases of a polymerization mixture (a) TSC = 0.8 w/w %; (b) TSC = 3.6 w/w%; (c) TSC = 8.71 w/w% (d) TSC = 12.4 w/w%; (e) TSC = 20.5 w/w% (f) TSC = 19.1 w/w%.	75
Figure 3.14 The amount of styrene- <i>n</i> -heptane mixture absorbed in sPS polymer ($T = 70^\circ\text{C}$; ●, data; line, regression).....	77
Figure 3.15 (a) The volume fraction of liquid phase vs. reaction time; (b) the TSC profiles vs. reaction time (symbols - data (●, 0.81 mol/L; ○, 2.02 mol/L; ▼, 3.24 mol/L; Δ, 4.86 mol/L), lines - model).....	79
Figure 3.16 sPS molecular weight profiles for $[\text{M}]_{\text{b}0} = 3.24$ mol/L (symbols - experimental data, lines - model: dashed lines - \bar{M}_w).	81
Figure 3.17 Polymer molecular weights at different monomer concentrations (reaction time = 30 min; symbols - data, lines - model).	82
Figure 3.18 Plot of eq. (3-35) to determine rate constants (experimental data at reaction time = 30 min).....	84
Figure 3.19 The surface groups of silica gel and the complexes of MAO and the surface groups of silica [72, 85, 86].....	87
Figure 3.20 Experimental and model-predicted molecular weight distribution curves for $[\text{M}]_{\text{b}0} = 3.24$ mol/L, $t = 30$ min, symbols - data).....	91
Figure 3.21 Experimental and model-predicted molecular weight distribution curves at different initial monomer concentration ($t = 30$ min, symbols – data).	92
Figure 4.1 SEM images of sPS film produced by solvent induced crystallization: solvent: chloroform.	101
Figure 4.2 SEM images of sPS produced over homogeneous catalyst: (a) and (b) $[\text{M}]_0 = 3.49$ mol/L, reaction time = 10 min, (c) $[\text{M}]_0 = 3.49$ mol/L, reaction time = 30 min, (d) $[\text{M}]_0 = 5.24$ mol/L, reaction time = 10 min, (e) $[\text{M}]_0 = 2.14$ mol/L, reaction time = 10 min, (f) $[\text{M}]_0 = 6.98$ mol/L, reaction time = 10 min.	103

Figure 4.3 SEM images of sPS particle cross-sections: homogenous catalyst system, (a) and (b) $[M]_0 = 3.49$ mol/L, $T = 70^\circ\text{C}$, reaction time = 10 min, (c) and (d) $[M]_0 = 5.24$ mol/L, $T = 70^\circ\text{C}$, reaction time = 60 min.....	104
Figure 4.4 SEM images of sPS particle produced over silica-supported $\text{Cp}^*\text{Ti}(\text{OCH}_3)_3/\text{MAO}$ catalyst in <i>n</i> -heptane: pore size of silica gel = 20nm; (a)-(c), $[M]_0 = 4.71$ mol/L, reaction time = 2 min; (d), $[M]_0 = 4.86$ mol/L, reaction time = 10 min.	106
Figure 4.5 SEM images of sPS particle cross-sections: pore size of silica gel = 20nm, $[M]_0 = 4.86$ mol/L, $T = 70^\circ\text{C}$, reaction time = 10 min; (a) fractured sPS particle, (b) particle interior, (c) edge portion of the sPS particle, (d) close-up of the particle surface.	108
Figure 4.6 SEM images of sPS produced over silica-supported $\text{Cp}^*\text{Ti}(\text{OCH}_3)_3/\text{MAO}$ catalyst having smaller pore size: pore size of silica gel = 6nm, $[M]_0 = 3.24$ mol/L, reaction time = 30 min.	110
Figure 4.7 2_1 -helix of a single sPS chain with 1000 styrene units: drawing based on Materials Studio [®] modeling package (Accelrys Software Inc.).	112
Figure 4.8 DSC thermograms of the sPS; (a) homogeneous $\text{Cp}^*\text{Ti}(\text{OCH}_3)_3/\text{MMAO}$ catalyst, $[M]_0 = 8.73$ mol/L, reaction time = 30 min, (b) silica-supported $\text{Cp}^*\text{Ti}(\text{OCH}_3)_3/\text{MAO}$ catalyst: pore size of silica gel = 20nm, $[M]_0 = 4.86$ mol/L, reaction time = 60 min.	115
Figure 4.9 XRD patterns of sPS particles (a) homogeneous $\text{Cp}^*\text{Ti}(\text{OCH}_3)_3/\text{MMAO}$ catalyst, $[M]_0 = 8.73$ mol/L, reaction time = 60 min, (b) silica-supported $\text{Cp}^*\text{Ti}(\text{OCH}_3)_3/\text{MAO}$ catalyst: pore size of silica gel = 20nm, $[M]_0 = 2.03$ mol/L, reaction time = 60 min	116
Figure 4.10 TGA thermograms of nascent sPS samples synthesized over silica-supported $\text{Cp}^*\text{Ti}(\text{OCH}_3)_3/\text{MAO}$ catalyst in <i>n</i> -heptane: pore size of silica gel = 20nm, reaction time = 60 min.	117
Figure 4.11 SEM images of silica gel and sPS particles: (a) Davison 952 silica gel, (b) polymerized sPS particles, $[M]_0 = 2.02$ mol/L, reaction time = 60 min.	119
Figure 4.12 SEM images of fractured sPS particles: (a)-(b), pore size of silica gel = 20nm, $[M]_0 = 4.71$ mol/L, reaction time = 2 min; (c)-(f), pore size of silica gel = 6nm, $[M]_0 = 3.24$ mol/L, reaction time = 30 min.	121
Figure 4.13 Element distribution mappings of a fractured sPS particle produced over silica-supported $\text{Cp}^*\text{Ti}(\text{OCH}_3)_3/\text{MAO}$ catalyst: pore size of silica gel = 20nm, $[M]_0 = 4.86$ mol/L, Reaction time = 10 min: (a), SEM image; (b) Si mapping; (c) Al mapping.....	123
Figure 5.1 Polymer nanofiber formation mechanism with mesoporous silica fiber [142, 143].....	130
Figure 5.2 Scheme of the synthesis of sPS nanofibrils in catalyst-anchored silica nanotube reactors.	132
Figure 5.3 SEM images of AAO porous membranes: (a) commercial membrane (pore diameter: 200 nm, pore height: 60 μm , (b) homemade membrane (pore diameter: 80 nm, pore height: 3 μm	135
Figure 5.4 white sPS polymers emerging from the SNTR films	138
Figure 5.5 SEM images of sPS nanostructures: (a) vertical cross-section of the polymer layer on the SNTR film surface, Run ID: C-4, (a1) top-down view of sPS	

nanofibrils extruded out from SNTR channels after polymer layer was removed, (a2) sPS fibrils in the vertical cross-sectional view of the polymer layer, (a3) top-down view of the surface of the polymer layer, (b) vertical cross-section of the polymer-filled nanopore channels, Run ID: C-3, scale bars: 20 for (a), 500 nm for (a1), (a2), and (a3), 5 μm for (b).....	140
Figure 5.6 SEM photographs of polyethylene synthesized over a bare AAO film deposited with a $\text{TiCl}_4/\text{Al}(\text{C}_2\text{H}_5)_3$ catalyst with gas phase polymerization; (a) top-view, (b) side view, (c) side view of AAO film [154].....	142
Figure 5.7 SEM images of sPS nanofibrils inside SNTR pores of diameter 200 nm: (a) low catalyst activity without MAO treatment, Run ID: C-5; (b) high catalyst activity with MAO treatment, Run ID: C-3, scale bars: 500 nm.	144
Figure 5.8 SEM images of sPS nanostructures synthesized in a 60-nm SNTR film, Run ID: H-1, (a) vertical cross-section of the SNTR film, pore diameter = 60 nm, (b, c) magnified images. The cartoon in the top left corner illustrates the viewing angles for the images (a)-(c). The polymer layer on the SNTR film and the sPS nanofibrils are omitted for clarity, scale bars: 5 μm for (a), 2 μm for (b), 250 nm for (c).....	146
Figure 5.9 Transmission electron micrographs (TEM) of 60 nm diameter silica nanotubes containing sPS polymerized at the inner surface of the pore walls, Run ID: H-2, scale bars: 250 nm for (a) and (b), 100 nm for (c).....	148
Figure 5.10 ^{13}C NMR spectrum of sPS nanofibrils,	149
Figure 5.11 Molecular weight distributions of sPS: SNTR (200 nm), Run ID: C-2, $M_n = 275,000$ g/mol, $M_w = 928,000$ g/mol (solid line); silica-supported catalyst, $[\text{M}]_0 = 3.24$ mol/L, reaction time = 60 min, $M_n = 68,400$ g/mol, $M_w = 221,000$ g/mol (dotted line).	150
Figure 5.12 DSC thermograms of sPS: (a) SNTR, Run ID: C-1, (b) silica supported catalyst, $[\text{M}]_0 = 4.86$ mol/L, reaction time = 10 min, and (c) homogeneous catalyst, $[\text{M}]_0 = 3.42$ mol/L, reaction time = 10 min.	152
Figure 5.13 XRD patterns of sPS samples: (a) sPS nanofibrils synthesized in 200-nm SNTR, Run ID: C-1 (b) sPS particles synthesized over silica-supported catalyst, $[\text{M}]_0 = 2.03$ mol/L, reaction time = 60 min (c) sPS particle synthesized with homogeneous catalyst, $[\text{M}]_0 = 8.74$ mol/L, $T = 50^\circ\text{C}$, reaction time = 60 min.....	154
Figure 5.14 Monomer concentration profile in SNTR pore; $[\text{M}]_0 = 2.53$ mol/L, Commercial SNTR; pore diameter: 200 nm, pore length: 60 μm , (a) 3D plot of monomer concentration, (b) monomer concentration at the center of a pore, (c) monomer concentration along the pore depth.....	159
Figure 5.15 Monomer concentration profile in an SNTR pore; $[\text{M}]_0 = 2.53$ mol/L, Homemade SNTR; pore diameter: 60 nm, pore length: 5 μm , (a) 3D plot of monomer concentration, (b) monomer concentration at the center of a pore, (c) monomer concentration along the pore depth.	160
Figure 5.16 Schematic diagram of sectioning method.....	161
Figure 5.17 Molecular weight distributions of sPS in SNTR, no chain transfer constants change; experimental results, $M_n = 275,000$ g/mol, $M_w = 928,000$ g/mol (symbol); simulation result, $M_n = 41,400$ g/mol, $M_w = 156,000$ g/mol (line).	163
Figure 5.18 Molecular weight distributions of sPS in SNTR, chain transfer change, $k_t' = 0.065k_t$; experimental results, $M_n = 275,000$ g/mol, $M_w = 928,000$ g/mol (symbol); simulation result, $M_n = 209,000$ g/mol, $M_w = 908,000$ g/mol (line).	164

Figure 5.19 Molecular weight distributions of sPS in SNTRs, chain transfer change, $k_t' = 0.065k_t$; homemade, $M_n = 209,000$ g/mol, $M_w = 908,000$ g/mol (solid line); commercial, $M_n = 566,000$ g/mol, $M_w = 1,189,000$ g/mol (dashed line). 165

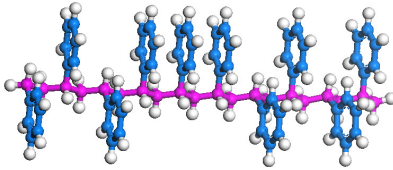
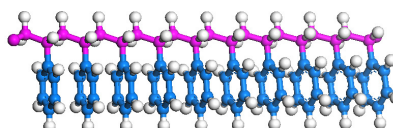
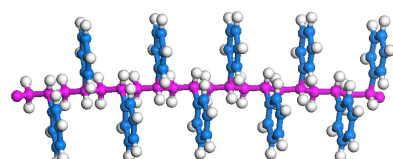
Chapter 1: Introduction

1.1 Background and Motivations

1.1.1 Syndiotactic polystyrene

There are three different stereo-isomers of polystyrene illustrated in Table 1.1. The phenyl groups in atactic polystyrene (aPS), or general purpose polystyrene, are randomly distributed to the main polymer backbone. aPS is an amorphous polymer and one of the most widely used commodity polymers because of its good transparency, stiffness, and good processibility. aPS was firstly commercialized by IG Farben [1]. In isotactic polystyrene (iPS), phenyl groups are on the same side of the backbone chain plane. iPS can be synthesized over Ziegler-Natta catalysts. iPS is a semi-crystalline polymer with a melting point of around 240 °C. Because of very slow crystallization rate, iPS is little used to make injection moldable objects [2]. In syndiotactic polystyrene (sPS), phenyl groups alternate vertically along the backbone chain. sPS is a semi-crystalline polystyrene that can be synthesized over metallocene catalysts in conjunction with methylaluminoxane (MAO).

Table 1.1 Three different stereo-isomers of polystyrene: structures and properties

		T_g	T_m	Crystallinity
Atactic		100 °C	-	Amorphous
Isotactic		100 °C	240 °C	20 ~ 30 % (Slow Crystallization)
Syndiotactic		100 °C	270 °C	40 ~ 50 % (Fast Crystallization)

sPS was firstly synthesized in 1985 by Idemitsu Kosan Co. Ltd. (Tokyo, Japan). Figure 1.1 shows the properties and possible applications of sPS. sPS has low specific gravity, high modulus, good electrical properties, high melting point (270 °C), strong chemical resistance, and dimensional stability. Table 1.2 illustrates physical properties of reinforced sPS in comparison with PS and poly (methyl methacrylate) (PMMA). The fast crystallization rate makes sPS a promising material for a large number of applications such as in the automotive, electrical, and packaging industries [1-4]. As sPS is brittle like aPS, sPS can be reinforced with impact modifiers such as glass fibers to improve the impact resistance and toughness.

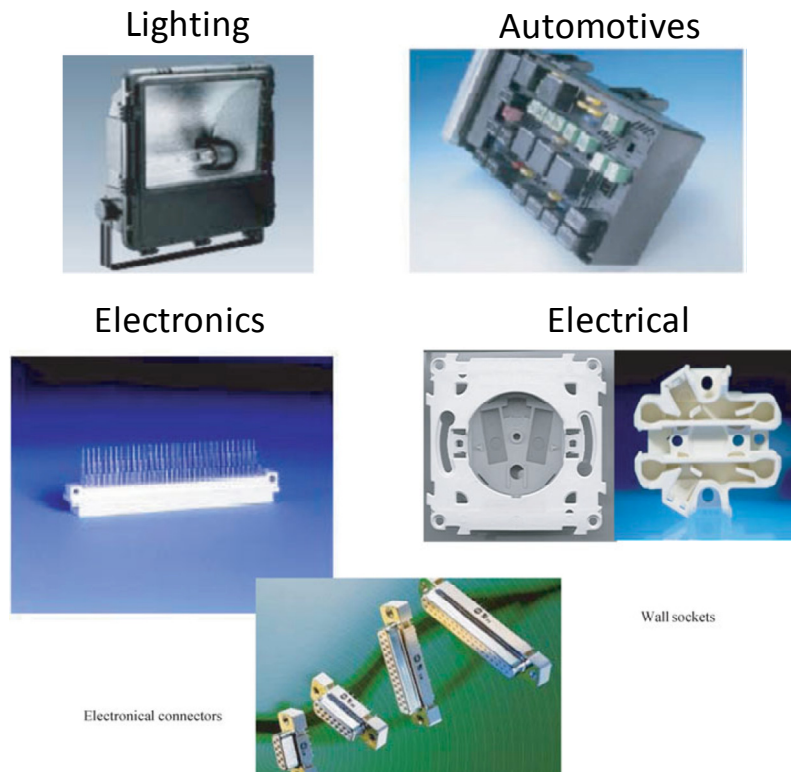
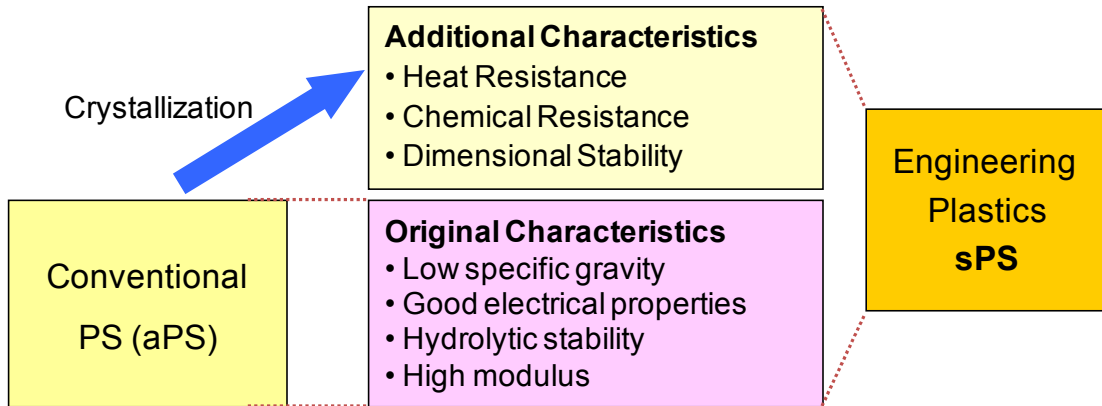


Figure 1.1 The properties and applications of syndiotactic polystyrene (sPS).

Table 1.2 Physical properties of sPS in comparison with PS and PMMA [5]

Property	unit	SPS- IM ^a	SPS-GF ^b	PS	PMMA
Density	g/cm ³	1.02	1.21	1.05	1.2
Tensile strength	kpsi	6.58	15.3	6.4-8.2	10
Elongation	%	30	3.4	2-4	5
Flexible strength	kpsi	11.6	23.7	10-15	11-19
Notched Izod impact	ft-lb/in	1.2	2.5	0.4	0.3
Heat distortion temperature	°C	176	232	75-94	92
Water absorption	%	0.01	0.01	0.05	0.1

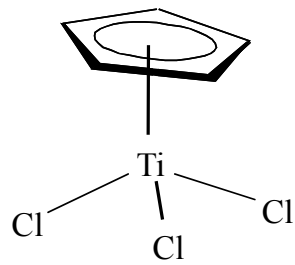
^aDow Plastics grade, impact modified, XU72108.01L.

^bDow Plastics grade, glass filled, XU72107.02L.

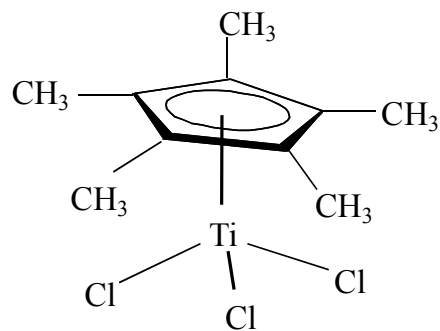
1.1.2 Synthesis of syndiotactic polystyrene

sPS was first synthesized by Ishihara *et al.* [6] in 1985 with cyclopentadienyl titanium trichloride (CpTiCl₃) catalyst. Since then, many different titanium compounds have been found active to produce sPS. In particular, half sandwiched titanium compounds (e.g. CpTi- and Cp^{*}Ti-complexes) have high polymerization activities and high syndiospecificity [7]. Figure 1.2 shows the examples of Ti based metallocene catalysts for sPS synthesis.

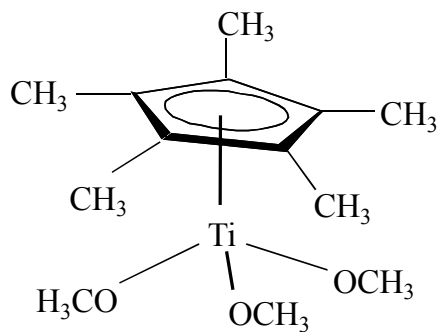
The mechanism of syndiospecific polymerization of styrene with metallocene catalyst is composed of four steps: catalyst site activation (initiation) step, propagation step, chain transfer (termination) step, and catalyst deactivation step.



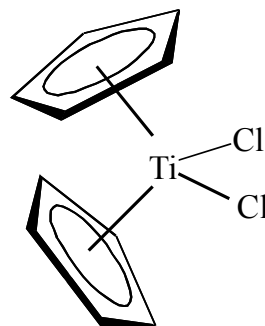
CpTiCl_3



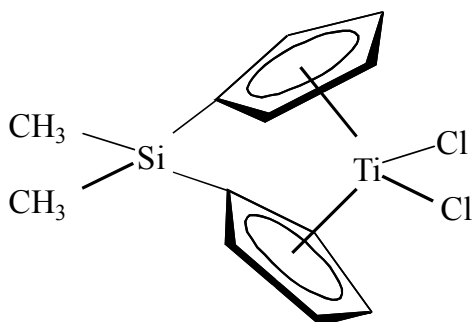
Cp^*TiCl_3



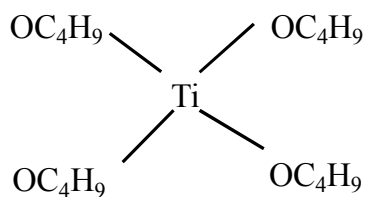
$\text{Cp}^*\text{Ti}(\text{OCH}_3)_3$



Cp_2TiCl_2



$\text{Si}(\text{CH}_3)_2\text{Cp}_2\text{TiCl}_2$



$\text{Ti}(\text{OC}_4\text{H}_9)_4$

Figure 1.2 Examples of Ti based metallocene catalysts for sPS polymerization.

The Ti(III) cation is known as catalyst active site for syndiospecific polymerization of styrene [8, 9]. Figure 1.3 shows the catalytic active site formation mechanism in the sPS polymerization. In the catalyst site activation step, the titanium of the oxidation state (IV) in the titanium complex is reduced to the oxidation state (III) with an aluminum alkyl, AlR_3 or MAO. Then the Ti(III) complex is alkylated again by MAO or AlR_3 , and finally reaction with the cocatalyst leads to the formation of the active Ti(III) cation. The final step is an equilibrium reaction. Therefore, larger amount of MAO promotes polymerization rate by making more active Ti(III) cations.

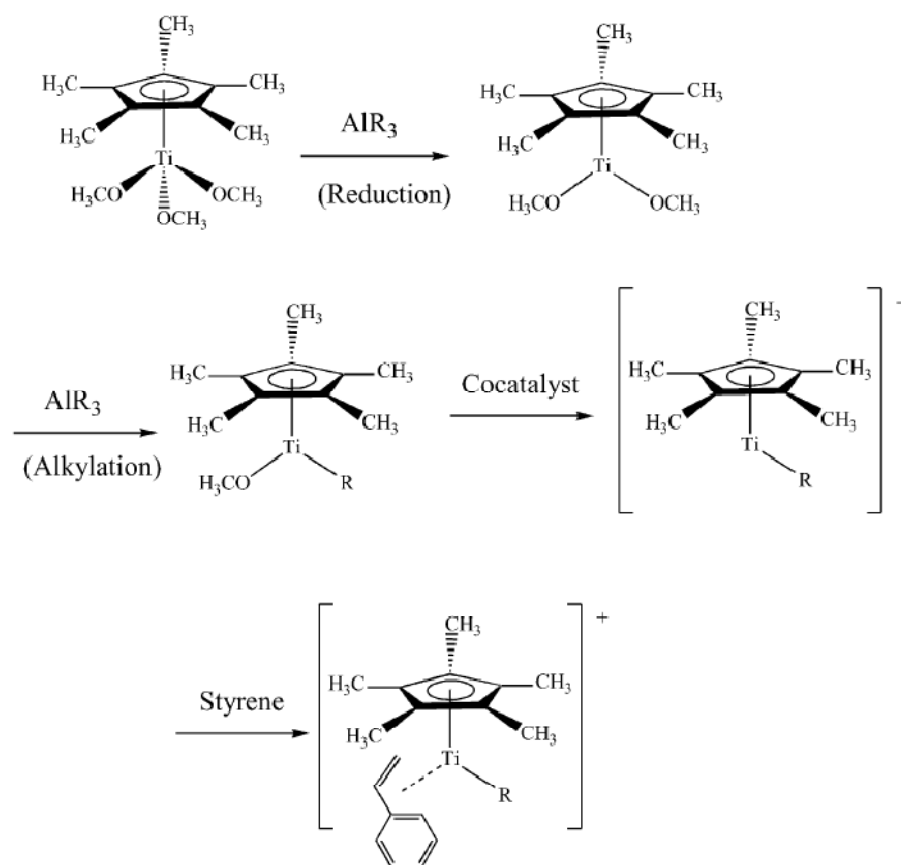


Figure 1.3 The mechanism of active site formation in syndiospecific polymerization of styrene; R: alkyl [8].

The second step is a propagation step that styrene monomers are converted an syndiotactic polymer at the active cationic Ti(III) site. Figure 1.4 illustrates the propagation step of syndiospecific polymerization of styrene. The propagation reaction at the active site is described by the stereochemical control of the reaction, understood by the *cis*-opening of the double bond of styrene, the secondary insertion into the Ti–carbon bond - benzylic carbon is directly bonded to the Ti(III) ion - and the chain-end control of the insertion mechanism [1, 7]. When styrene monomer approaching catalyst active center, syndiotactic configuration is favored because of phenyl-phenyl repulsion between the last inserted unit of a polymer chain and incoming monomer [1].

The propagation reaction can be terminated by a species that contains an exchangeable proton. β -hydride elimination (abstraction) and chain transfer to monomer are the main termination reactions in metallocene catalyzed polymerization as confirmed by ^{13}C -NMR analysis [10]. Duncalf *et al.* [11] analyzed sPS samples synthesized over $\text{Ti}(\eta^5\text{-C}_5\text{H}_4t\text{Bu})\text{Cl}_3/\text{MAO}$ catalyst using mass spectra data and showed that sPS samples contain both methyl and ethyl end groups, indicating that the major mechanism of chain termination is β -hydride elimination. The influence of termination reactions can be evaluated by examining the relationship between monomer concentration and the number average degree of polymerization of sPS [12-15].

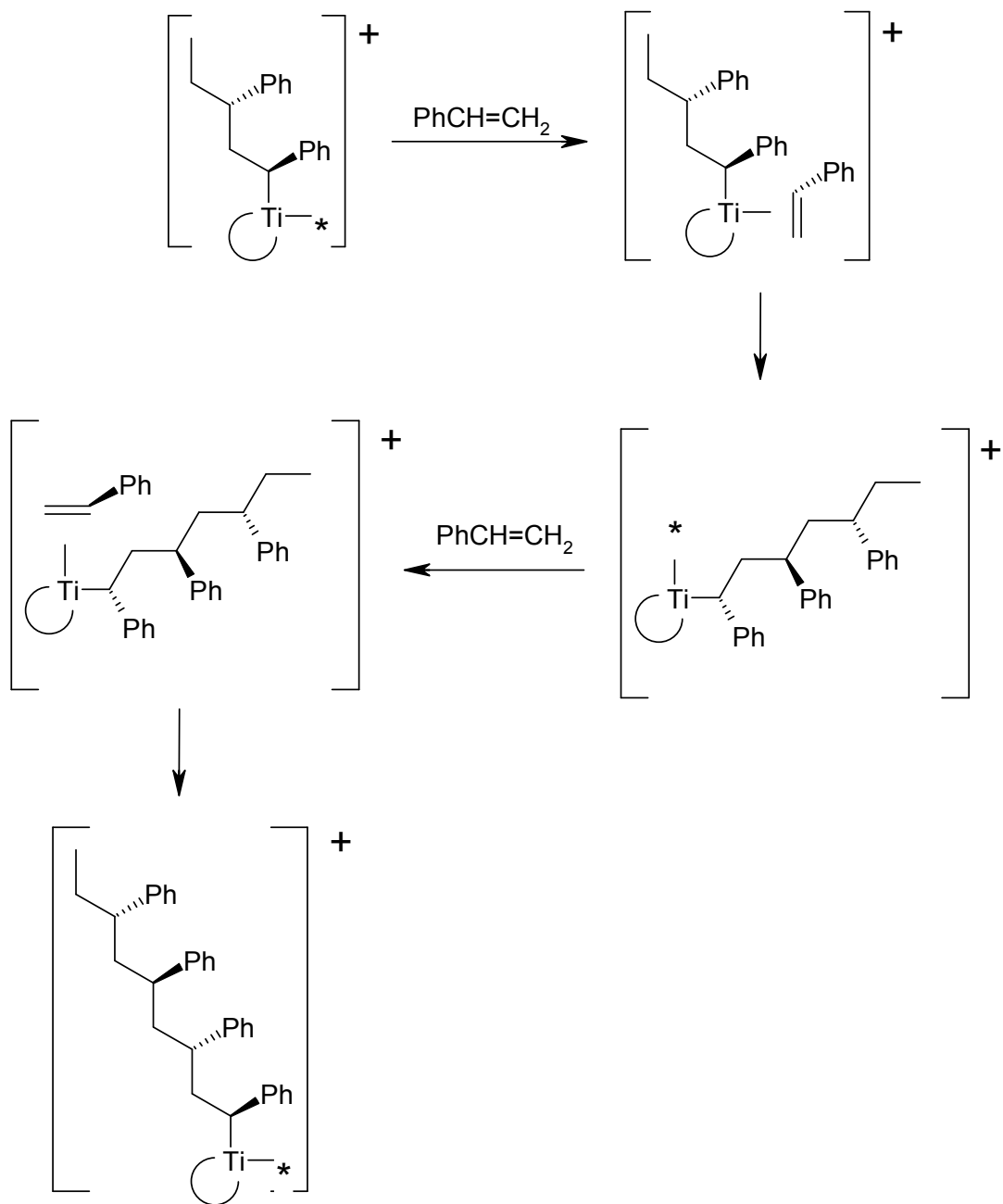


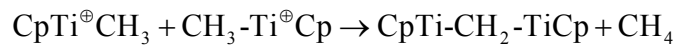
Figure 1.4 Steric control in propagation of syndiospecific polymerization of styrene [1].

$$\frac{1}{X_n} = \frac{k_{t\beta}}{k_p} \frac{1}{[M]} + \frac{k_{tM}}{k_p} \quad (1-1)$$

where X_n is the number average degree of polymerization, k_p , k_{tM} , and $k_{t\beta}$ are the kinetic constants of propagation, chain transfer to monomer, and β -hydride elimination, respectively. Grassi *et al.* [12] obtained the ratio of $k_{t\beta}/k_{tM}$ is 5, indicating that β -hydride elimination is the main termination process in the sPS polymerization over $\text{Ti}(\text{CH}_2\text{Ph})_4/\text{MAO}$ catalyst,. Huang *et al.* [13] also obtained over 5.5 of the ratio of $k_{t\beta}/k_{tM}$ after kinetic analysis of sPS polymerization with $\text{Cp}^*\text{TiCl}_3/\text{MAO}$ catalyst.

Activated catalyst concentration is roughly constant when the reaction time is very short [12]. When reaction time is long enough, many researchers found that deactivation of catalytic active sites reduces the polymerization rate [16-18]. In metallocene catalyzed polymerization, catalyst deactivation occurs via methane abstraction through bimolecular deactivation between two active centers [19-21]. Impurities are known to promote catalyst deactivation. As MAO acts as an impurity scavenger, larger amount of MAO helps to prevent catalyst deactivation by bimolecular process [22].

Bimolecular deactivation process

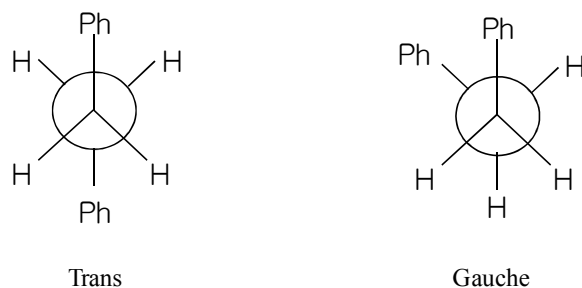


1.1.3 Polymorphism of syndiotactic polystyrene

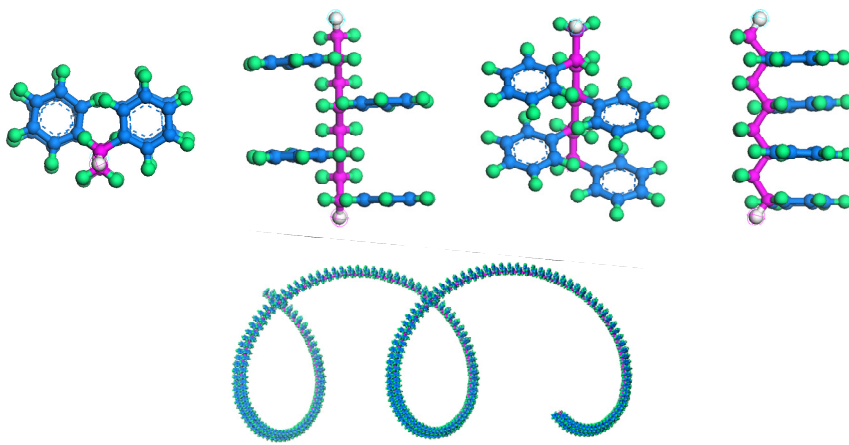
Semicrystalline sPS exhibits a complex polymorphic behavior. By the rotation of phenyl rings of backbone chain, sPS chain can have two stable staggered states – trans (anti) and gauche conformations (Figure 1.5(a)). sPS crystalline structures are characterized by two different conformations and four semicrystalline forms [23, 24]. One is T_4 zigzag planar conformation having two different crystal forms – α and β forms. T_4 conformation is generally formed through melt crystallization of sPS. The other is T_2G_2 helical conformation (2_1 helix conformation) having two different crystal forms of γ and δ forms. Figure 1.5(b) represents the T_4 zigzag planar conformation and Figure 1.5(c) corresponds to the T_2G_2 helical conformation. Note that when polymer chain is long enough, sPS having T_2G_2 helical conformation makes a straight chain whereas sPS having T_4 conformation makes a spiral chain.

The α and β forms, both containing planar zigzag chains with an identity period of $c = 5.05 \text{ \AA}$, can be obtained from the melt or the glassy state of sPS under different thermal conditions [25]. The cooling rate from the melt, the thermal history of the melt and the crystallization temperature are the major factors influencing the formation of these forms. The α form can be obtained by quenching from the melt or by annealing from the amorphous phase. The pure α form is present at low temperatures below about 170°C . When sPS was cooled at a moderate cooling rate from the melt, its β form can be obtained. The pure β form is only produced at high temperatures above about 230°C [23, 25, 26]. The main difference of α and β form is

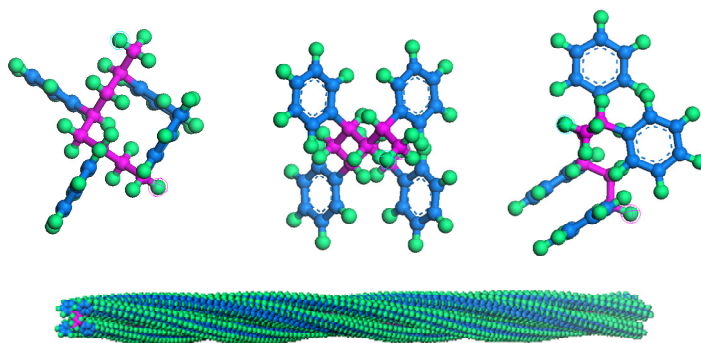
the unit cell structure. The α form consists of hexagonal unit cell with $a = 26.26 \text{ \AA}$, but β form consists of orthorhombic unit cell with $a = 8.81 \text{ \AA}$ and $b = 28.82 \text{ \AA}$.



(a) Trans / Gauche conformation



(b) T₄ zigzag planar conformation, long chain: 400 monomer units



(c) T₂G₂ helical conformation, long chain: 400 monomer units

Figure 1.5 Syndiotactic polystyrene conformations; (b) and (c): drawing based on Materials Studio[®] modeling package (Accelrys Software Inc.).

The forms γ and δ , both containing helical chains of monoclinic unit cell with an identity period of $c = 7.7 \text{ \AA}$, are formed under conditions where solvents are involved [25]. The main difference of γ and δ form is that the crystalline structure has solvent molecules in its cell or not. When concentrated solutions are quenched, the helical δ phase is observed [27]. The δ form crystal can also be obtained by solvent induced crystallization at a temperature below glass transition temperature of sPS [28-31]. The δ form is a complex form of sPS and solvent [30, 32]. Thus, suitable treatment such as annealing can transform δ form to γ form. If solvent molecules are removed from sPS above glass transition temperature, γ form sPS crystal is obtained.

The guest molecules included in clathrate structures (δ form) can be completely removed through extraction process, and the emptied δ -form, δ_e form, is obtained. The δ_e form has slightly low density (0.977 g/cm^3) in comparison with amorphous form (1.06 g/cm^3) [33]. The crystal structure of the δ_e form is characterized by the presence of empty cavities previously occupied by guest molecules in the δ form [34]. It has micro-void between the polymer chains. Therefore, δ_e form can absorb a specific solvent selectively because it memorizes the size and shape of solvent molecules which were trapped in former δ form [30]. Table 1.3 summarizes the density and crystal cell dimensions of sPS crystals and Figure 1.6 summarizes the polymorphic structures of sPS.

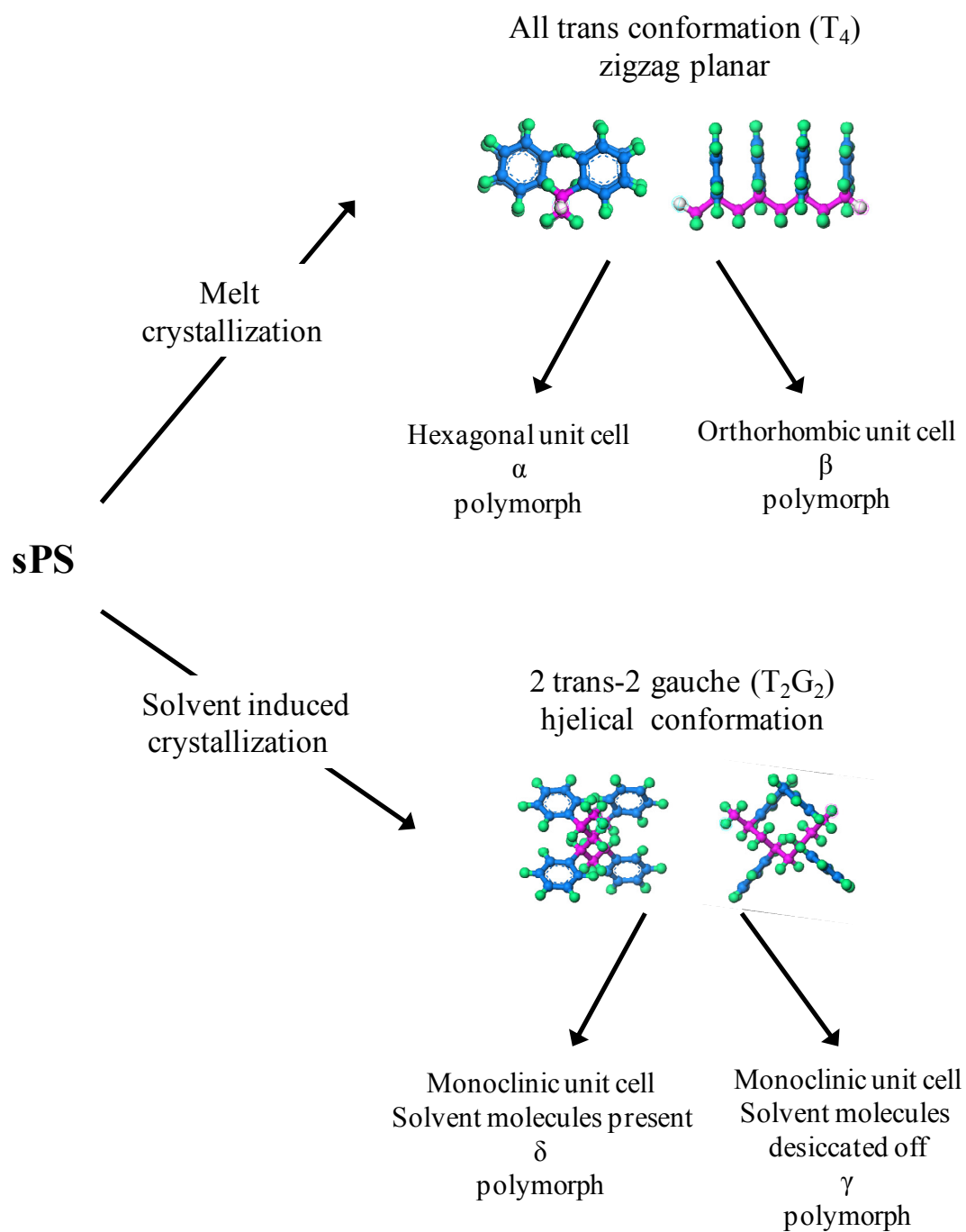


Figure 1.6 Summary of the polymorphic structures of sPS. [35]

Table 1.3 Density and crystal cell dimensions of sPS polymorphs [36, 37]

Crystal	Density (g/cm ³)	Unit cell	<i>a</i> (Å)	<i>b</i> (Å)	<i>c</i> (Å)	γ (°)
α	1.034	hexagonal	26.25	26.26	5.04	120
β	1.08	orthorhombic	8.81	28.82	5.06	90
γ^a	1.07	monoclinic	19.43	8.51	7.93	83.4
δ	1.11	monoclinic	17.58	13.26	7.71	121.2
δe	0.977	monoclinic	17.4	11.85	7.70	117

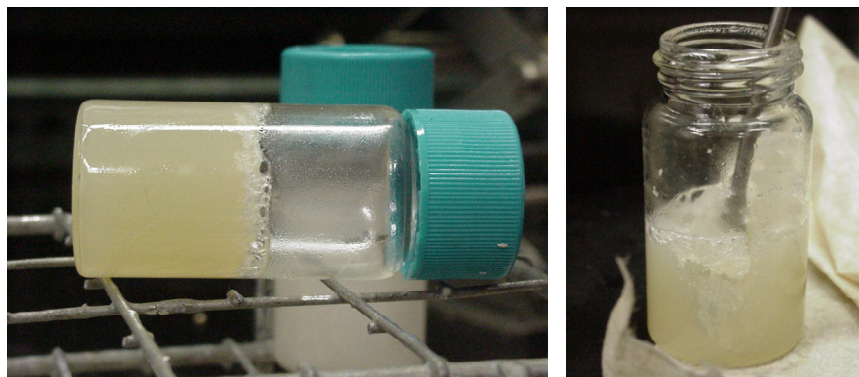
a. simulation value by Tamai et al. (2002)

1.1.4 Thermoreversible gelation

sPS is a highly chemical resistant thermoplastic and insoluble in its own monomer (styrene) and many organic solvents at its typical reaction temperatures (40-90°C). When styrene is polymerized to sPS, polymer particles precipitate out from the reaction mixture during the early stage of polymerization. As monomer conversion increases the polymer particles agglomerate and they develop into an immobile gel. The sPS gel is classified as a thermoreversible gel [38].

The sPS gel is not a covalently cross-linked gel but a thermoreversible gel with 2_1 -helix conformation [23, 24, 39, 40]. Daniel *et al.* [41, 42] proposed a cavity model to explain thermoreversible gelation of sPS: At low temperature with solvent, sPS crystallizes into a δ -form crystal that has a helical conformation. The helical form of sPS crystal is stabilized by the intercalation of the solvent molecules between the phenyl groups of the sPS chains, increasing the chain rigidity. The folding of sPS chains are inhibited by the intercalation and as a result, sPS grows with a fibrillar

structure [42]. In sPS polymerization, styrene monomers intercalate with sPS chains, forming sPS nanofibrils as polymerization proceeds.



Soft sPS gel



Hard sPS gel

Figure 1.7 Thermoreversible gel of sPS; toluene is used as solvent.

Figure 1.7 shows the thermoreversible gels of sPS after solution polymerization over homogeneous metallocene catalyst. The sPS gel can be classified into two different states. At low total solid contents (TSC, about 3-5 wt. %), reaction mixture transforms to a soft-gel. Soft-gel does not flow like gel, but is easily

breakable. At high TSC (over 10 – 15 wt. %), reaction mixture changes to a hard-gel. It is very difficult to break hard sPS gel. Thus, after forming hard thermoreversible gel, the gelation makes the agitation of the reaction mixture difficult with conventional agitators or mixers.

To avoid global gelation phenomenon, several methods have been tried. In the industries, specially designed reactors such as self-cleaning reactors equipped with intermeshing blades or screws were proposed [43, 44]. Fan *et al.* [45, 46] reported that they obtained powdery sPS by choosing a proper agitator and reinforcing its stirring shear in bulk polymerization over homogeneous metallocene catalysts.

1.2 Research Objectives

The major objectives of the thesis are:

- (1) To investigate the effects of reaction variables on the kinetics of syndiospecific polymerization of styrene with $\text{Cp}^*\text{Ti}(\text{OCH}_3)_3/\text{MAO}$ in homogeneous and heterogeneous systems;
- (2) To analyze the reaction kinetics and develop a mathematical model to predict catalyst activities, polymer yields, and molecular weight distribution under various operation conditions;
- (3) To investigate the nascent morphology of sPS particles in slurry phase reactions;

(4) To study the polymer properties and morphology of sPS synthesized in silica-coated nanotube reactors (SNTRs).

For the successful development of syndiospecific polymerization of styrene in homogeneous and heterogeneous polymerization process, it is needed to investigate the reaction mechanisms and characteristics of polymers including morphological aspect under various operation conditions and develop a mathematical model. Since a mathematical model can be directly used for process design and for the development of operational policies for various grades of polymer, it will be a very useful tool in the industries. Moreover, understanding of the morphology of polymer helps us understand polymerization mechanism and polymer properties. Therefore, it is expected that the current research reported in this thesis will make a new and valuable contribution to increase the fundamental knowledge about sPS synthesis.

Chapter 2: Kinetics of Syndiospecific Polymerization of Styrene over Homogeneous Metallocene Catalysts

2.1 Introduction

Since the first synthesis of sPS by Ishihara *et al.* [6], the synthesis of sPS has been investigated by many researchers in the past, and some review articles [1, 3, 4, 7, 47] provide a comprehensive overview of the recent developments of catalyst systems for the syndiospecific polymerization of styrene. Many different types of catalysts that are effective for sPS polymerization include cyclopentadienyl and substituted cyclopentadienyl derivatives of titanium such as CpTiCl_3 and $\text{Cp}^*\text{Ti}(\text{OCH}_3)_3$ with methylaluminoxane (MAO) as a cocatalyst. In Table 2.1, the results of syndiotactic polystyrene polymerization with different types of catalysts are summarized. As shown in Table 2.1, zirconocenes generally cannot produce sPS.

Although there are many reports on the synthesis of sPS, little has been reported on the modeling of sPS polymerization kinetics [12-14, 46, 48-52]. Oliva *et al.* [48] report preliminary kinetic study on sPS polymerization with $\text{Ti}(\text{OC}_4\text{H}_9)_4/\text{MAO}$. Oliva *et al.* [48] show that polymerization rate increase with increasing monomer concentration and average molecular weight increase with reaction time. By examining the dependence of polymerization rate with monomer concentration, They obtain the temperature coefficient of the kinetic rate constant ($E_p = 8\text{kcal/mol}$) [48]. The first order kinetics of monomer concentration was also

observed by other groups [12, 14, 15]. Grassi *et al.* [12] show that with Cp^*TiR_3 ($\text{R} = \text{CH}_3, \text{CH}_2\text{Ph}$)/MAO catalyst, sPS yield is proportional to styrene concentration and that catalytic active site concentration is almost constant for 10 min with a homogeneous catalyst. Kawabe *et al.* [15] also show the polymerizations of styrene were first order with respect to the monomer concentration in CpTiCl_3 /MAO reaction system.

Table 2.1 syndiotactic polystyrene polymerization with different types of catalysts

Catalyst	Reaction Temp.	[St]/[Me]	[Al]/[Me]	Syndiotacticity	Catalyst Activity	Reference
TiCl_4	50 °C	4000	800	syndiotactic	4.1%	[17]
$\text{Ti}(\text{OC}_4\text{H}_9)_4$	50 °C	5244	100	91%	0.57 g	[53]
CpTiCl_3	50 °C	4000	300-600	syndiotactic	99.2%	[53]
CpTiCl_3	70 °C	6000	500	>90 %	27.7%	[54]
Cp^*TiCl_3	50 °C	4000	100-900	syndiotactic	75.4%	[17]
Cp^*TiCl_3	50 °C	68800	300	syndiotactic	15 ^a	[55]
Cp^*TiCl_3	70 °C	6000	500	>95 %	31%	[54]
Cp^*TiCl_3	50 °C	70080	300	97.2%	40 ^a	[56]
Cp^*ZrCl_3	50 °C	6880	300	isotactic	0.08 ^a	[55]
Cp^*TiF_3	50 °C	70080	300	99.4%	940 ^a	[21]
$\text{Cp}^*\text{Ti}(\text{OCH}_3)_3$	70 °C	233333	100	syndiotactic	33%	[8]
$\text{Cp}^*\text{Ti}(\text{OCH}_3)_3$	50 °C	233333	300	syndiotactic	39.1%	[57]
$\text{Cp}^*\text{Ti}(\text{OC}_4\text{H}_9)_3$	45 °C	8775	1000	93%	30600 ^b	[58]
Cp_2TiCl_2	50 °C	4020	600	syndiotactic	1.0%	[59]
$\text{CpTiCl}_3/\text{Silica}$	50 °C	21800	300	87.7%	238 ^b	[60]
$\text{CpTiCl}_3/\text{MAO/Silica}$	50 °C	21800	300	79.8%	38 ^b	[60]
$\text{CpTiCl}_3/\text{Silica}$	50 °C	26892	940	79%	2892 ^c	[61]

a. kg-sPS/mol-Me.h

b. kg-sPS/mol-Me.mol-St.h

c. g-sPS/g-Ti

However, only low initial monomer concentrations (up to 1.2 mol/L of styrene [12], up to 1.5 mol/L of styrene [15]) were used or polymerization was stopped at low monomer conversion (0.8g in 40mL solution [48]). In bulk polymerization experiments with $\text{Cp}^*\text{TiCl}_3/\text{MAO}$ and $\text{Cp}^*\text{Ti}(\text{OPhOCH}_3)_3/\text{MAO}$ catalysts, Fan *et al.* [46] obtained discrete polymer particles at high monomer conversion and report S-shaped monomer conversion profiles which are caused by two different polymerization locus – liquid and solid phase or heat accumulation in the solid polymer phase. Choi *et al.* [51] carried out sPS slurry polymerization with homogeneous $\text{Cp}^*\text{Ti}(\text{OCH}_3)_3/\text{MAO}$ catalyst. They observe no global gelation at low styrene/heptane ratio. They also observe the apparent propagation rate constant decrease with an increase in styrene concentration in the liquid phase and claim that the decrease in the polymerization rate is not exclusively due to the depletion of monomer and the active catalytic site deactivation, but probably due to the mass transfer resistance exerted by the solid polymer phase [51].

With molecular weight and polymerization rate data, Chien and Salajka obtain kinetic parameters in $\text{Bz}_4\text{Ti}/\text{MAO}$ [49] and $\text{CpTi}(\text{OC}_4\text{H}_9)_3/\text{MAO}$ system [50]. By electron paramagnetic resonance (EPR) and redox titration, they determine that catalytic active site is Ti(III) ion [62]. They also claim that the chain transfer to monomer reaction can be neglected because β -hydrogen elimination reaction rate is much faster than chain transfer to monomer by analyzing polymerization rate and molecular weight data [50]. With $\text{CpTi}(\text{OC}_4\text{H}_9)_3/\text{MAO}$ catalyst, Chien *et al.* [62] obtain broad polydispersity index values lying between 4 and 6 and conclude $\text{CpTi}(\text{OC}_4\text{H}_9)_3$ is not a single site catalyst. Duncalf *et al.* [11] observe average

molecular weight increase with time and molecular weight decrease with reaction temperature and conclude chain transfer step become more important as the reaction temperature increases.

Nevertheless a few reaction kinetics studies are reported about several different catalyst systems, it is often difficult to generalize the polymerization kinetics observed for a certain catalyst system to other similar or different catalyst systems. At very low monomer concentrations, first order kinetics of monomer has been accepted, but at high monomer concentration and high monomer conversion, polymerization rate seems not to linearly depend on the monomer concentrations. During sPS polymerization, undissolved sPS solid is created and this sPS gelation must affect the sPS polymerization kinetics. In this chapter, a slurry phase sPS polymerization over homogeneous $\text{Cp}^*\text{Ti}(\text{OCH}_3)_3$ /MAO catalyst is carried out. During slurry polymerization, phase change of reaction mixture is observed. With experimental results, mathematical modeling study of a slurry phase sPS polymerization over homogeneous $\text{Cp}^*\text{Ti}(\text{OCH}_3)_3$ /MAO catalyst will be presented.

2.2 Experimental

2.2.1 Materials

Styrene (Aldrich) was vacuum distilled over calcium hydride, and activated alumina was used to remove inhibitor from the monomer. Figure 2.1 shows the styrene purification apparatus and procedure. Alumina was previously activated in

high temperature oven (over 250°C) for 3 hrs and kept in a storage bottle. The styrene purification system consists of a three-neck flask, a head, and a distillation column as shown in Figure 2.1(a). Purification equipment was dried with N₂ /vacuum process several times. Then, styrene and calcium hydride were added in the three-neck flask (Figure 2.1(b)), and styrene was vacuum distilled for at least 12 hrs at room temperature (Figure 2.1(c)). After vacuum distillation, purified styrene was transferred to a storage bottle which contains activated alumina (Figure 2.1(d)). Purified styrene was kept in a refrigerator.

n-heptane (Fisher Scientific) was used as a diluent, and it was purified by being refluxed over sodium and benzophenone in nitrogen atmosphere. Figure 2.2 shows the solvent purification apparatus and procedure. The solvent purification system consists of a three-neck flask, a 1000 mL storage head, and a condenser as shown in Figure 2.2(a). The solvent purification system was deoxygenated with N₂ /vacuum process several times. Then, solvent, sliced sodium, and benzophenone were loaded into the three-neck flask (Figure 2.2(b)), and solvent was boiled and refluxed until the color of solution turned to dark blue (Figure 2.2(c)). The purified solvent was transferred to a storage bottle containing activated molecular sieve. Molecular sieve (4A type) was activated in high temperature oven (over 250°C) for 3 hrs. Purified solvent was kept in the glove box. Cp*Ti(OCH₃)₃ (Pentamethyl cyclopentadienyl titanium trimethoxide, Strem Chemicals, min 97%) and modified methyl aluminoxane (MMAO, Akzo Nobel, 6.8 wt.% Al content) were used as supplied without further purification.



Figure 2.1 Styrene monomer purification apparatus and procedure; (a) solvent purification system, (b) styrene and calcium hydride in the three-neck flask, (c) styrene distillation, (d) styrene transfer to a storage bottle.

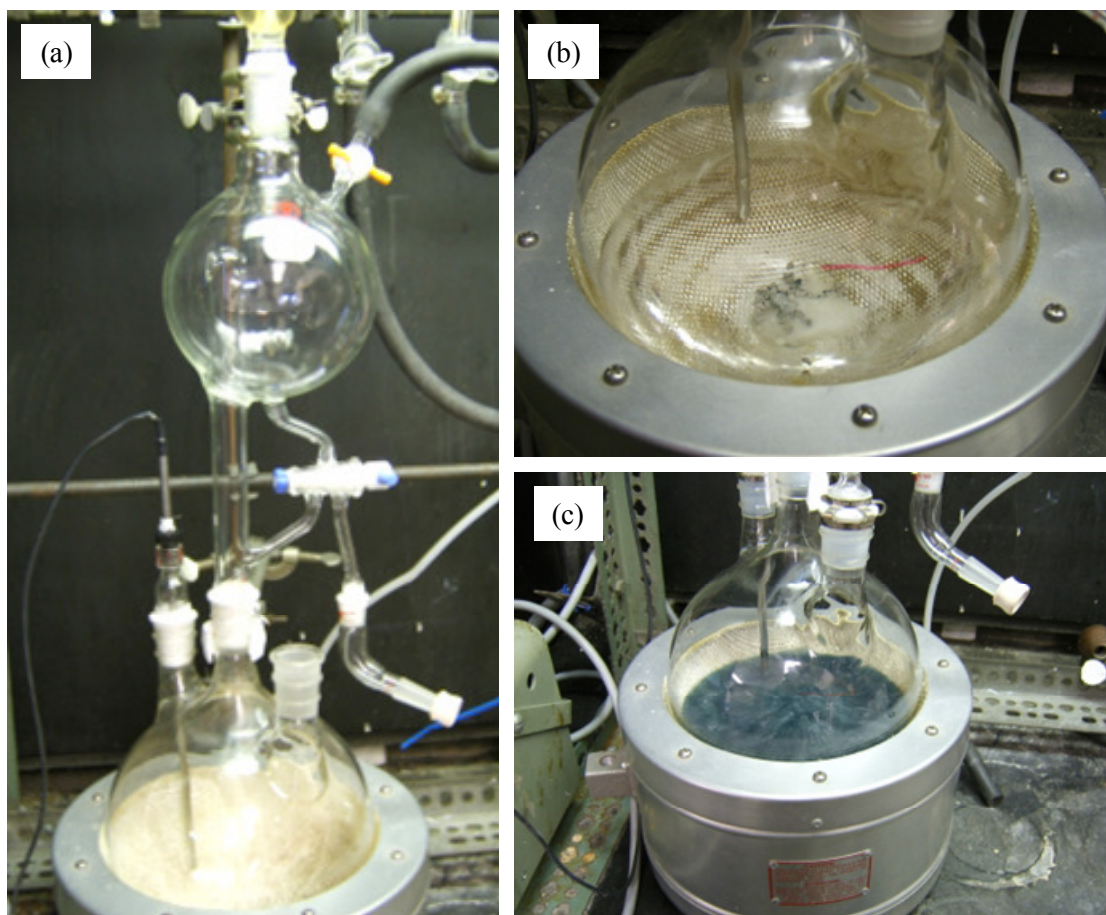


Figure 2.2 Solvent purification apparatus and procedure; (a) solvent purification system, (b) loading of solvent, sliced sodium, and benzophenone into the three-neck flask, (c) purified solvent.

2.2.2 Styrene polymerization with homogeneous metallocene catalyst

Syndiospecific polymerization of styrene experiments were carried out using 20 mL reaction vessels. Predetermined amounts of monomer, solvent, catalyst and MMAO were charged into the reaction vessels in a glove box (for detail experimental conditions, see Table 2.2). All the reaction vessels were taken out of the glove box and immersed in the water bath. In all the polymerization experiments, the temperature of water bath was maintained at 70°C. The initial catalyst concentration was fixed at 1.65×10^{-4} mol-Ti/L, and the Al/Ti mole ratio was fixed at 500. After polymerization, the reaction mixture was removed from the reaction vessels, washed with excess amount of acidified methanol (10 vol. % of hydrochloric acid), and dried *in vacuo*.

The monomer conversion was determined gravimetrically by measuring the polymer weight for a known amount of initial monomer and diluent. The total solid content (TSC) was determined by measuring the weight of the initial reaction mixture and the weight of the polymer produced (i.e., $\text{TSC} = \text{polymer weight} / \text{initial weight of reaction mixture}$). The methylethylketone (MEK) insoluble fraction was used as a quick but approximate measure of the syndiotacticity. MEK insoluble fraction was measured with Soxhlet extractor. Dried sPS sample was weighed and placed inside a thimble, which is loaded into the main chamber of the Soxhlet extractor. The Soxhlet extractor was placed onto a flask containing MEK. Then, the Soxhlet is equipped with a condenser. MEK was heated to reflux. Refluxed MEK flowed into the main

chamber and sample in a thimble was soaked by warmed MEK. aPS in a sample was dissolved in MEK and when the Soxhlet chamber was almost full, the chamber was automatically emptied by a siphon side arm. This cycle was repeated for 24 hr. After 24 hr, polymer sample was retracted from the thimble and dried *in vacuo*. MEK insoluble fraction was calculated by using the polymer weight change. Most of the sPS samples showed that the MEK insoluble fractions were in the range of 93 – 95%.

2.3 Results and Discussion

2.3.1 Polymerization Rate Analysis

The series of syndiotactic styrene polymerization experiments in homogeneous metallocene catalytic system were carried out at different monomer concentrations. Table 2.2 summarizes sPS polymerization experimental results with the change of monomer concentrations and reaction time. The same concentration of catalyst and Al/Ti mole ratio in all these experiments were used. The polymerization rate values were determined by numerically differentiating polymer conversion vs. time curve with ORIGIN[®] package. Table 2.2 shows that the polymerization yields and polymerization rates (R_p) increase with increasing monomer concentration.

Figure 2.3 shows the measured styrene conversion data at different initial monomer concentrations. In all the experimental runs, monomer conversion reaches plateau in 10 min. Even 2 min of reaction time, monomer conversions were very high (above 30%), because of high initiator concentration. Catalyst activity decreases with

as monomer concentration decreases but catalyst deactivation is also expected to contribute to the activity decay.

Table 2.2 Yields and polymerization rates of syndiospecific polymerization of styrene over homogeneous metallocene catalyst

Styrene/heptane (v/v)	[M] ₀ (mol/L)	Time (min)	Yield (g)	Conversion	R _p (mol/L.hr)	Catalyst Activity (kg-sPS/mol-Ti.hr)
1/9	0.87	2	0.58	0.64	9.80	6184
		3	0.63	0.69	3.46	2182
		5	0.77	0.85	2.36	1491
		10	0.83	0.91	0.40	250
		22	0.85	0.94	0.12	75
		30	0.87	0.96	0.08	49
		60	0.88	0.97	0.02	12
2/8	1.75	2	0.98	0.54	18.63	11761
		5	1.45	0.80	5.90	3722
		10	1.69	0.93	2.77	1746
4/6	3.49	2	1.49	0.41	31.84	20096
		5	2.57	0.71	12.73	8038
		10	2.98	0.82	4.73	2984
6/4	5.24	2	1.95	0.36	46.63	29431
		5	3.88	0.71	23.61	14902
		10	4.77	0.87	10.14	6404
8/2	6.98	2	2.37	0.33	63.15	39858
		5	5.40	0.74	35.52	22419
		10	6.53	0.90	13.02	8221

Reaction conditions: T = 70°C, [Ti] = 0.165 mmol-Ti/L, Al/Ti mol ratio = 500, total reaction volume = 10 mL

To find the dependency of polymerization rate on monomer concentration, the initial polymerization rates vs. time at different initial monomer concentrations are plotted in Figure 2.4. It has been reported by many workers that the sPS

polymerization rate follows the first-order kinetics with respect to monomer concentration for various metallocene catalysts [12, 14, 15, 48].

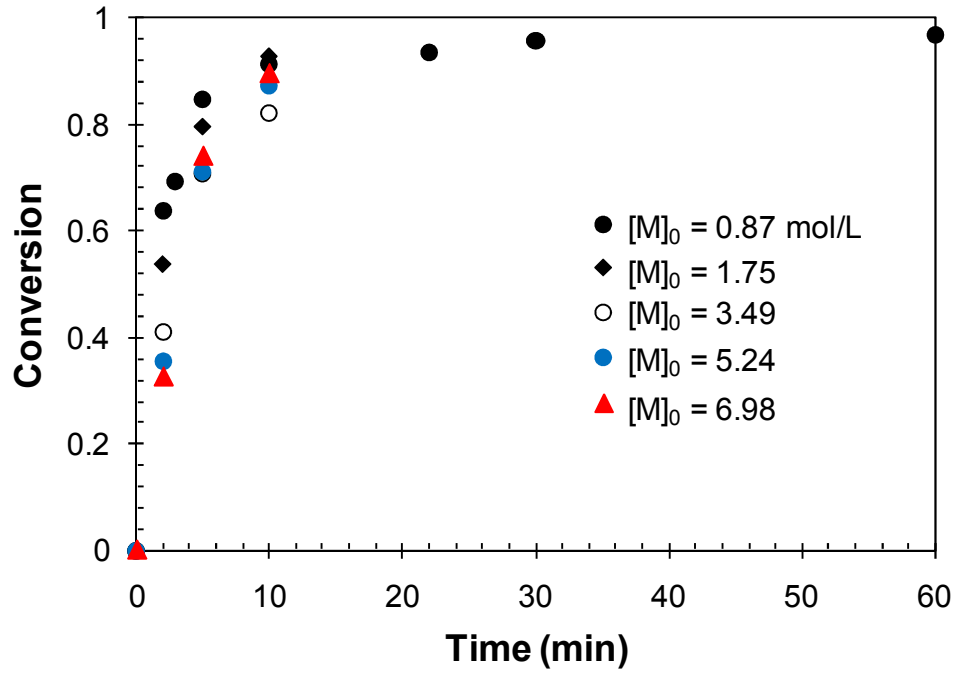


Figure 2.3 monomer conversion profiles vs. reaction time at different initial monomer concentrations.

The initial polymerization rate is proposed to follow the following form:

$$R_{p0} = k_p [M]_0 [C^*]_0 \quad (R_{p0} \text{ in mol/L.hr}) \quad (2-1)$$

where k_p is the propagation rate constant, $[M]_0$ is the initial monomer concentration, and $[C^*]_0$ is the initial catalyst concentration.

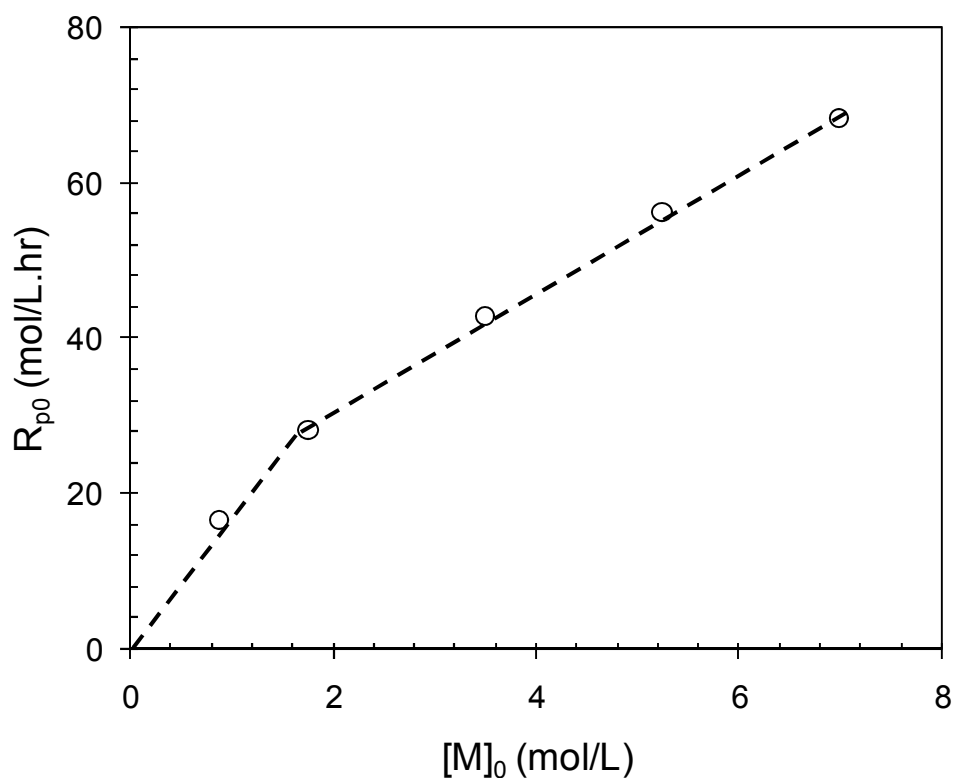


Figure 2.4 Initial polymerization rate vs. initial monomer concentrations ($T = 70^{\circ}\text{C}$, $[\text{Ti}] = 0.165 \text{ mmol-Ti/L}$, $\text{Al/Ti mol ratio} = 500$, symbol: experimental data, line: regression result).

Figure 2.4 shows the dependence of the initial polymerization rate on the monomer concentration. It is seen that the slope of R_{p0} vs. $[\text{M}]_0$ curve or line is steeper at lower monomer concentration than that at higher monomer concentration. In our experiments, it was observed that the polymer gelation occurred at about 2 min of reaction. At high monomer concentration, the initial polymerization rate becomes larger and hence, the time for the onset of gelation will be even shorter. After the gelation, the transport of monomer to catalytic

sites might be hindered by the presence of the solid phase, resulting in the decreased polymerization rate.

The effect of catalyst concentration on the initial polymerization rate is also investigated. The results are shown in Table 2.3 and Figure 2.5. At very low catalyst concentrations ($[\text{Ti}]_0 < 6 \times 10^{-5} \text{ mol/L}$), no polymer was produced. It is probably because at such low catalyst concentrations, the catalyst might have been deactivated by the impurities present in the liquid phase with very few sites left available for polymerization. Over the range of catalyst concentration we have tested, the initial sPS polymerization rate shows the first order dependence on the initial catalyst concentration.

Table 2.3 Initial polymerization rates at different catalyst concentrations

St/Ti (mol/mol)	$[\text{Ti}]_0 \times 10^4$ (mol/L)	Time (min)	Yield (g)	Conversion	R_{p0} (mol/L.hr)
100000/1	0.85	10	3.51	0.386	20.22
75000/1	1.12	2	1.50	0.165	43.21
50000/1	1.65	2	2.89	0.318	83.28
30000/1	2.65	2	6.18	0.679	177.83

* $[\text{M}]_0 = 8.73 \text{ mol/L}$, Al/Ti mol ratio = 500, T = 70°C.

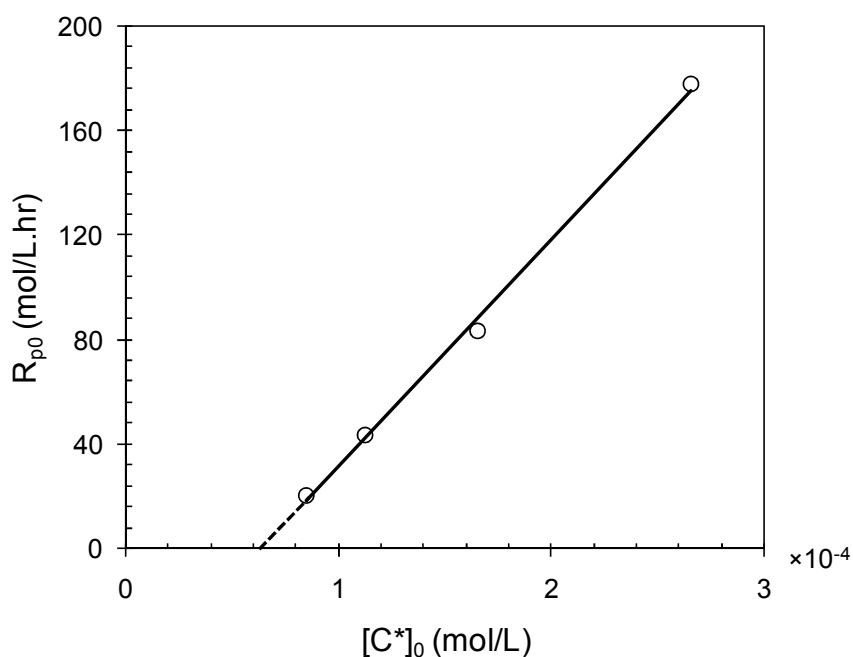


Figure 2.5 Initial polymerization rate vs. initial catalyst concentrations (bulk polymerization, $[M]_{b0} = 8.73$ mol/L, $T = 70^\circ\text{C}$, $\text{Al/Ti} = 500$).

We performed a simple kinetic analysis with eq. (2-1) that can be rearrange to

$$\frac{R_{p0}}{[M]_0[C^*]_0} = k_p \quad (2-2)$$

Figure 2.6 illustrates the propagation rate constant calculated from eq. (2-2) vs. initial monomer concentrations. Notice that the calculated propagation rate constant decreases with an increase in initial monomer concentrations. Since it is unlikely that the intrinsic propagation rate constant will be dependent on the monomer concentration, the results shown in Figures 2.6 suggest that the true rate constant may be masked by some other effects. For example, we can think of the monomer mass

transfer limitation in the solid phase and the monomer partition in the solid and liquid phase as possible cause.

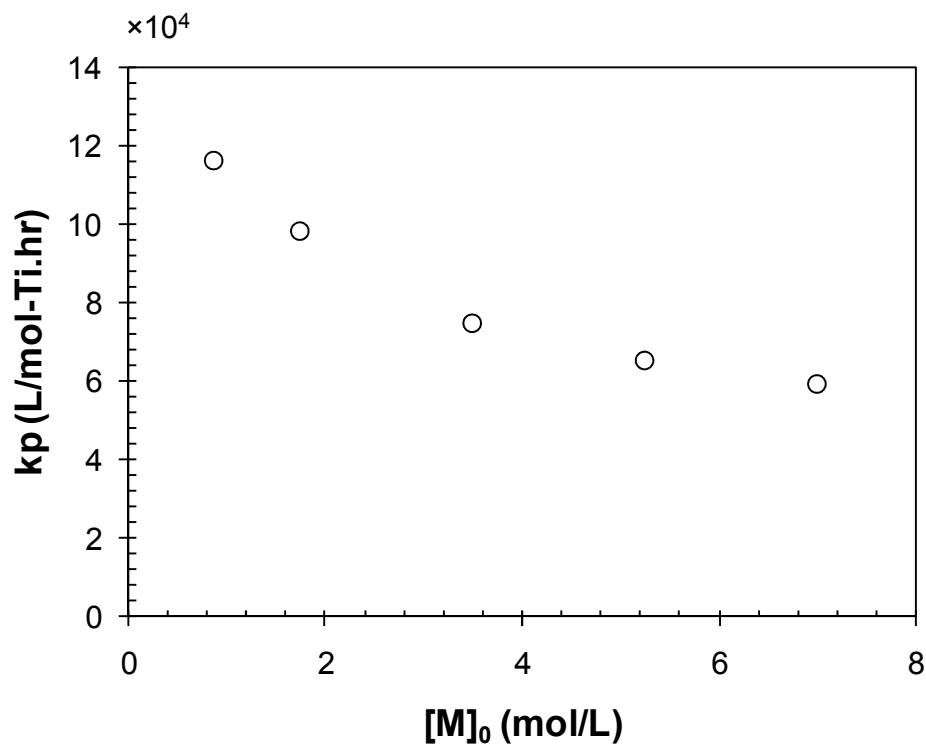


Figure 2.6 Propagation rate constant vs. initial monomer concentration ($T = 70^{\circ}\text{C}$, $[\text{Ti}] = 0.165 \text{ mmol-Ti/L}$, $\text{Al/Ti mol ratio} = 500$).

Figure 2.7 illustrates the modified polymerization rate ($R_p/[M]_0$) and the effective propagation rate constant (k_p) with reaction time. The decrease in the polymerization rate with time is primarily due to the depletion of monomer, but the catalyst deactivation may also be contributing. The occlusion of some active sites in the solid phase can also reduce the polymerization rate.

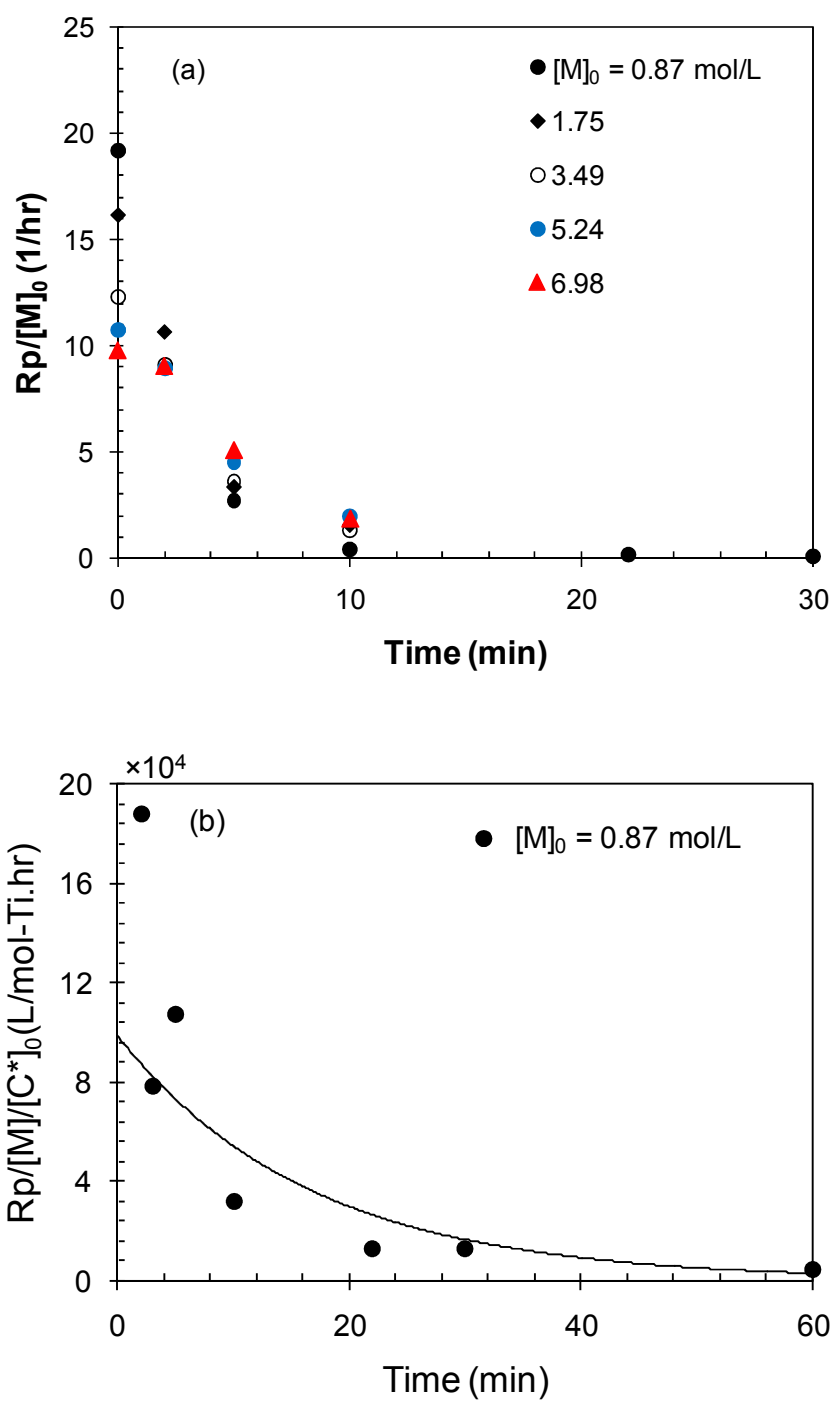


Figure 2.7 (a) Modified polymerization rate changes, (b) effective propagation rate constant with reaction time, solid curve: the exponential regression curve; $T = 70^\circ\text{C}$, $[\text{Ti}] = 0.165$ mmol-Ti/L, Al/Ti mol ratio = 500.

From the foregoing experimental data, we propose that the rate constant that can be estimated from eq. (2-2) is the effective or apparent rate constant:

$$\frac{R_p}{[M][C^*]_0} = k_p^{eff} \quad (2-3)$$

By dividing the polymerization rate with the time-dependent monomer concentration ($[M]$), monomer depletion effect can be removed from the effective propagation rate constant. Then, the decrease of effective propagation rate constant, as shown in Figure 2.7(b), can be regarded as the results of catalyst deactivation or physical transport limitation. The decline in the k_p value is modeled as a first order decay of catalyst activity [i.e., $[C^*] = [C^*]_0 \exp(-k_d t)$]:

$$\frac{R_p}{[M][C^*]_0} = k_p e^{-k_d t} \quad (2-4)$$

The solid curve in Figure 2.7(b) is the exponential regression curve, and the deactivation rate constant value obtained at 70°C is $k_d = 3.59 \text{ hr}^{-1}$.

2.3.2 Physical transitions during sPS polymerization

The study of physical changes of the reaction mixture in a reactor can help understand sPS polymerization reaction mechanism. After solid phase sPS gel is produced, the monomer concentration in the solid (gel) phase is changed by the diffusion of monomer from liquid phase. The main reason for sPS gel formation is the

interaction force between phenyl groups of main chain and guest molecules. In the sPS polymerization, guest molecules will be styrene monomer itself and solvent which is used for diluent. Unquestionably, styrene monomer has strong interaction with phenyl rings of main chain. Thus, selection of solvent type and monomer to solvent ratio are key factors to determine the strength of interaction force between phenyl rings of main chain and guest molecules and avoid global gelation in a reactor.

To investigate the physical phase changes of reaction mixture, sPS polymerization over homogeneous catalyst was carried out in 100 mL of reactor with agitator. Table 2.4 summarized the results of sPS polymerization experiments.

Table 2.4 sPS polymerization experimental data for physical phase change in an agitated reactor

Catalyst type	Solvent	Styrene/solvent	Reaction time	Remarks
		(v/v ratio)	(min)	
Homogeneous	Heptane	1/9	10	turbid solution
		4/6	10	turbid solution
		6/4	10	marsh mallows
			120	dry powder
		8/2	10	low density aggregagtes

Figure 2.8 illustrates the series of physical phase changes of reaction mixture at different styrene to solvent volume ratio. Unlike with toluene diluent (see Figure 1.5), fine sPS particles can be obtained with *n*-heptane. As shown in Figure 2.8, particle formation times vary with initial styrene/heptane volume ratio. At high *n*-heptane volume ratio (styrene/heptane = 1/9 v/v), polymer particles were precipitated

out before 1 min, whereas at low *n*-heptane volume ratio (styrene/heptane = 8/2), precipitated polymer particles were not shown even at 9 min.

The solubility parameter is one of good factors to estimate the interaction force between two molecules. The solubility parameter of reaction mixture is not the same to the solubility parameter of solvent. Because solubility properties are the net result of intermolecular attractions, the solubility parameter of a reaction mixture is determined by calculating the volume-wise contributions of the solubility parameters of the individual components of the mixture [63]. The solubility parameters of styrene/*n*-heptane mixtures were calculated and listed in Table 2.5. Solubility parameter of reaction mixture increases with increasing styrene volume ratio. Thus, at higher styrene volume ratio, discrete sPS particles generate in the reactor very slowly. As polymerization goes, styrene monomer converted to polymer chains and solubility parameter of reaction mixture decreases. Therefore, even of 8/2 of initial styrene/heptane was used, global gelation can be avoided.

Table 2.5 The solubility parameters of reaction mixture

Styrene/Heptane	Solubility Parameters of mixture [MPa ^{1/2}]			
	δ_d	δ_p	δ_h	δ
0/10 (Heptane)	14.9	0	0	14.9
1/9	15.6	0.1	0	15.6
4/6	16.6	0.4	0	16.6
6/4	17.3	0.6	0	17.3
8/2	17.9	0.8	0	18.0
10/0 (Styrene)	18.6	1	0	18.6

Figure 2.9 shows the series of typical phase changes of reaction mixture in slurry phase polymerization of sPS over homogeneous catalyst. At first, the reaction mixture is a clear liquid with no visible particle precipitation. As TSC increases to about 1 %, precipitation of polymer particles becomes visible and the reaction

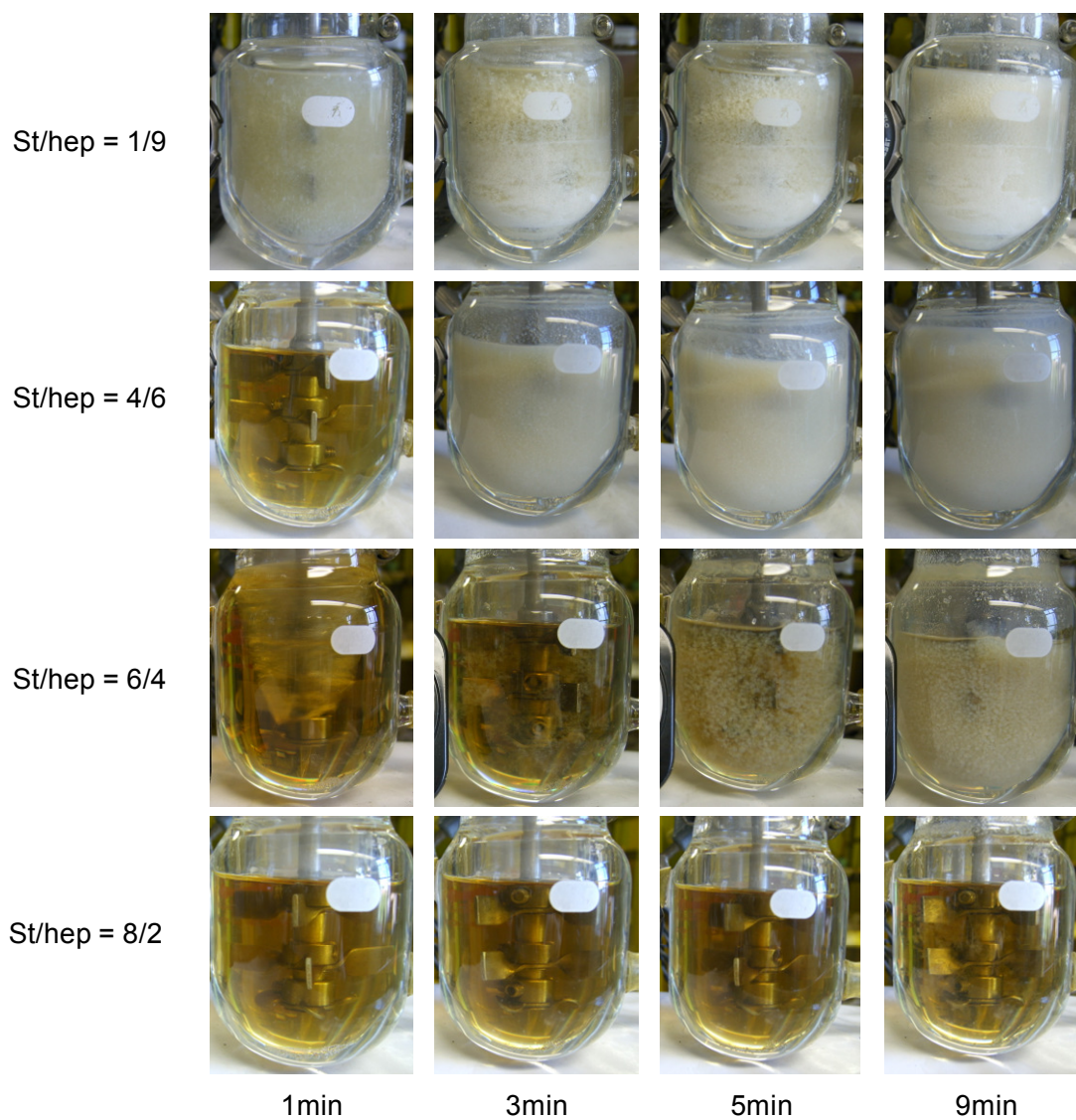


Figure 2.8 Physical phase changes of reaction mixture with different initial styrene to *n*-heptane ratio (Homogeneous reaction system, st/hep = v/v ratio, T = 70°C, [Ti] = 0.160 mmol/L, Al/Ti = 500).

mixture becomes turbid. Initially, the polymer precipitates are not hard and discrete particles. They begin to agglomerate to form soft or very low density aggregates.

These aggregates become larger as conversion increases and they look like 'marshmallows' (5 min in Figure 2.9). As TSC increases further, the collision of these agglomerates becomes more frequent and they become smaller and dense. Then, these solid particles imbibe the liquid and the reaction mixture becomes a wet cake-like material. Finally, the wet cake becomes dry particles (TSC = 25.8%).

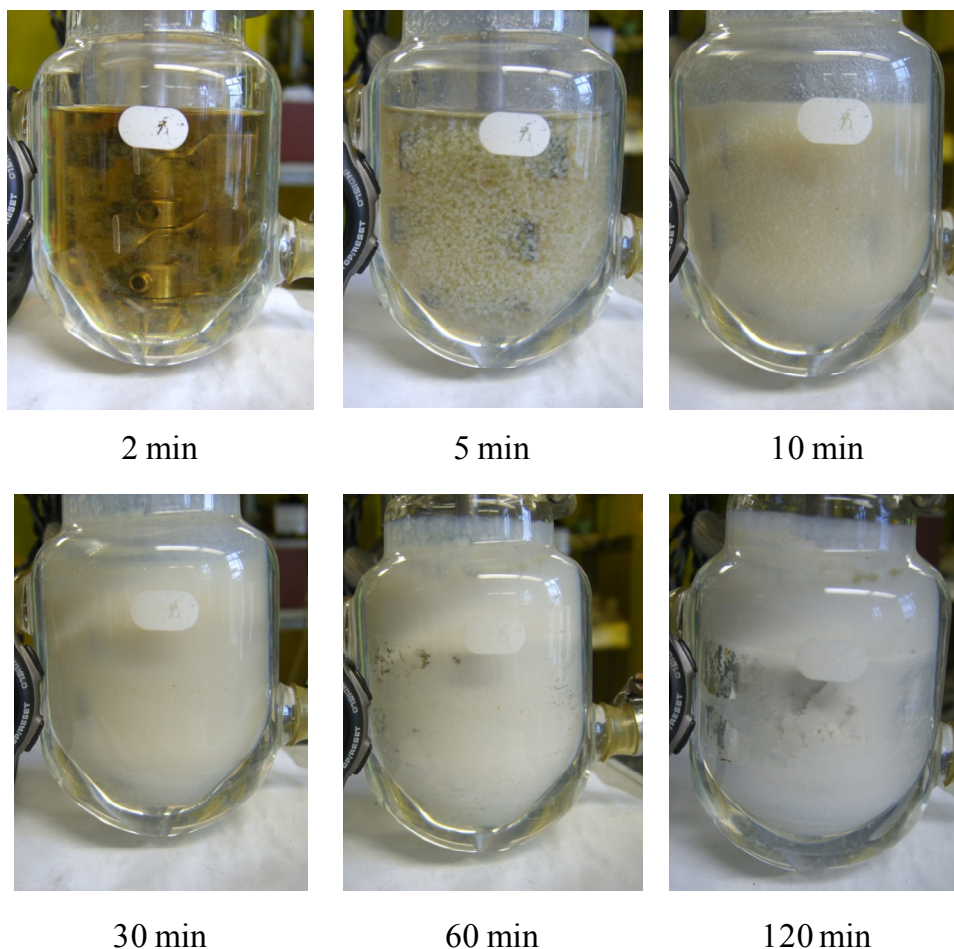


Figure 2.9 Physical phase changes during sPS polymerization over homogeneous catalyst, diluent = *n*-heptane, $[M]_0 = 5.02 \text{ mol/L}$, $[Ti] = 0.16 \text{ mmol-Ti/L}$, $T = 70^\circ\text{C}$.

2.3.3 Modified polymerization model for sPS polymerization over homogeneous catalyst

During the polymerization, reaction mixture undergoes physical phase changes from homogeneous liquid to slurry having discrete polymer particles. The phase changes of reaction mixture affect the polymerization kinetics, especially the non-linear dependency of monomer concentrations on the polymerization rate. To

analyze the non-linear rate dependence on monomer concentration, monomer sorption kinetics can be adopted. In ethylene or propylene polymerization in liquid slurry phase with transition metal catalysts, monomer partition occurs between the bulk liquid phase and the solid polymer particle phase [64]. In a bulk free radical polymerization of vinyl chloride, similar particle precipitation phenomena occur [65, 66]. For example, according to Patel *et al.* [67] who performed sorption experiments with poly vinyl chloride (PVC) particles and vinyl chloride in water, the monomer concentrations in the bulk liquid phase and in the solid phase are nonlinearly related. They fitted the experimental monomer sorption data with a Langmuir isotherm type monomer partition equation. In our work, we employ a similar empirical correlation for the partition of styrene between the bulk liquid phase ($[M]_b$) and the solid phase ($[M]_s$):

$$[M]_s = \frac{K_1[M]_b}{1 + K_2[M]_b} \quad (2-5)$$

If we adopt the form given by eq. (2-5), the polymerization rate is expressed as

$$R_p = k_p[M]_s[C^*] = \frac{k_p K_1[M]_b}{1 + K_2[M]_b} [C^*] \equiv \frac{k_p' [M]_b}{1 + K_2[M]_b} [C^*] \quad (2-6)$$

where $k_p' \equiv k_p K_1$ represents the effective propagation rate constant. We can rearrange eq. (2-6) as follows:

$$\frac{[C^*]_0}{R_{p0}} = \frac{K_2}{k_p'} + \frac{1}{k_p'} \frac{1}{[M]_{b0}} \quad (2-7)$$

Figure 2.10(a) shows the test of eq. (2-7) applied to the polymerization rate data in Table 2.2. Notice that the experimental data are well fitted by eq. (2-7). The kinetic parameter values obtained from Figure 2.10(a) are: $k_p' = 1.34 \times 10^5$ L/mol-hr, $K_2 = 0.192$ L/mol. Unfortunately, the value of K_1 cannot be obtained separately because it is not possible to directly measure the monomer concentration in the solid phase. Figure 2.10(b) illustrates the initial polymerization rate calculation with respect to initial monomer concentration by eq. (2-6). Simulation results agree well with the experimental data.

Catalyst deactivation rate constant also can be estimated using sorption mechanism. With the first-order deactivation kinetics, the polymerization rate equation can be expressed as follows:

$$R_p = \frac{k_p' [M]_b}{1 + K_2 [M]_b} [C^*]_0 e^{-k_d t} \quad (2-8)$$

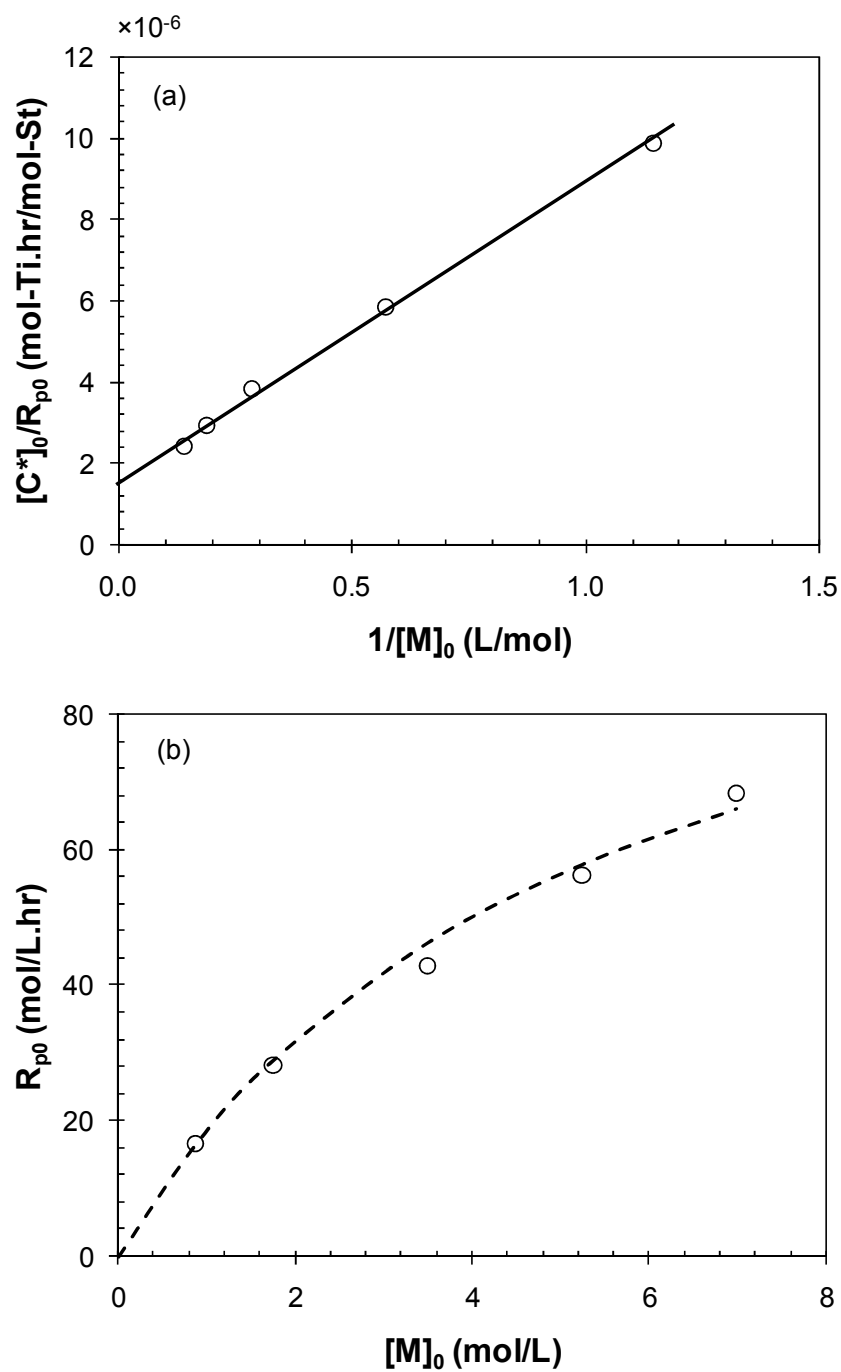


Figure 2.10 Polymerization rate analyses by adopting sorption kinetics; (a) Test of eq. (2-7), (b) Initial polymerization rate vs. initial monomer concentration (line: model calculation from eq. (2-6)).

Eq. (2-8) can be arranged to

$$\ln \frac{R_p (1 + K_2 [M]_b)}{k_p [M]_b [C^*]_0} = -k_d t \quad (2-9)$$

Figure 2.11 shows the test of eq. (2-9) applied to the polymerization rate data in Table 2.2. The deactivation rate constant value obtained at 70°C is $k_d = 3.83 \text{ hr}^{-1}$ ($t_{1/2} = 11 \text{ min}$). The deactivation rate constant value (3.83 hr^{-1}) obtained from eq. (2-8) is very similar to the deactivation constant value (3.59 hr^{-1}) obtained from Figure 2.7(b), because the catalyst deactivation mechanism is not affected by solid phase formation. Using the modified polymerization rate model (eq. (2-8)), the polymer yields are calculated (Figure 2.12). Overall, simulation results (dashed lines) and experimental data (symbols) are in good agreement.

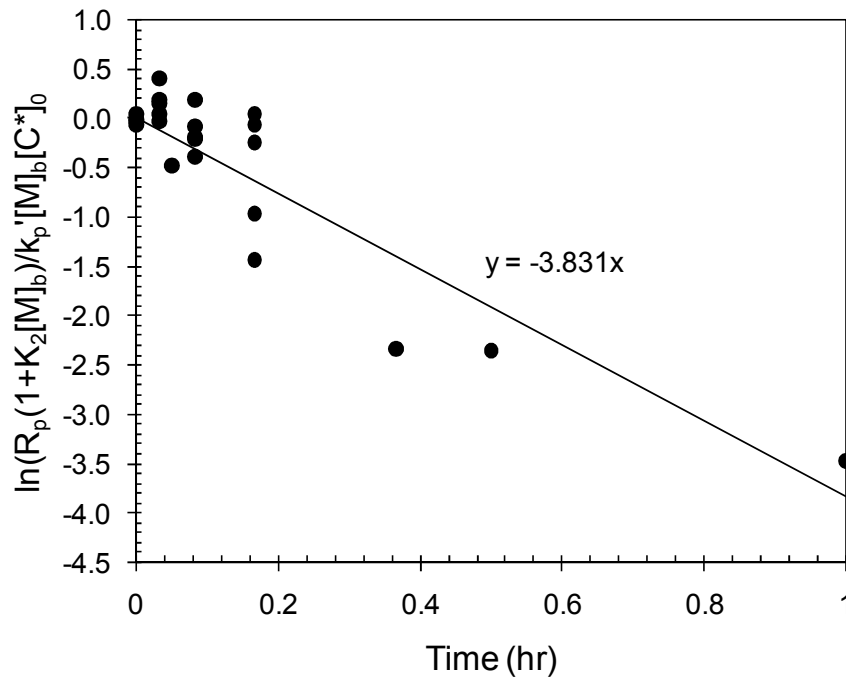


Figure 2.11 Test of eq. (2-9).

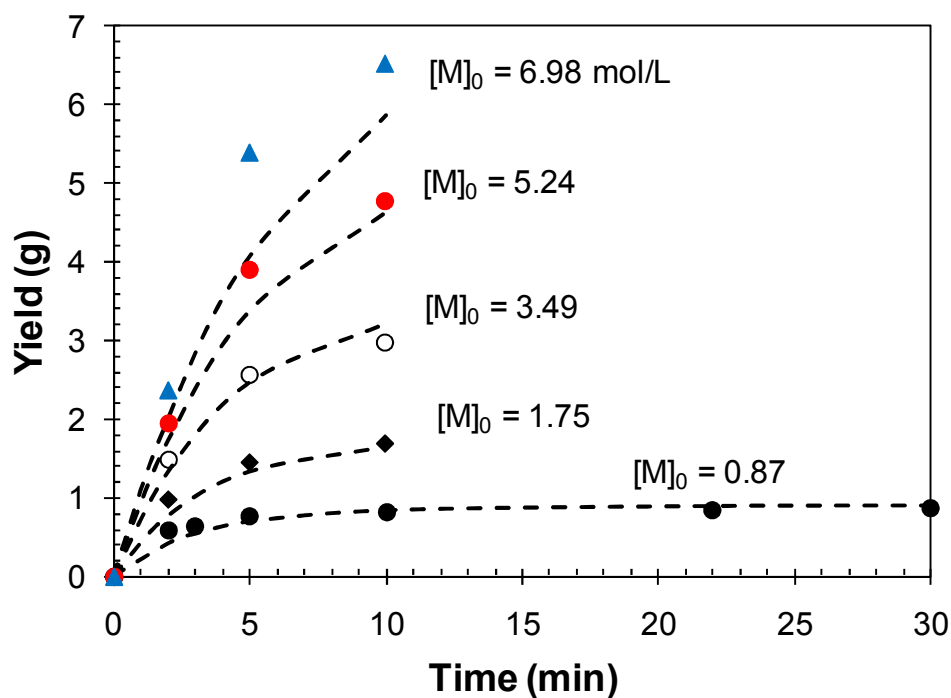


Figure 2.12 Polymer yields vs. reaction time (symbols: experimental data, lines: simulation results).

2.4 Conclusions

In this chapter, theoretical modeling analysis of the syndiospecific polymerization of styrene over homogenous $\text{Cp}^*\text{Ti}(\text{OCH}_3)_3/\text{MAO}$ catalyst was reported. Even with homogenous metallocene catalyst, liquid slurry polymerization was performed successfully. It has been observed that sPS polymerization rate is nonlinearly dependent on the bulk phase monomer concentration. To elucidate the reason of nonlinear dependency of polymerization rate on the monomer concentration, physical transitions of the reaction mixture in homogeneous metallocene catalyst

were also investigated. An sPS slurry undergoes a series of physical changes during the polymerization. At very low monomer conversion, the reaction mixture is a clear liquid with no visible particle precipitation. But as the total solid content (TSC) increases, precipitated polymer particles start to agglomerate and the reaction mixture becomes turbid. The polymer agglomerates are transformed to soft or low density aggregates which become larger as conversion increases. These polymer aggregates can absorb a large amount of solvent and monomer in the reactor. As TSC further increases, the amount of liquid (monomer and solvent) imbibed in the sPS particles increases such that the reaction mixture eventually becomes a wet cake or paste-like material. These physical changes of reaction mixture attribute to the partition of monomer between the solid and the liquid phases. We incorporated the monomer partition effect into our kinetic model and with monomer partition effect incorporated kinetic model, successfully simulated experimental results.

Chapter 3: Kinetics of Syndiospecific Polymerization of Styrene over Heterogeneous Metallocene Catalysts¹

3.1 Introduction

The polymerization of sPS with either homogeneous or heterogeneous metallocene catalyst is characterized by the precipitation of sPS because sPS does not dissolve in its own monomer (styrene) and organic solvents at typical reaction temperatures (e.g., $< 100^{\circ}\text{C}$). In sPS polymerization over a metallocene catalyst, polymer microparticles agglomerate as monomer conversion increases and these sPS agglomerates become a gel that is a wet-cake like material. With further increase in monomer conversion, the gel becomes hard. The sPS gel is not a chemically cross-linked gel but a physical gel. It is believed that strong intermolecular interactions between the polymer and monomer/solvent molecules are the main cause for the gelation. Once sPS gel is formed, the reaction mixture becomes extremely difficult to agitate by conventional means. Therefore, developing a polymerization process that can avoid the gelation is of an important industrial interest.

When a liquid slurry polymerization process is employed with heterogeneous catalysts, sPS can be recovered as discrete particles. One of the simple techniques to heterogenize a homogeneous metallocene catalyst is the catalyst embedding technique where active titanium-MAO complex is embedded into a homogeneous

¹ The main part of this chapter has been published in Han, J.J., H. W. Lee, W. J. Yoon and K. Y. Choi (2007). "Rate and molecular weight distribution modeling of syndiospecific styrene polymerization over silica-supported metallocene catalyst." *Polymer* **48**(22): 6519-6531.

mass of sPS pre-polymer [51, 68]. The sPS polymerization with the embedded catalyst showed that there was a range of polymerization conditions that allowed for the formation of sPS particles without significant particle agglomeration or gelation [52, 68].

Another simple and well known method is to anchor catalyst onto inorganic catalyst support such as a silica gel. There are four different methods of immobilizing metallocene catalyst onto silica surface: (a) absorption of methyl aluminoxane (MAO) on the support with subsequent addition of metallocenes in a second step, (b) absorption of a mixture of the metallocene and MAO to the support, (c) adsorption and immobilization of the metallocene to the support surface, and (d) direct bonding of metallocene to the support by a spacer and an anchor group [69]. These methods are represented in Figure 3.1. Method (c) can make higher molecular weight polymers, but alter stereospecificity due to interaction with surface electron donor group [70]. Method (d) has a difficulty in bonding the metallocene to the surface [70]. Method (a) does not significantly change the metallocene structure, thus the polymers produced by method (a) are very similar to those produced in a homogeneous system [69, 70].

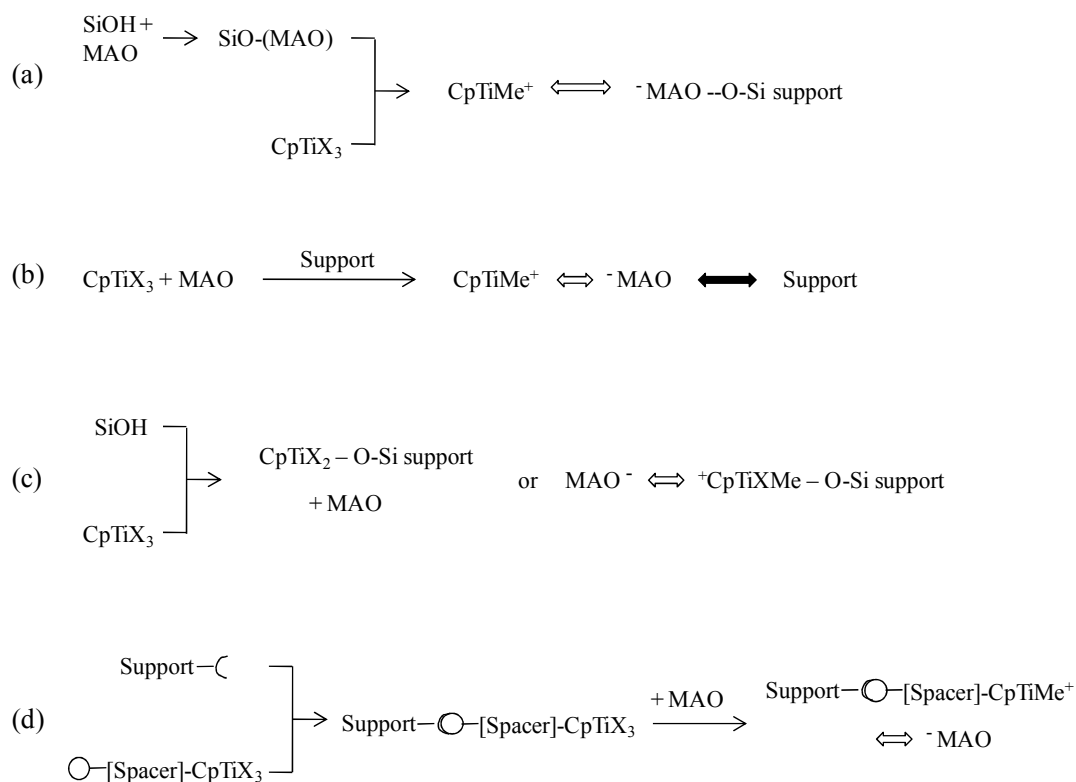


Figure 3.1 Methods for supporting metallocenes. [69]

3.2 Experimental

3.2.1 Materials

Styrene (Aldrich) was vacuum distilled over calcium hydride, and activated alumina was used to remove inhibitor from the monomer. *n*-heptane (Fisher Scientific) was used as a diluent, and it was purified by being refluxed over sodium and benzophenone in nitrogen atmosphere. Cp*Ti(OCH₃)₃ (Pentamethyl cyclopentadienyl titanium trimethoxide, Strem Chemicals, min 97%) and modified methyl aluminoxane (MMAO-3A, Akzo Nobel, 6.8 wt.% Al content) were used as supplied

without further purification. Silica gel (Davison 952, W.R. Grace) was used as a catalyst support.

Figure 3.2 (a) shows a scanning electron microscope (SEM) image of the Davison 952 silica surface used in this study. Figure 3.2 (a) shows that the silica support consists of multilevel aggregates of 2-10 nm-diameter primary silica particles [71, 72]. The primary silica particles or spheroids are formed during the polymerization of silicic acid solution and the subsequent aggregation of colloidal silica. These spheroids aggregate and form larger clusters. The pores for the diffusion of monomer and the growth of polymers are provided by the channels between the primary particles and the channels between the clusters. Figure 3.2 (b) is the pore size distribution of the Davison 952 silica particles [Courtesy of W.R. Grace and Company, Columbia, MD]. The average pore diameter is 20 nm and the pores larger than 30 nm are practically absent.

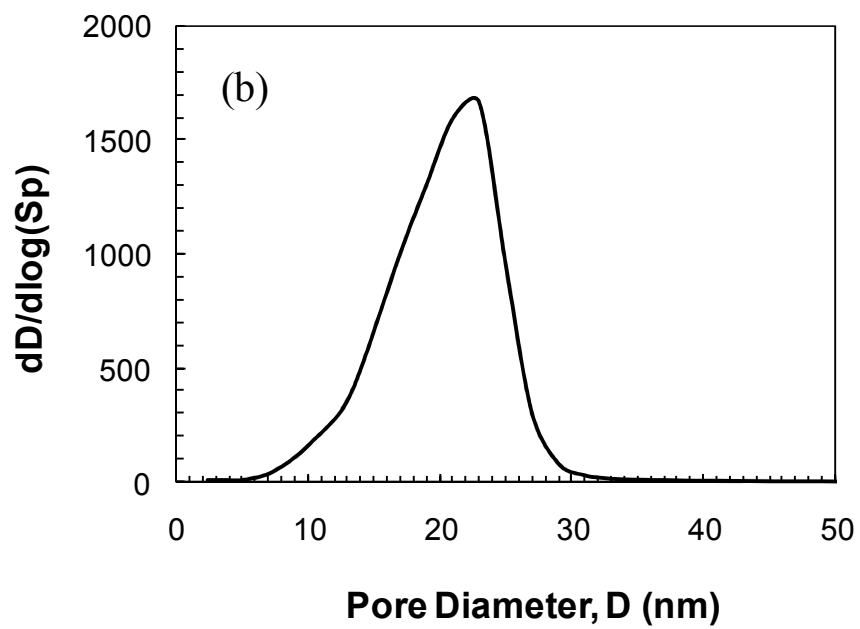
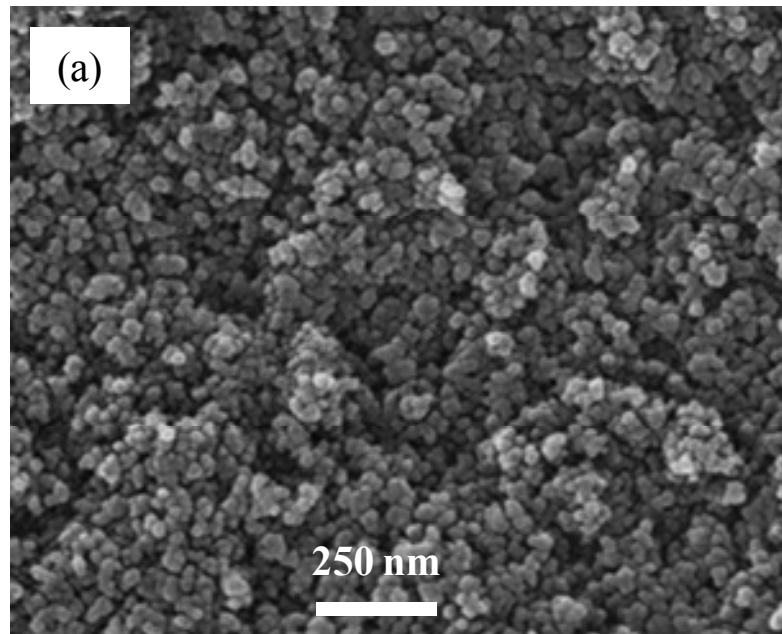


Figure 3.2 (a) SEM image of Davison 952 silica gel particle and (b) the pore size distribution (Courtesy of W.R. Grace and Company).

3.2.2 Preparation of silica-supported metallocene catalysts

In our experiments, method (a) in Figure 3.1 is used to anchor metallocene catalyst onto silica support. Figure 3.3 shows the mechanism of supporting step of $\text{Cp}^*\text{Ti}(\text{OCH}_3)_3$ on silica pretreated with MAO. MAO is first absorbed to the support and bonded with surface silanol groups. Then, the methoxy group of $\text{Cp}^*\text{Ti}(\text{OCH}_3)_3$ is complexed with aluminums in MAO.

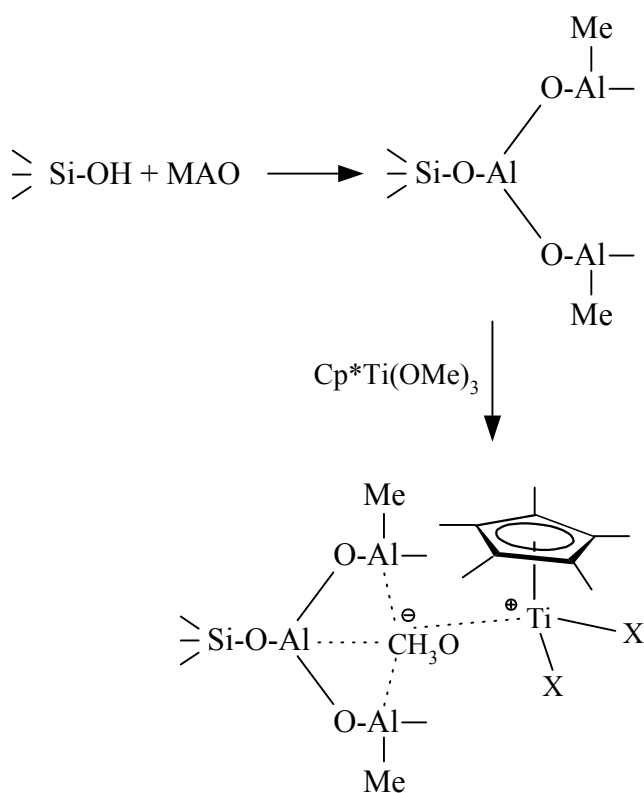


Figure 3.3 Mechanism of supporting step of $\text{Cp}^*\text{Ti}(\text{OCH}_3)_3$ on silica pretreated with MAO ($\text{X} = \text{CH}_3$).

In Figure 3.4, silica-supported metallocene catalyst preparation step is illustrated. Firstly, silica gel particles were calcined in an oven at 250°C for 24 hr under nitrogen atmosphere. The calcined silica gel was then treated with a MMAO solution (1.6 mmol of MMAO and 20 mL of toluene per 1 g of silica gel) at 50°C for 1.5 hr, washed with excess toluene three times, and dried *in vacuo* overnight. Then, the MMAO/silica particles were mixed with Cp*Ti(OCH₃)₃ catalyst solution (0.5 mmol of Cp*Ti(OCH₃)₃ and 35mL of toluene per 1 g of MMAO-silica) at 50°C for 1 hr, washed with toluene three times, and dried *in vacuo* for 24 hr. The Al and Ti loadings were measured by inductively coupled plasma emission spectroscopy (ICP): 1.30×10^{-3} mol-Al/g-catalyst and 2.92×10^{-4} mol-Ti/g-catalyst.

3.2.3 Styrene polymerization with silica-supported Cp*Ti(OCH₃)₃/MAO catalyst

Syndiospecific polymerization of styrene experiments were carried out using an 100 mL jacketed glass reactor equipped with a stainless steel agitator. Figure 3.4 shows the simple schematic diagram of reactor system. Predetermined amounts of monomer, solvent, silica-supported catalyst, and MMAO were charged into the reactor in a glove box (for detail experimental conditions, see Table 3.1). All the polymerization experiments were carried out at 70°C, and the agitator speed was maintained constant during the polymerization. The Al/Ti mole ratio was fixed at 350 and 500. After polymerization, the reaction mixture was removed from the reactor, washed with excess amount of acidified methanol (10 vol. % of hydrochloric acid),

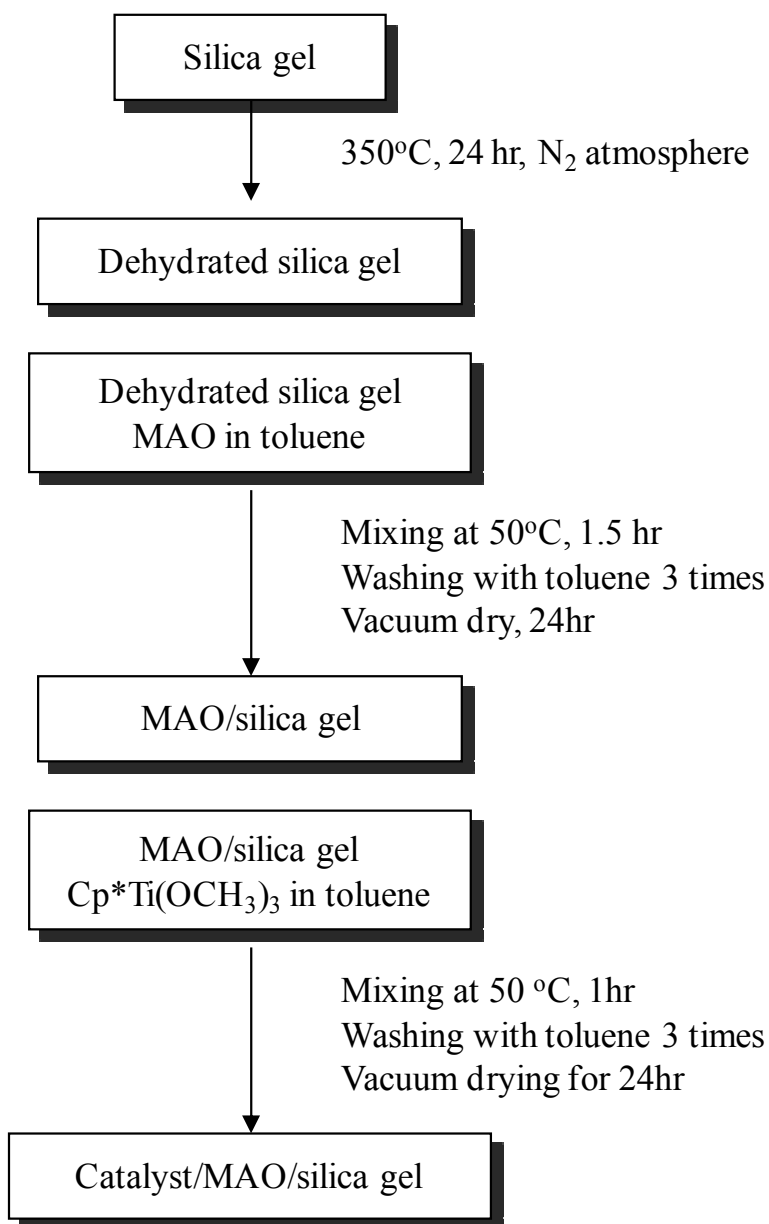


Figure 3.4 Preparation of silica-supported catalyst.

and dried *in vacuo*. Since the reactor has no provisions for sampling during the polymerization, the polymer yield vs. time profiles were obtained by conducting the individual experiments with same reaction conditions but terminated at different reaction times. The monomer conversion was determined gravimetrically by measuring the polymer weight for a known amount of initial monomer and diluent. The total solid content (TSC) was determined by measuring the weight of the initial reaction mixture and the weight of the polymer produced. Most of the sPS samples obtained in our experiments had the methyl ethyl ketone (MEK) insoluble fraction of 91-98%, indicating high degree of syndiotacticity. The number and weight average molecular weight were determined by gel permeation chromatography (GPC) (Polymer Laboratories, PL GPC220) with 1,2,3-trichlorobenzene at 135°C using PLgel[®] 10µm MIXED-B and PLgel[®] 10µm GUARD columns (Polymer Laboratories).

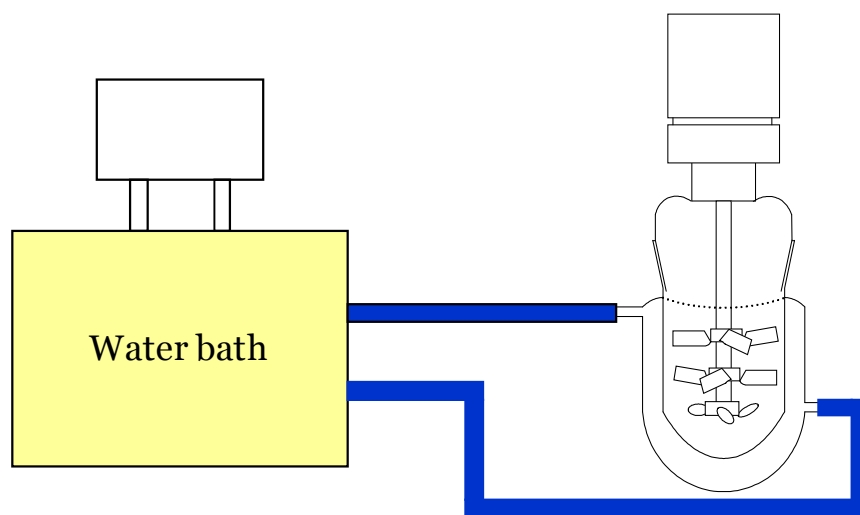


Figure 3.5 The schematic diagram of 100 mL glass reactor system.

3.3 Results and Discussion

3.3.1 Polymerization rate analysis

We carried out styrene polymerization experiments at different monomer and catalyst concentrations. The same batch of catalyst was used in all these experiments to minimize the run-to-run variations in catalyst activity. Table 3.1 is a summary of experimental results of twenty polymerization runs at 70 °C. We use the same amount of catalyst and Al/Ti mole ratio in all these experiments.

Effect of monomer concentration

In our first series of polymerization experiments, the effect of bulk phase monomer concentration on the polymer yield and polymerization rate was investigated. Figure 3.6(a), (b), and (c) show the polymer yield, monomer conversion and polymerization rate data (symbols) obtained for four different initial styrene concentrations ($[M]_{b0}$). For each polymerization experiment, monomer conversions and remained monomer concentrations were calculated from polymer yield data. The polymerization rate values were determined by averaging the slopes of two adjacent points for each data point with ORIGIN[®] package (OriginLab, Ver. 7.5). Since the polymerization was carried out in a batch reactor, the decrease in the polymerization rate was due to the consumption of monomer as well as the catalyst deactivation. The polymerization rate data shown in Figure 3.6(c) indicates that initial polymerization rate does not increase linearly in proportion to the initial monomer concentration.

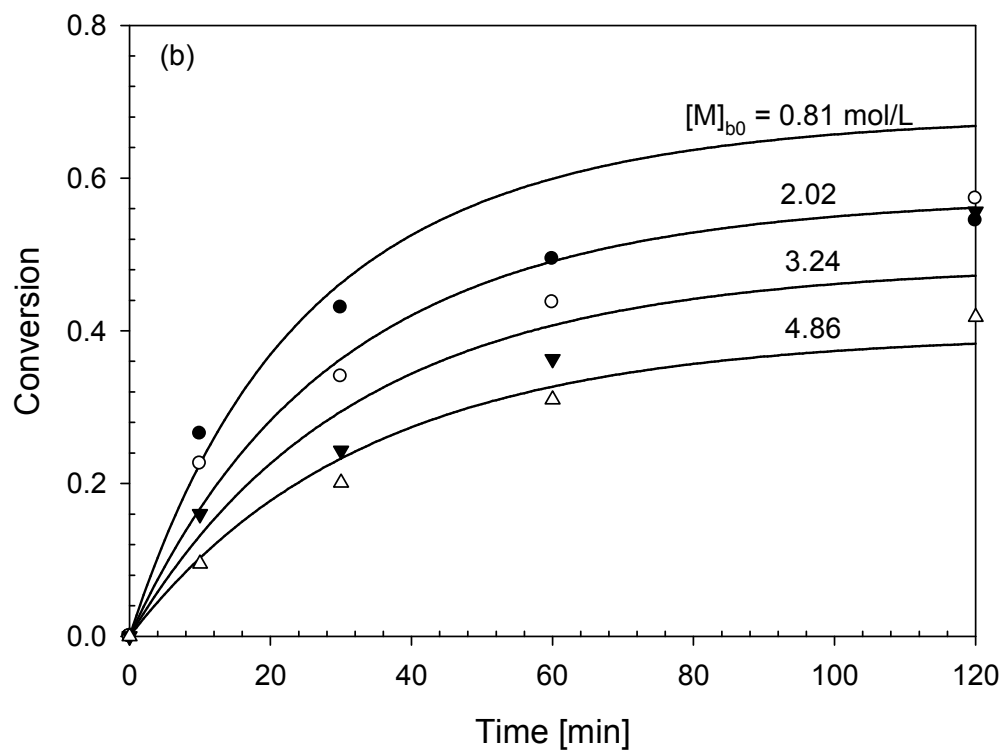
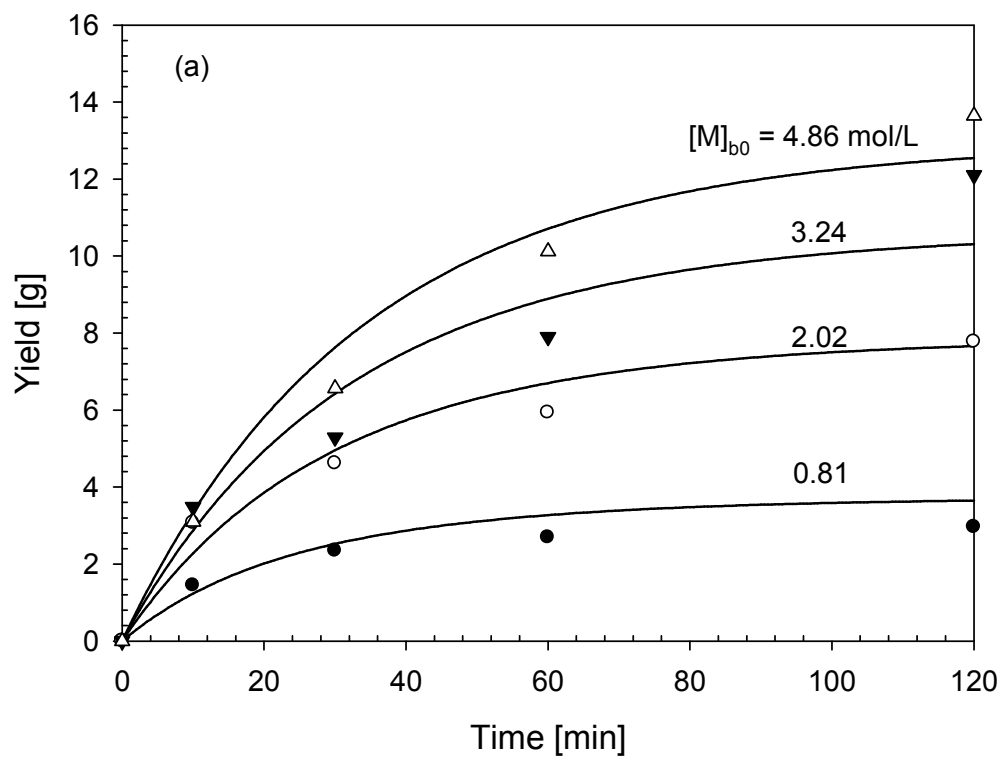
This observation suggests that the sPS polymerization rate deviates from the first-order kinetics with respect to monomer concentration.

Table 3.1 Reaction conditions and experimental data of sPS polymerization with silica-supported metallocene catalyst

Run ID	[M] _{bo}	[Ti] ×10 ⁴	St. Vol. %	Reaction Time	Yield	TSC	Avg. Activity ×10 ⁻³	Mw × 10 ⁻⁵	PDI
[-]	[mol/L]	[mol/L]	[%]	[min]	[g]	[w/w%]	[g-sPS/mol-Ti.min]	[g/mol]	[-]
1-1	0.81	2.62	10	10	1.45	4.9%	8.58	1.32	4.10
1-2				30	2.34	6.9%	4.62		
1-3				60	2.69	7.7%	2.65		
1-4				120	2.97	8.2%	1.46		
2-1	2.02	2.62	25	10	3.08	8.1%	18.22	1.70	3.06
2-2				30	4.64	11.3%	9.15		
2-3				60	5.96	14.1%	5.88		
2-4				120	7.81	17.9%	3.85		
3-1	3.24	2.62	40	10	3.49	8.6%	20.65	2.65	3.74
3-2				30	5.30	12.2%	10.45	2.42	3.04
3-3				60	7.92	17.4%	7.81	2.21	3.24
3-4				120	12.14	25.8%	5.99	2.39	3.71
4-1	4.86	2.62	60	10	3.11	7.4%	18.40	3.15	3.44
4-2				30	6.59	14.0%	13.00		
4-3				60	10.13	20.7%	9.99		
4-4				120	13.66	27.4%	6.74		
C-1	2.03	0.35	25	15	0.01	0.0%	0.31		
C-2		0.70			0.34	0.6%	5.35		
C-3		1.37			1.31	2.2%	10.34		
C-4		2.68			4.28	7.1%	16.88		
C-5		3.92			6.83	11.4%	17.93		

* 60 mL of styrene and n-heptane was used.

** [Al]/[Ti] = 500 (1-1 to 4-4), [Al]/[Ti] = 350 (C-1 to C-5)



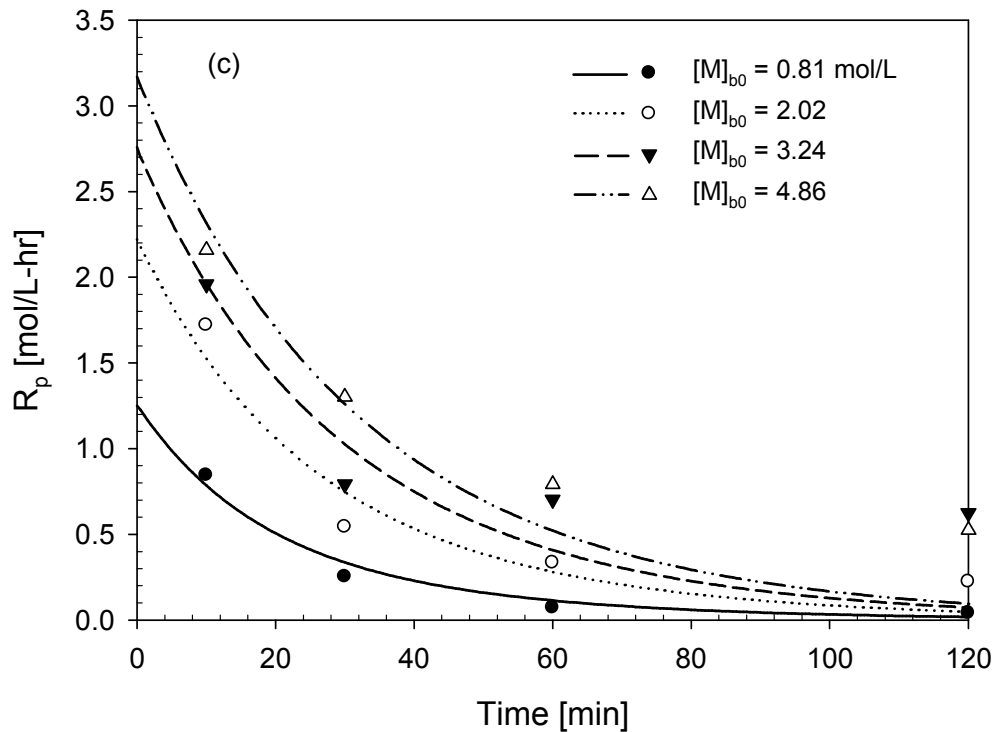


Figure 3.6 Effect of initial monomer concentration on polymer yield, monomer conversion, and polymerization rate at 70 °C (symbols - data (●, 0.81 mol/L; ○, 2.02 mol/L; ▼, 3.24 mol/L; Δ, 4.86 mol/L), lines - model).

To determine the dependence of polymerization rate on the monomer concentration, initial polymerization rates are plotted against initial monomer concentrations as shown in Figure 3.7. The initial polymerization rate values were estimated by extrapolating the polymerization rate data to $t = 0$. It is observed that the initial polymerization rate increases almost linearly in proportion to monomer concentration up to about 2.0 mol/L. At monomer concentrations higher than 2.0 mol/L, polymerization rate is little dependent on the monomer concentration. The

data shows that the initial polymerization rate tends to level off for the initial monomer concentrations higher than 2.0 mol/L. Since catalyst deactivation effect can be assumed negligible at the beginning of polymerization, the results shown in Figure 3.6 suggest that some other effects might have influenced the polymerization rate. Similar phenomena were observed in styrene polymerization with other heterogeneous catalyst systems (e.g., embedded catalysts [52]).

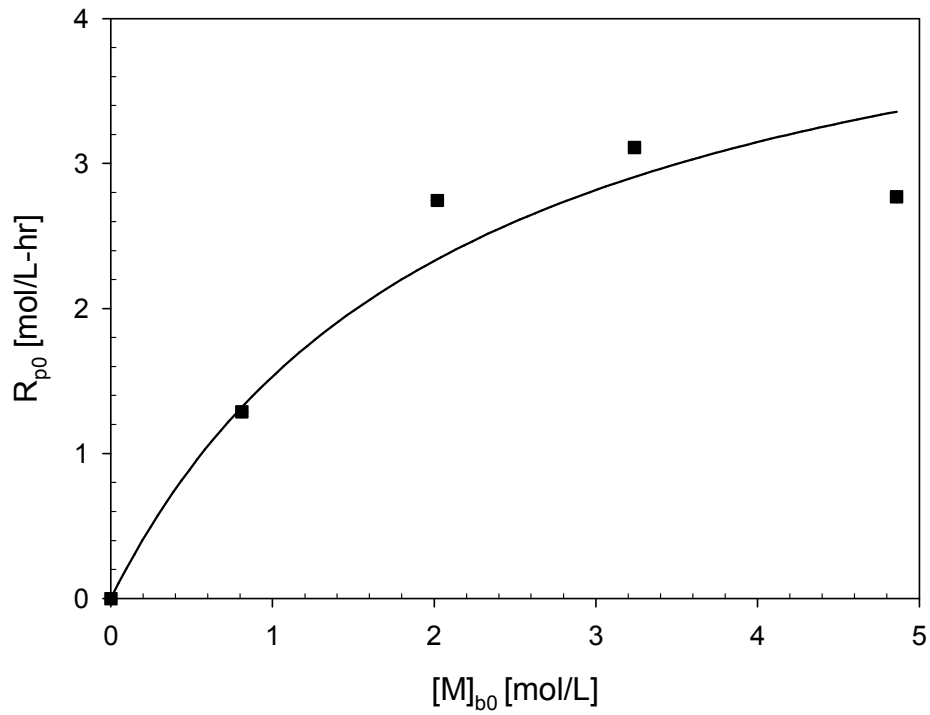


Figure 3.7 Initial polymerization rates vs. initial monomer concentration (■, data; dashed line, model calculations from eq. (3-20)).

Effect of catalyst concentration

The effect of catalyst concentration on the initial polymerization has also been investigated and the results are shown in Figure 3.8. At very low catalyst concentrations (e.g., $< 0.5 \times 10^{-4}$ mol/L, cf. for homogeneous catalyst, $[\text{Ti}]_{\text{crit}} = 0.6 \times 10^{-4}$ mol/L), very little amount of polymer was produced. It is probably because at such low catalyst concentrations, the catalyst might have been deactivated by the impurities present in the liquid phase with very little sites left available for polymerization. Over the range of catalyst concentration we tested (i.e., $[\text{Ti}] > 0.5 \times 10^{-4}$ mol/L), the sPS polymerization rate shows the first order dependence on the initial catalyst concentration.

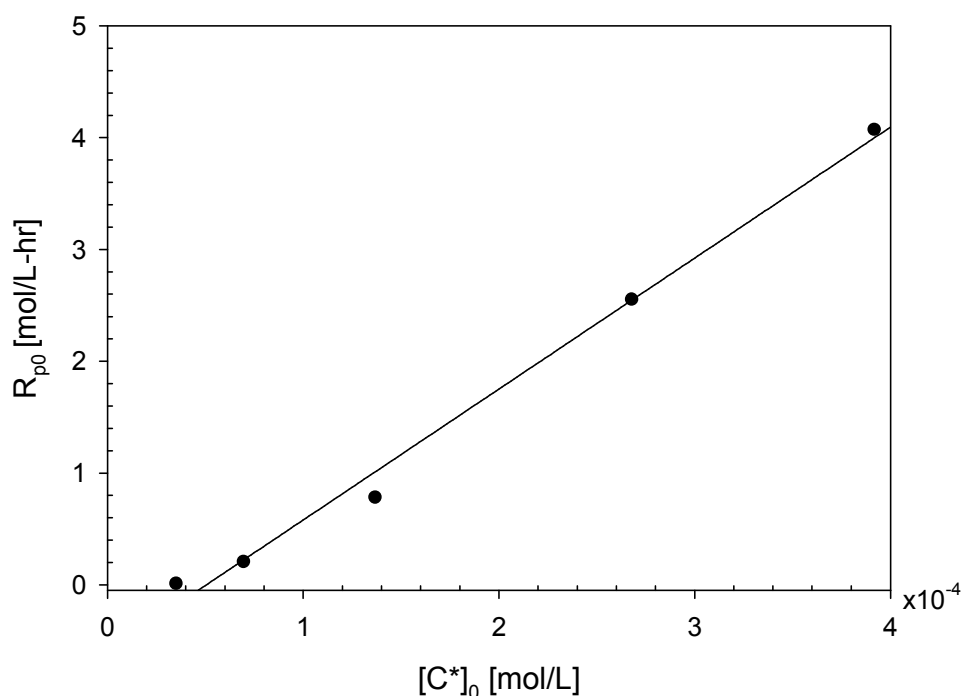


Figure 3.8 Polymerization rate vs. initial catalyst concentration ($[\text{M}]_{b0} = 2.03$ mol/L, Reaction time = 15 min, $T = 70^\circ\text{C}$, $\text{Al/Ti} = 350$).

Kinetic model

To further analyze the polymerization rate behaviors observed in our experiments, reaction kinetic model is developed as follows:

Catalyst site activation:



Propagation:



Chain transfer to monomer:



β -hydrogen elimination:



Catalyst deactivation:



where C_0 is the potent catalyst site, C^* is the activated catalyst site, P_n and M_n are the live and dead polymer chains of length n , M is the monomer, and D^* is the

deactivated catalyst site. k_j represents the reaction rate constant for each corresponding reaction. We assume that catalyst activation reaction (eq. (3-1)) is very fast. To calculate the molecular weight averages, polymer molecular weight moment equations are needed. The polymerization rate equations and the polymer molecular moment equations are derived as follows.

$$\frac{d[C^*]}{dt} = -k_d[C^*] - k_p[C^*][M]_s + k_{t\beta}\lambda_{p0} \quad (3-6)$$

$$\frac{d[M]_s}{dt} = -k_p[P][M]_s - k_{tM}[P][M] \approx -k_p[P][M]_s \quad (3-7)$$

$$\frac{d[P_1]}{dt} = k_p[C^*][M]_s - k_p[P_1][M]_s - k_{tM}[P_1][M]_s + k_{tM}\lambda_{p0}[M]_s - k_{t\beta}[P_1] - k_d[P_1] \quad (3-8)$$

$$\frac{d[P_n]}{dt} = k_p([P_{n-1}] - [P_n])[M]_s - k_{tM}[P_n][M]_s - k_{t\beta}[P_n] - k_d[P_n] \quad (n \geq 2) \quad (3-9)$$

$$\frac{d[M_n]}{dt} = k_d[P_n] + k_{t\beta}[P_n] + k_{tM}[P_n][M]_s \quad (n \geq 2) \quad (3-10)$$

$$\frac{d\lambda_{p0}}{dt} = k_p[C^*][M]_s - k_{t\beta}\lambda_{p0} - k_d\lambda_{p0} \quad (3-11)$$

$$\frac{d\lambda_{M0}}{dt} = k_{t\beta}\lambda_{p0} + k_d\lambda_{p0} + k_{tM}\lambda_{p0}[M]_s \quad (3-12)$$

$$\frac{d\lambda_{P1}}{dt} = k_p[C^*][M]_s + k_p\lambda_{P0}[M]_s + k_{tM}[M]_s(\lambda_{P0} - \lambda_{P1}) - k_{t\beta}\lambda_{P1} - k_d\lambda_{P1} \quad (3-13)$$

$$\frac{d\lambda_{M1}}{dt} = k_{t\beta}\lambda_{P1} + k_{tM}\lambda_{P1}[M]_s + k_d\lambda_{P1} \quad (3-14)$$

$$\frac{d\lambda_{P2}}{dt} = k_p[C^*][M]_s + k_p[M]_s(2\lambda_{P1} + \lambda_{P0}) - k_{t\beta}\lambda_{P2} + k_{tM}[M]_s(\lambda_{P0} - \lambda_{P2}) - k_d\lambda_{P2} \quad (3-15)$$

$$\frac{d\lambda_{M2}}{dt} = k_{t\beta}\lambda_{P2} + k_{tM}\lambda_{P2}[M]_s + k_d\lambda_{P2} \quad (3-16)$$

where the k-th moments of live and dead polymers are defined as $\lambda_{Pk} \equiv \sum_{n=1}^{\infty} n^k [P_n]$ and

$\lambda_{Mk} \equiv \sum_{n=1}^{\infty} n^k [M_n]$, respectively. $[P]$ is the total live polymer concentration and

$$[P] = \lambda_{P0}.$$

Number-average and weight-average molecular weights are calculated using the following equations:

$$\bar{M}_n = \frac{\lambda_{P1} + \lambda_{M1}}{\lambda_{P0} + \lambda_{M0}} (mw)_{sty} \approx \frac{\lambda_{M1}}{\lambda_{M0}} (mw)_{sty} \quad (3-17)$$

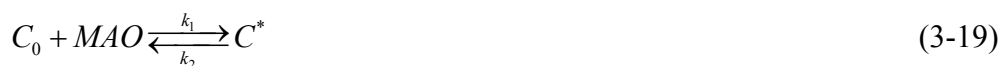
$$\bar{M}_w = \frac{\lambda_{P2} + \lambda_{M2}}{\lambda_{P1} + \lambda_{M1}} (mw)_{sty} \approx \frac{\lambda_{M2}}{\lambda_{M1}} (mw)_{sty} \quad (3-18)$$

where $(mw)_{sty}$ represents the molecular weight of styrene. Notice that in eqs. (3-17)

and (3-18), the contributions of live polymers to overall molecular weight averages

are ignored because the concentrations of live polymers are far smaller than the concentration of dead polymers. Also, in the above kinetic model, we assumed that the catalyst is a single site catalyst. Later in our discussion, we shall examine the validity of this assumption.

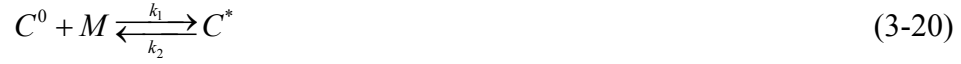
In the mathematical derivation of the foregoing polymerization model, the monomer concentration $[M]_s$ represents the monomer concentration at the catalytic sites in the solid phase. In a heterogeneous reaction system such as considered in this work, it is possible that the monomer concentration in the bulk liquid phase ($[M]_b$) may not be same as that in the solid phase. Recall that in Figure 3.7, we have observed the deviation of the initial polymerization rate from the first order dependence on the bulk phase monomer concentration. The non-linear rate dependence of polymerization rate on monomer concentration is often observed in other catalyzed polymerization processes such as ethylene slurry polymerization with metallocene catalysts [73]. But the polymerization rate patterns observed in our system and liquid slurry ethylene polymerization systems reported in the literature are different. For example, in ethylene polymerization, reversible complex formation [1] occurs between an active site and a monomer molecule, leading to the transition from the second-order kinetics to the first-order kinetics as monomer concentration is increased.



Bergstra and Weickert [73] introduced another complex formation mechanism. From their slurry phase ethylene polymerization with heterogeneous metallocene

catalyst experiments, they stated that uncomplexed active site is complexed with monomer.

Complex formation



where C^0 is unoccupied catalyst site.

With a steady state approximation, activated catalytic site can be obtained as

$$\frac{dC^*}{dt} = k_1 C^0 M - k_2 C^* = 0 \rightarrow C^* = \frac{k_1}{k_2} C^0 M \quad (3-21)$$

The total catalyst concentration is:

$$C_t = C^* + C^0 \rightarrow C^0 = \frac{k_2}{k_2 + k_1 M} C_t \quad (3-22)$$

Combining eq. (3-21) and (3-22), catalytic active site can be calculated as

$$C^* = \frac{K_A M}{1 + K_A M} C_t \quad (3-23)$$

where K_A is k_1/k_2 , and polymerization rate is expressed as:

$$R_p = k_p C^* M = k_p C_t \frac{K_A M^2}{1 + K_A M} \quad (3-24)$$

Propagation rate constant (k_p), two equilibrium parameter (K), catalyst deactivation rate constant (k_d), and complex formation equilibrium constant (K_A) were estimated by non-linear least squares regression method in MATLAB package.

Figure 3.9 shows one of simulation results for polymer yield vs. reaction time. In our polymerization, the polymerization shows the first-order kinetics ($R_p \propto [M]$) at low monomer concentrations ($[M]_{b0} < 2.0$ mol/L) but the polymerization rate deviates from the first-order kinetics as monomer concentration is increased (e.g. $[M]_{b0} > 2.0$ mol/L). As shown in Figure 3.9, however, polymerization rate by simulation with reversible active site formation mechanism cannot match the experimental data.

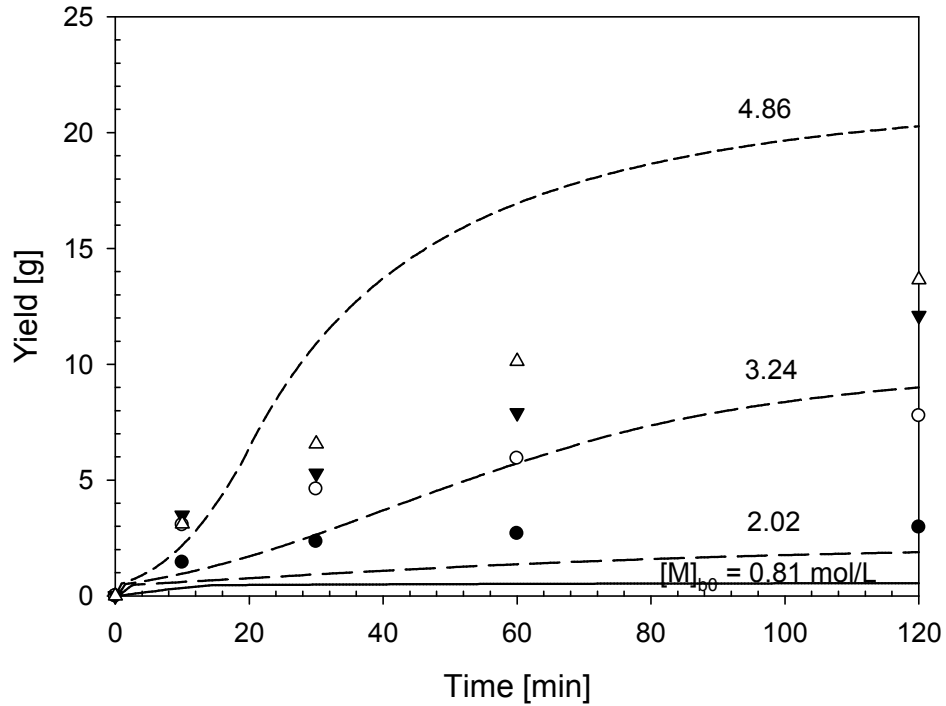


Figure 3.9 Polymer yield profiles vs. reaction time calculated with reversible active site formation mechanism (lines: simulation results, symbols: experimental data).

To analyze the non-linear rate dependence on monomer concentration, we propose that the monomer concentration in the solid phase (liquid-swollen polymer

phase) is nonlinearly related to the monomer concentration in the bulk liquid phase. In ethylene or propylene polymerization in liquid slurry phase with transition metal catalysts, monomer partition occurs between the bulk liquid phase and the solid polymer particle phase [64]. Other researchers [67] fitted the experimental monomer sorption data with a Langmuir isotherm type monomer partition equation. In our work, we employ a similar empirical correlation for the partition of styrene between the bulk liquid phase ($[M]_b$) and the solid phase ($[M]_s$):

$$[M]_s = \frac{K_1[M]_b}{1 + K_2[M]_b} \quad (3-25)$$

According to eq. (3-25), the monomer concentration in the solid phase increases linearly with the bulk phase concentration at low $[M]_b$ but it approaches the saturation value (i.e., $[M]_{sat} = K_1 / K_2$ at high $[M]_b$). If we adopt the form given by eq. (3-25), the polymerization rate is expressed as

$$R_p = k_p[M]_s[C^*] = \frac{k_p K_1 [M]_b}{1 + K_2 [M]_b} [C^*] \equiv \frac{k_p' [M]_b}{1 + K_2 [M]_b} [C^*] \quad (3-26)$$

where $k_p' \equiv k_p K_1$ represents the effective propagation rate constant. We can rearrange eq. (3-26) as follows:

$$\frac{[C^*]_0}{R_{p0}} = \frac{K_2}{k_p'} + \frac{1}{k_p'} \frac{1}{[M]_{b0}} \quad (3-27)$$

Figure 3.10 shows the test of eq. (3-27) applied to our polymerization rate data. Notice that the experimental data are well fitted by eq. (3-27). The kinetic

parameter values obtained from Figure 3.10 are: $k_p' = 8.15 \times 10^3$ L/mol-hr, $K_2 = 0.47$ L/mol. Unfortunately, the value of K_1 cannot be obtained separately because it is not possible to directly measure the monomer concentration in the solid phase.

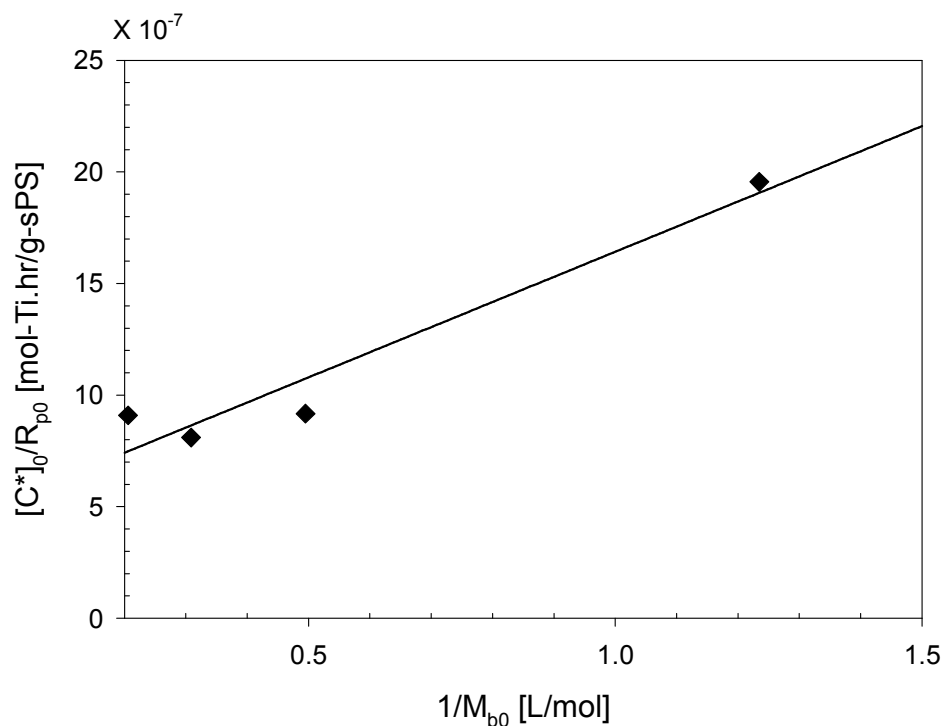


Figure 3.10 Test of eq. (3-27).

Another factor that can contribute to the decrease in the polymerization rate is catalyst deactivation. Although the site deactivation mechanisms and kinetics are not well understood for most of the transition metal catalyzed olefin polymerization processes, first-order deactivation kinetics has been generally well accepted. If we

assume the first-order deactivation kinetics, the polymerization rate equation can be expressed as follows:

$$R_p = \frac{k_p [M]_b}{1 + K_2 [M]_b} [C^*]_0 e^{-k_d t} \quad (3-28)$$

Eq. (3-28) can be arranged to

$$\ln \frac{R_p (1 + K_2 [M]_b)}{k_p [M]_b [C^*]_0} = -k_d t \quad (3-29)$$

Figure 3.11 shows the test of eq. (3-29) applied to the polymerization rate data in Table 3.1. The deactivation rate constant value obtained at 70°C is $k_d = 1.67 \text{ hr}^{-1}$ (half life $t_{1/2} = 25 \text{ min}$).

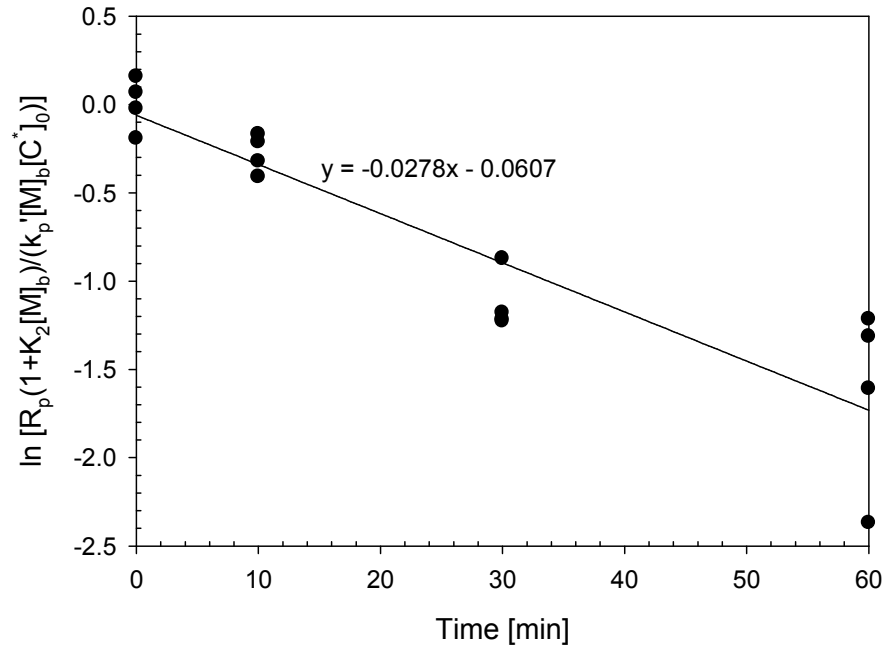


Figure 3.11 Test of eq. (3-29).

Note that propagation rate constant (k_p ') and deactivation rate constant (k_d) values of heterogeneous catalyst system is smaller than those of homogeneous catalyst system (k_p ' = 1.34×10^5 L/mol-hr, k_d = 3.83 hr^{-1} for homogeneous catalyst system). In general, propagation rate of silica-supported catalyst system is much smaller than that of homogeneous catalyst system because only catalytic active sites placed on the surface of silica particle are utilized at the early stage of polymerization. After silica support fragmentation, catalytic sites located in the core of silica particles are activated and involve polymerization reaction. Similarly, deactivation of active catalytic sites is also retarded because many catalytic sites are occluded inside the silica particles.

We used the modified polymerization rate model (eq. (3-26)) to calculate the polymer yield and the results are shown in Figure 3.5 (a) and (b). The model simulation results (lines) show that the proposed polymerization rate model yields a good fit of the experimental data (symbols). The predictions of initial polymerization rates at different monomer concentrations are also shown in Figure 3.5(b). The model tends to underpredict the polymerization rate at $t = 120$ min.

3.3.2 Physical changes during polymerization

The physical phase of reaction mixture changes during sPS polymerization. In Chapter 2, we observed that weak intermolecular interactions between solvent molecules and phenyl rings in main polymer chains help avoiding global gelation and

concluded selection of diluent is very important in slurry polymerization of sPS. To examine the effect of solvent on the physical phase changes of reaction mixture, four different solvents – *n*-hexane, *n*-heptane, toluene and ethylbenzene - were used in the polymerization experiments. Table 3.2 shows the solubility parameters of solvents, and styrene monomer. Toluene and ethylbenzene and styrene have similar solubility parameter values, whereas the solubility parameters of *n*-hexane and *n*-heptane are quite different from that of styrene. This means that toluene and ethylbenzene can interact strongly with phenyl groups of polystyrene main chains, and sPS will have weaker interactions with *n*-hexane and *n*-heptane. Thus, with *n*-hexane or *n*-heptane, discrete sPS particles can be formed easier than with toluene and ethylbenzene.

Table 3.2 Solubility parameters of solvents, styrene monomer [74]

	Solubility Parameter [MPa ^{1/2}]			
	δ_d	δ_p	δ_h	δ
Hexane	14.9	0	0	14.9
Heptane	15.3	0	0	15.3
Ethylbenzene	17.8	0.6	1.4	17.8
Toluene	18	1.4	2	18.2
Styrene	18.6	1	0	18.6

Table 3.3 summarized the results of sPS polymerization experiments with silica-supported catalyst using an 100 mL stirred reactor.

Figure 3.12 shows the photo-images of the reaction mixtures undergoing physical phase changes in different solvents. For aliphatic hydrocarbon diluents – *n*-hexane and *n*-heptane, larger amount of solvent can generate discrete sPS particles (Figure 3.12(b)) faster than smaller amount of solvent (Figure 3.12(d)). However,

when toluene and ethylbenzene were used, solvent amount was not an important factor to change phase of reaction mixture because the solubility parameter values of both solvents are similar to that of styrene (Figure 3.12 (a) and 3.12 (c)).

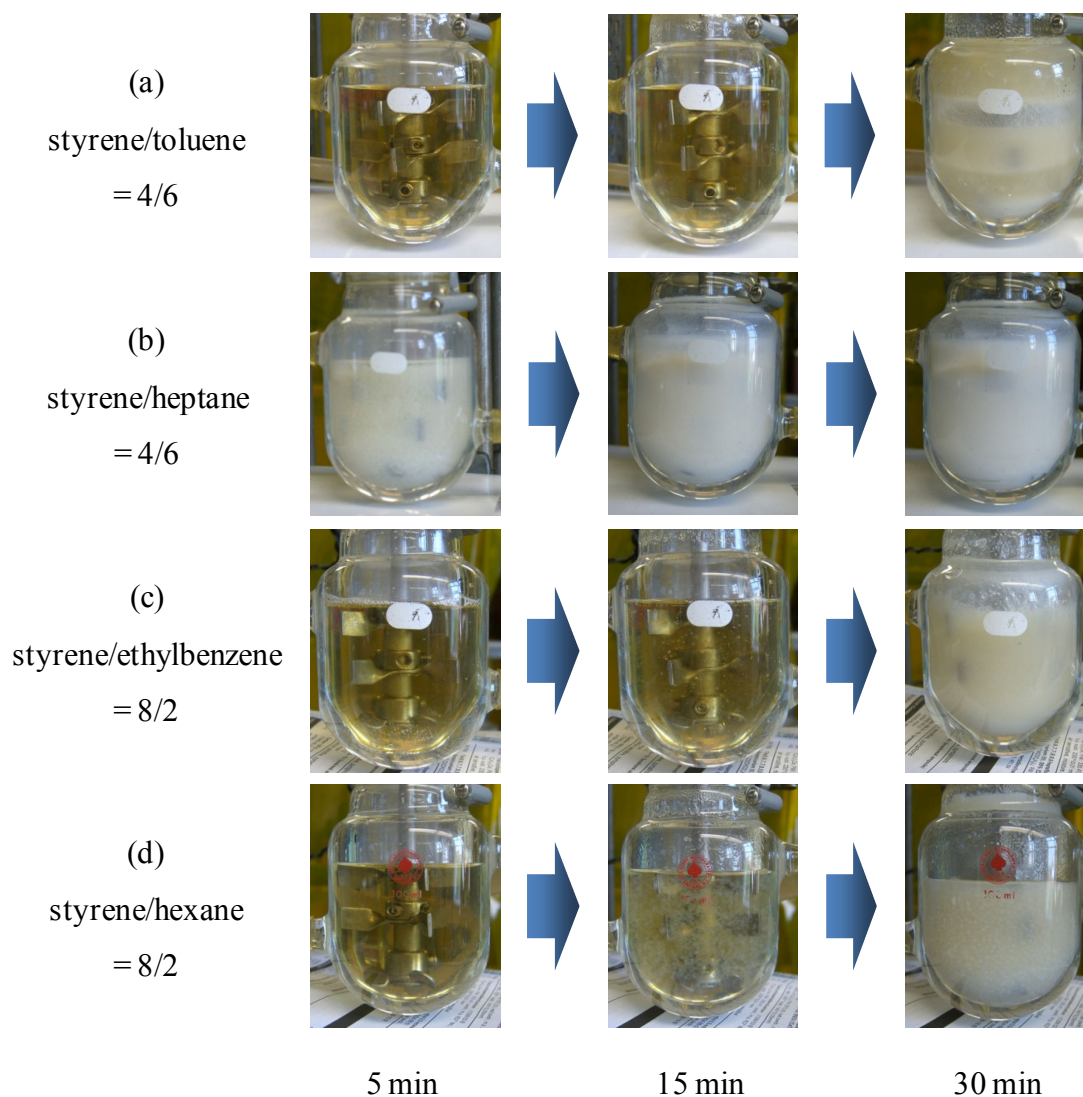


Figure 3.12 photo-images of phase changes during sPS polymerization in different solvents with silica-supported $\text{Cp}^*\text{Ti}(\text{OCH}_3)_3/\text{MAO}$ catalyst.

Thus, the solubility parameter of reaction mixture changes a little during polymerization. When styrene/heptane volume ratio is 4/6, sPS particles were formed

in 5 min and their shape was stable. When, however, styrene/toluene volume ratio is same to styrene/*n*-heptane ratio, discrete particle formation time is over 20 min. Note that in all cases, global gelation was suppressed. *n*-hexane and *n*-heptane diluents promoted discrete sPS particle formation. Thus, aliphatic hydrocarbon solvents and heterogenized catalyst system are very useful to avoid global gelation in syndiospecific polymerization of styrene.

Table 3.3 sPS polymerization data in different solvents

Solvent	Styrene/solvent	Reaction time	TSC	Remarks
	(v/v ratio)	(min)	(w/w%)	
Hexane	8/2	30	7.8	marsh mallows
Heptane	4/6	30	8.4	wet powder
	6/4	5	3.6	marsh mallows
		10	7.4	dense aggregates
		30	12.2	wet powder
		60	17.4	dry powder
Ethylbenzene	8/2	30	10.4	wet powder + gel
Toluene	4/6	60	17.2	dry powder + gel

* T = 70 °C, [Al]/[Ti] = 500

Figure 3.13 shows a schematic illustration of the physical changes of the reaction mixture we have observed with silica-supported metallocene catalyst. Figure 3.14 illustrates the reaction mixture at different solid contents during the polymerization with *n*-heptane diluent. At very low TSC, the reaction mixture is a clear liquid with no visible particle precipitation. As TSC increases to about 1 %, precipitation of polymer particles becomes visible and the reaction mixture becomes turbid. Initially, the polymer precipitates are not hard and discrete particles. They

begin to agglomerate to form soft or very low density aggregates (Figure 3.14(a)). These aggregates become larger as conversion increases and they look like 'marshmallows' (Figure 3.14(b)). As TSC increases further, the collision of these agglomerates becomes more frequent and they become smaller and dense (Figure 3.14(c)). Then, these solid particles imbibe the liquid and the reaction mixture becomes a wet cake-like material (Figure 3.14(d)). At this stage, a separate liquid phase is no longer visible and polymer particles are wetted by the liquid (solvent and monomer). When the initial styrene concentration was high (i.e., small solvent volume fraction), the wet cake eventually became dry particles (Figure 3.14(e), (f)). Indeed, when we opened the reactor after experiment, the reactor was filled with relatively dry particles with no liquid phase (diluent and styrene) (Figure 3.14(f)). It was a quite interesting series of physical changes.

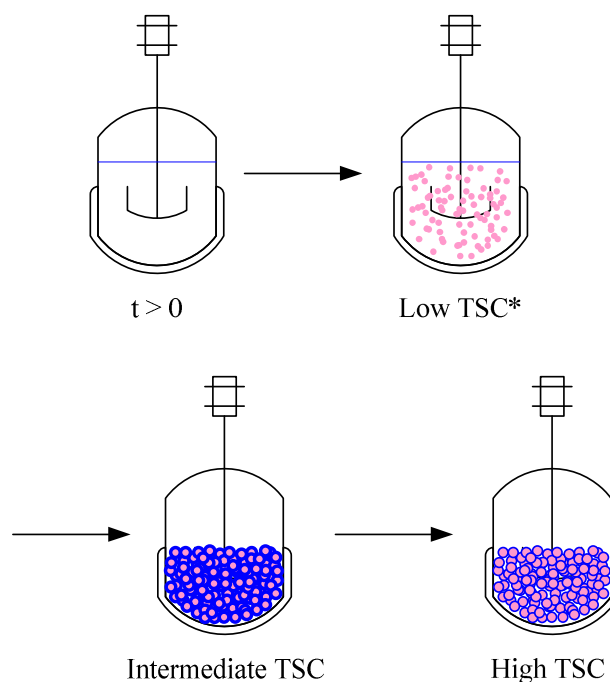


Figure 3.13 Schematic illustration of the sPS slurry polymerization process.

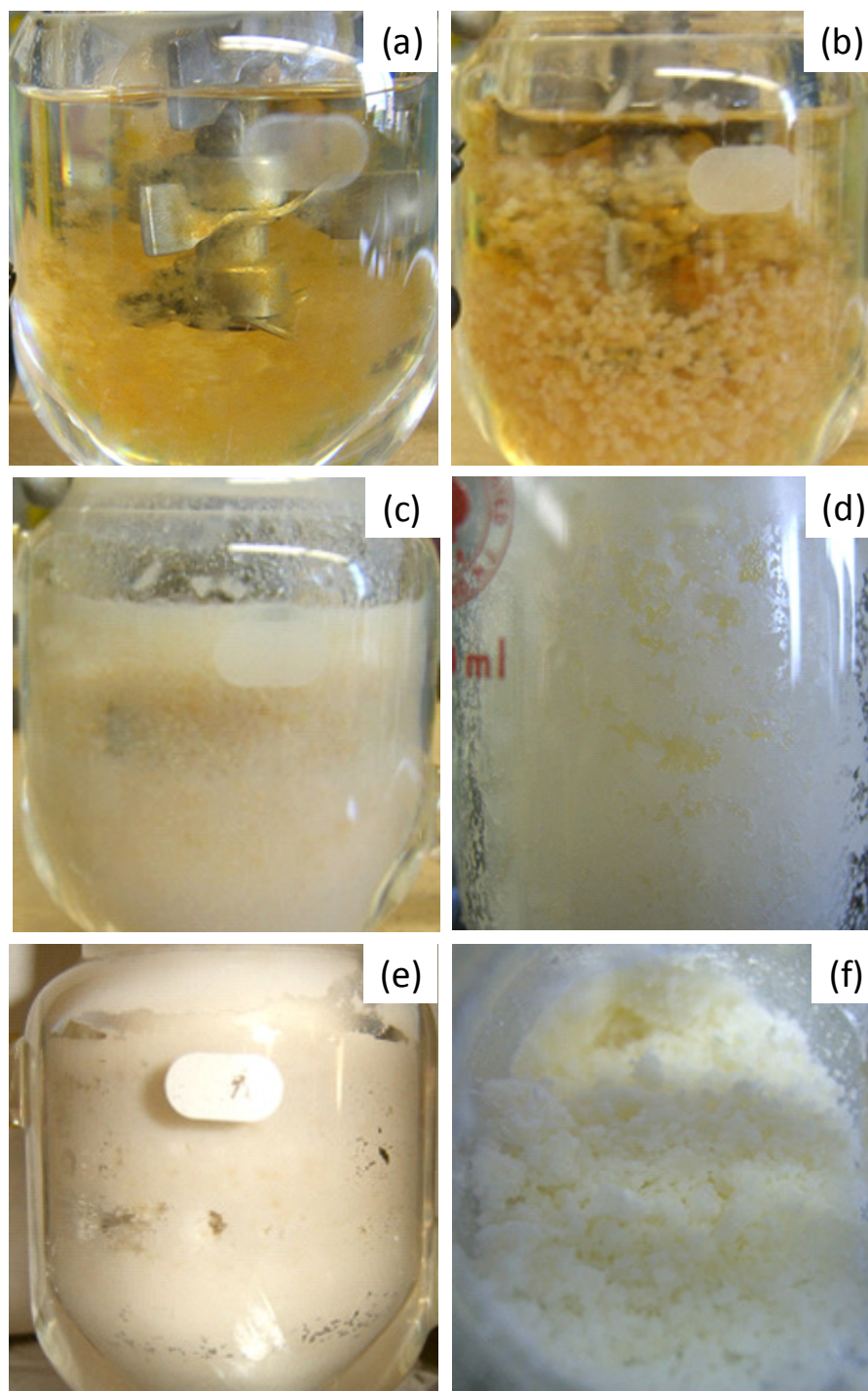


Figure 3.14 The photographs of physical phases of a polymerization mixture (a) TSC = 0.8 w/w %; (b) TSC = 3.6 w/w%; (c) TSC = 8.71 w/w% (d) TSC = 12.4 w/w%; (e) TSC = 20.5 w/w% (f) TSC = 19.1 w/w%.

To measure the amount of liquid imbibed in sPS, we carried out absorption experiments with sPS particles. Dried sPS particles were charged into glass vials and a styrene-solvent mixture was doled out to each vial. The glass vial was immersed in a constant temperature bath. After a vial was removed from the bath at a predetermined sampling time, the solid-liquid mixture was filtered and the weight of the liquid swollen polymer particles was measured. Table 3.4 shows the results of adsorption experiments

Table 3.4 Adsorption experimental data

styrene/heptane (v/v ratio)	styrene concentration (mol/L)	absorbed amount (ml)	Φ (ml/g)
0/10	0.00	3	6
2.5/7.5	2.18	3.35	6.7
5/5	4.36	3.6	7.2
7.5/2.5	6.55	3.7	7.4
10/0	8.73	3.8	7.6

* 0.5 g of sPS and 5 mL of solution were used in each experiment

Figure 3.15 shows the amount of absorbed styrene-solvent mixture in sPS solid phase. The amount of liquid absorbed in one gram of sPS polymer (Φ) is fitted by the following equation:

$$\Phi = 6.2 + 0.18[M]_b \quad (3-30)$$

Using eq. (3-30), we can calculate the volumes of bulk liquid and solid phases with reaction time. The total slurry volume (V_{slurry}) is represented by

$$V_{slurry} = \frac{W_M}{\rho_M} + \frac{W_D}{\rho_D} + \frac{W_{sPS}}{\rho_{sPS}} \quad (3-31)$$

where ρ_M , ρ_D , and ρ_{sPS} are the densities of monomer, diluent and sPS respectively.

The liquid phase volume is calculated by

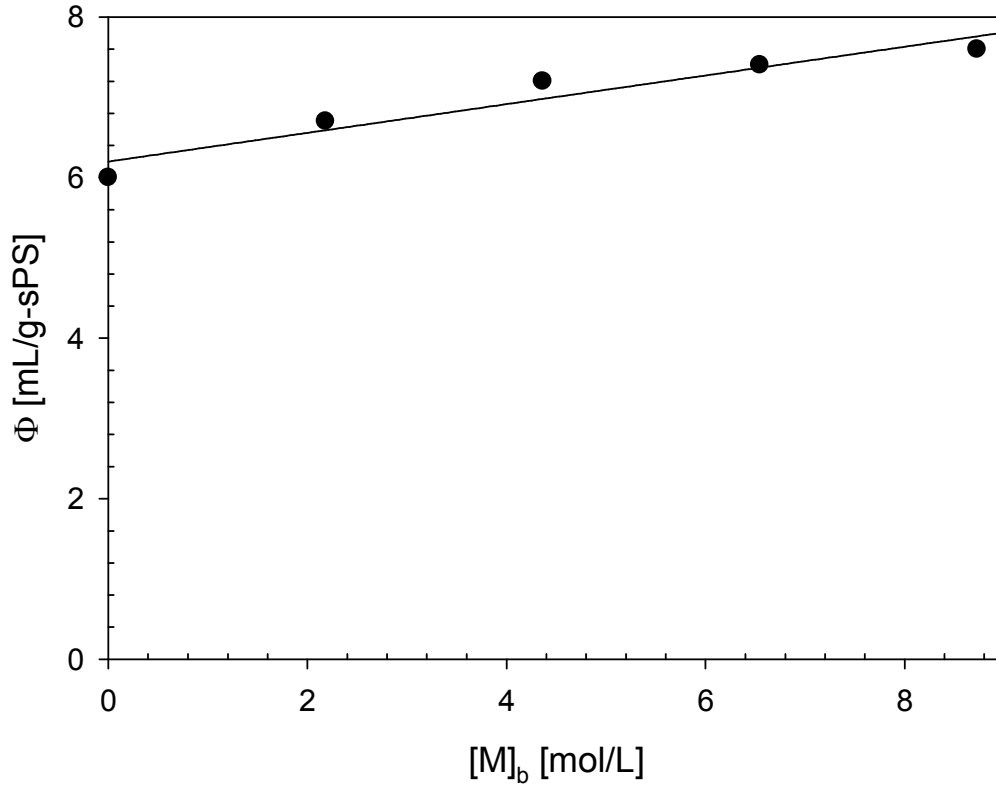


Figure 3.15 The amount of styrene-*n*-heptane mixture absorbed in sPS polymer (T = 70 °C; ●, data; line, regression).

$$V_L = V_{slurry} - \Phi W_{sPS} - \frac{W_{sPS}}{\rho_{sPS}} \quad (3-32)$$

Then, the change in the slurry phase volume with reaction time is represented as

$$\frac{dV_{slurry}}{dt} = \frac{1}{\rho_M} \frac{dW_M}{dt} + \frac{1}{\rho_{sPS}} \frac{dW_{sPS}}{dt} = \left(\frac{1}{\rho_{sPS}} - \frac{1}{\rho_M} \right) V_{slurry} R_p \quad (3-33)$$

Eq. (3-33) was solved with the kinetic model equations. Figure 3.16 (a) and (b) show the calculated volume fractions of liquid phase and the total solid content for different initial styrene concentrations. Volume fraction of liquid phase (f_L) was calculated as

$$f_L = \frac{V_L}{V_{slurry}} \quad (3-34)$$

Figure 3.16 (a) shows that at high initial monomer concentrations, a separate liquid phase disappears after about 35 min ($[M]_{b0} = 4.86$ mol/L) or 50 min ($[M]_{b0} = 3.24$ mol/L) at which the total solid contents are 15.7 wt.% and 16.5 wt.%, respectively (Figure 3.16 (b)). This means that after about 15 wt. % of TSC, only dry particles with no liquid exist in the reactor. The results in Figure 3.16 (a) match the visual observations as shown in Figure 3.14. Figure 3.16 (a) also indicates that slurry phase is always maintained at low initial monomer concentrations (e.g., $[M]_{b0} < 2.02$ mol/L) because the amount of sPS particles produced is not sufficient to absorb the whole liquid.

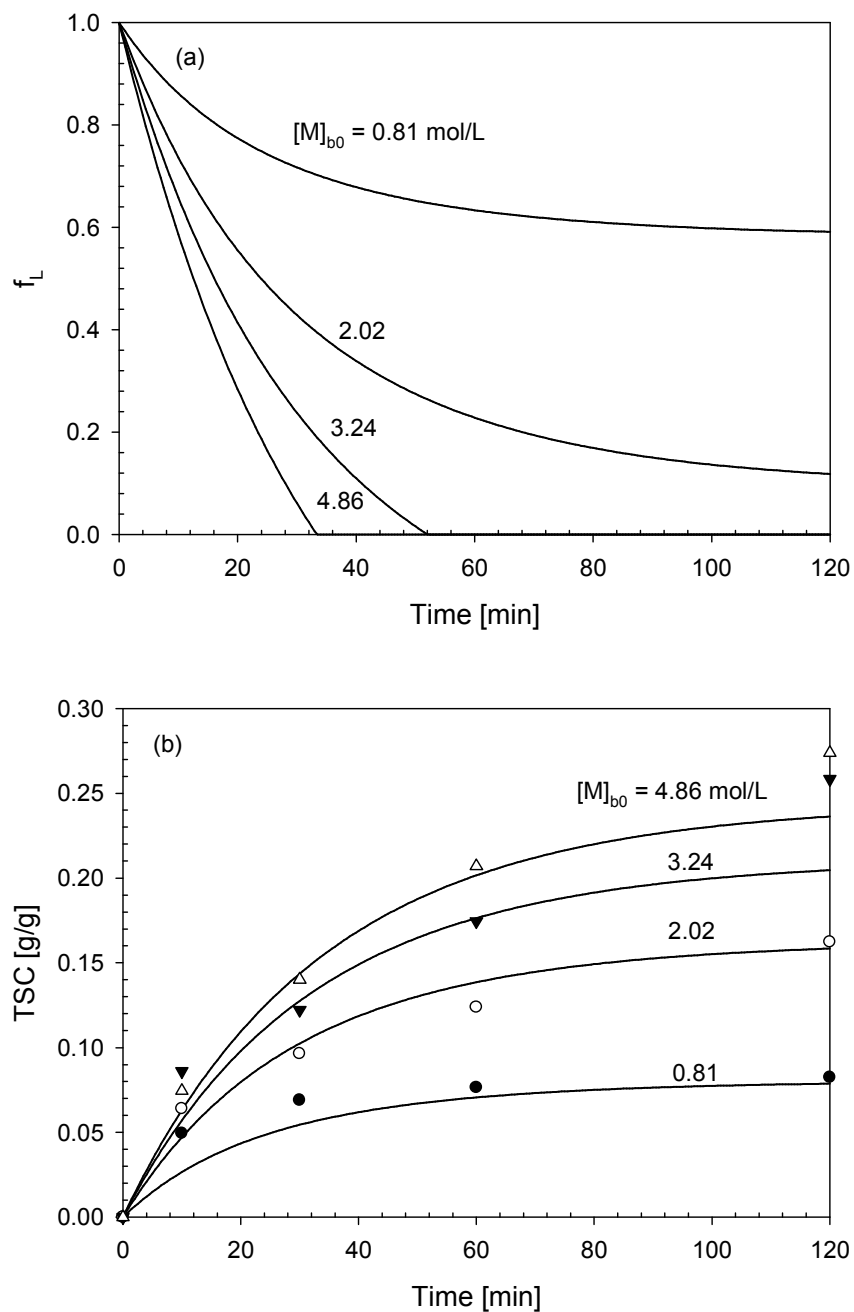


Figure 3.16 (a) The volume fraction of liquid phase vs. reaction time; (b) the TSC profiles vs. reaction time (symbols - data (●, 0.81 mol/L; ○, 2.02 mol/L; ▼, 3.24 mol/L; Δ, 4.86 mol/L), lines - model).

3.3.3 Molecular weight distribution analysis

We also investigated the effect of reaction time and monomer concentration on the polymer molecular weight and molecular weight distribution. Figure 3.17 (symbols) shows the experimental data of molecular weight averages with reaction time for the initial monomer concentration of 3.24 mol/L. As commonly observed in many other addition polymerization processes, both the number-average (\bar{M}_n) and the weight average (\bar{M}_w) molecular weight values increase rapidly in short reaction time at the beginning of polymerization and then slightly decrease with time. Figure 3.18 shows the effect of monomer concentration on \bar{M}_n and \bar{M}_w . In this graph, we used the effective bulk monomer concentration calculated from the monomer conversion data ($[M]_b = (1 - X)[M]_{b0}$). The molecular weight average values are those after 30 min of reaction.

Notice that the molecular weight increases with an increase in monomer concentration (Figure 3.18). In olefin polymerization processes with either Ziegler-Natta or metallocene catalysts, polymer molecular weight is not influenced by the bulk phase monomer concentration when the chain transfer to monomer is the dominant mode of chain transfer reaction (i.e., $\bar{X}_n \approx k_p / k_{tM}$; eq. (3-35')). The dependence of sPS molecular weight on styrene concentration suggests that other chain transfer reactions such as β -hydrogen elimination might be also important.

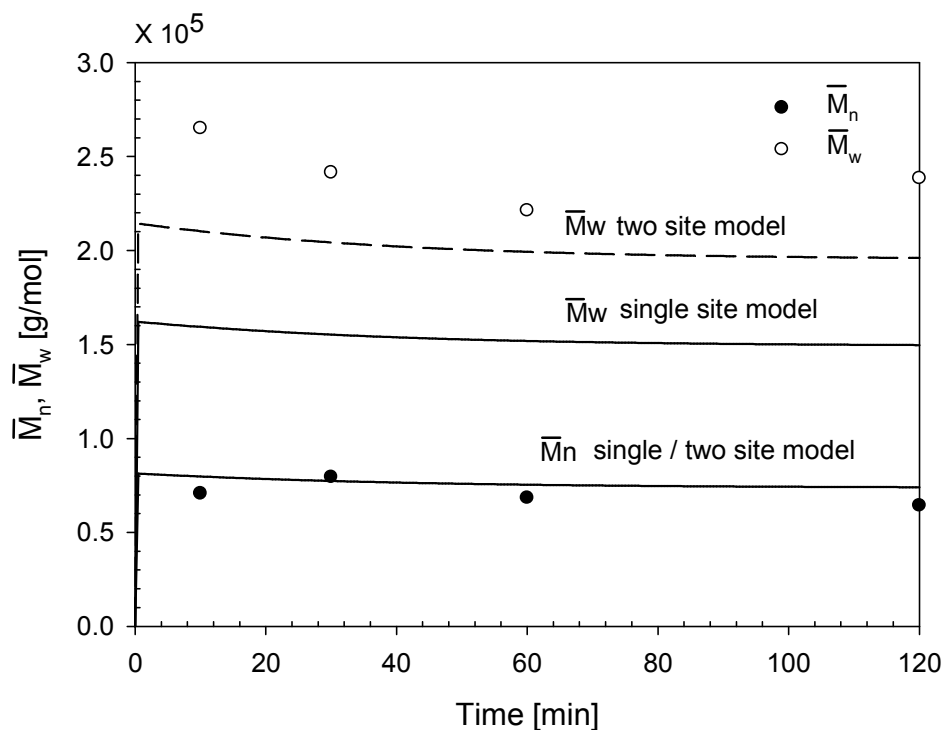


Figure 3.17 sPS molecular weight profiles for $[M]_{b0} = 3.24$ mol/L (symbols - experimental data, lines - model: dashed lines - \bar{M}_w).

To calculate polymer molecular weight averages and molecular weight distribution, several kinetic parameters need to be estimated. They are the chain propagation rate constant (k_p), the monomer chain transfer rate constant (k_{tm}), and the β -hydrogen elimination rate constant ($k_{t\beta}$). To obtain the initial estimates of these rate constants, we first assume that the catalyst is a single site catalyst and catalyst deactivation has little effect on the polymer molecular weight properties. Then, the instantaneous number average degree of polymerization can be represented by the following equation [12, 46]:

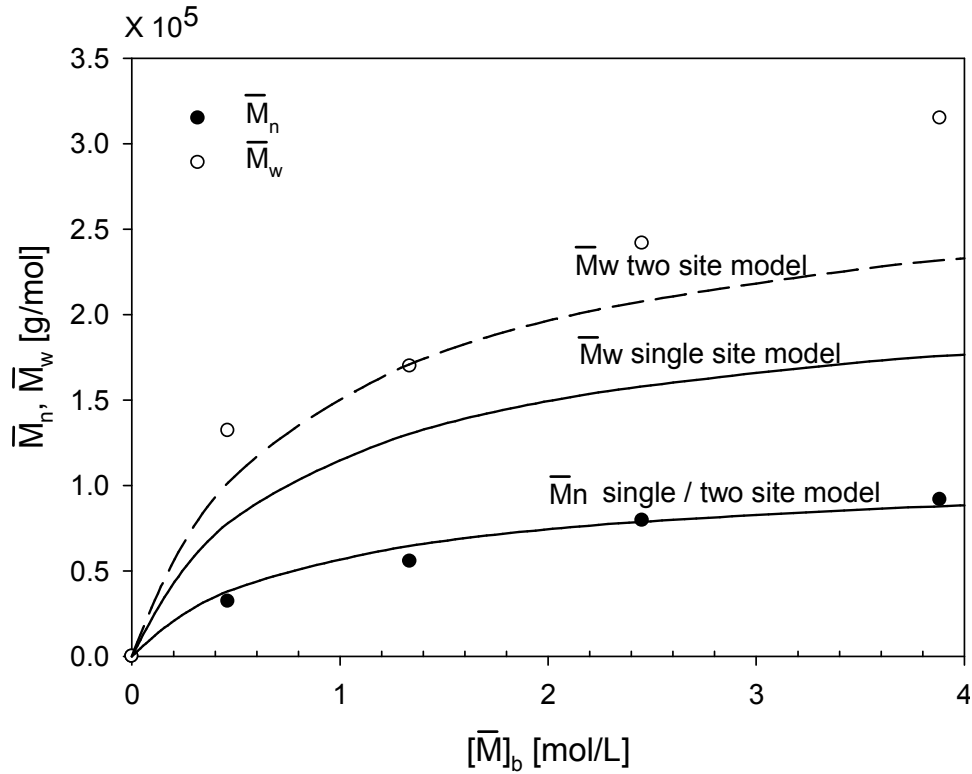


Figure 3.18 Polymer molecular weights at different monomer concentrations (reaction time = 30 min; symbols - data, lines - model).

$$\bar{X}_n = \frac{R_p}{R_t + R_d} = \frac{k_p[M]_s[P]}{k_{tM}[M]_s[P] + k_{t\beta}[P] + k_d[P]} \quad (3-35)$$

where R_p is the chain propagation rate, R_t is the total chain transfer rates, and R_d is the site deactivation rate. Eq. (3-35) can be rearranged to

$$\frac{1}{\bar{X}_n} = \frac{k_{tM}}{k_p} + \frac{k_{t\beta} + k_d}{k_p} \frac{1}{[M]_s} = \frac{k_{tM}'}{k_p'} + \frac{K_2(k_{t\beta} + k_d)}{k_p'} + \frac{k_{t\beta} + k_d}{k_p'} \frac{1}{[M]_b} \quad (3-36)$$

where $k_{tM}' \equiv k_{tM}K_1$. It should be pointed out that the molecular weight averages measured experimentally are cumulative molecular weight values at specific

sampling times. In sPS polymerization and also in most of α -olefin polymerizations with transition metal catalysts, polymer molecular weight (\bar{M}_n) increases almost instantly to a large value with a very slow decrease with time (e.g. Figure 3.17). So, using eqs. (3-35) and (3-36), we assume that the \bar{X}_n values are approximately equal to the cumulative \bar{X}_n values. Indeed, this approximation has been used in the kinetic analysis of polymer molecular weight distribution in most of the non-living addition polymerization processes (e.g., free radical and coordination polymerization) [75, 76].

Eq. (3-36) indicates that by plotting $1/\bar{X}_n$ against $1/[M]_b$, we can estimate the rate constant values. Figure 3.19 shows the test of eq. (3-36). Although we used a single site catalyst model, Figure 3.19 shows that the linear fit is quite satisfactory. Table 3.5 shows the rate parameter values obtained from Figure 3.19. Recall that the effective propagation rate constant (k_p') and the monomer partition constant (K_2) were determined from the polymerization rate analysis. The estimated chain transfer rate constants also indicate that both monomer chain transfer and β -hydrogen elimination reactions strongly affect the polymer molecular weight.

Table 3.5 The reaction rate constants (single site).

k_p'	K_2	k_d	$k_{t\beta}$	k_{tM}'
[L/mol-hr]	[L/mol]	[1/hr]	[1/hr]	[L/mol-hr]
8150	0.47	1.67	7.81	3.11

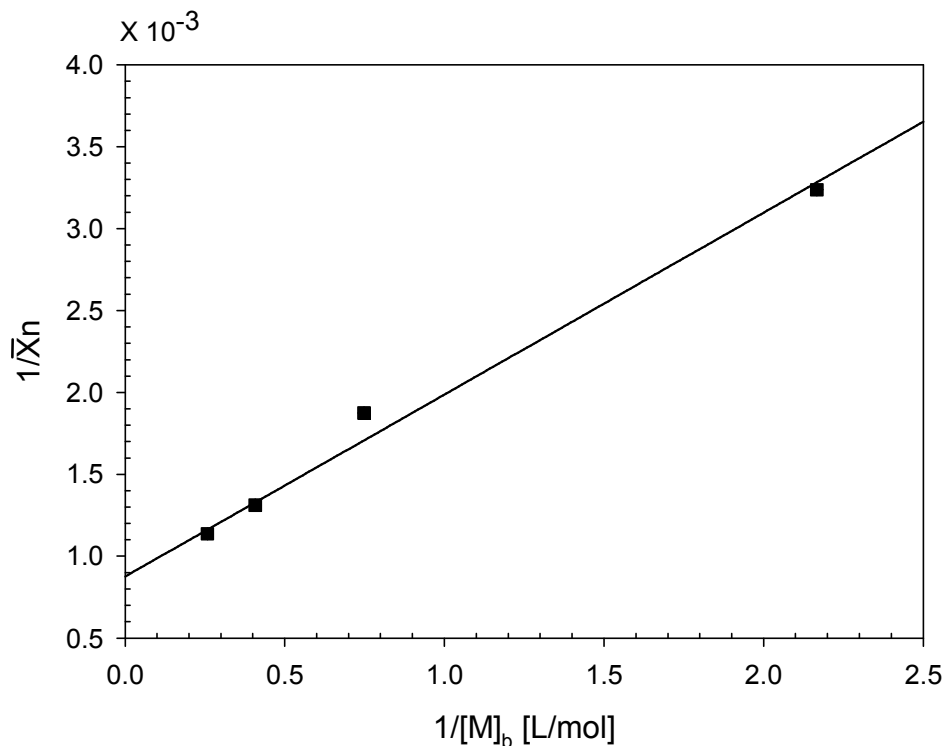


Figure 3.19 Plot of eq. (3-36) to determine rate constants (experimental data at reaction time = 30 min).

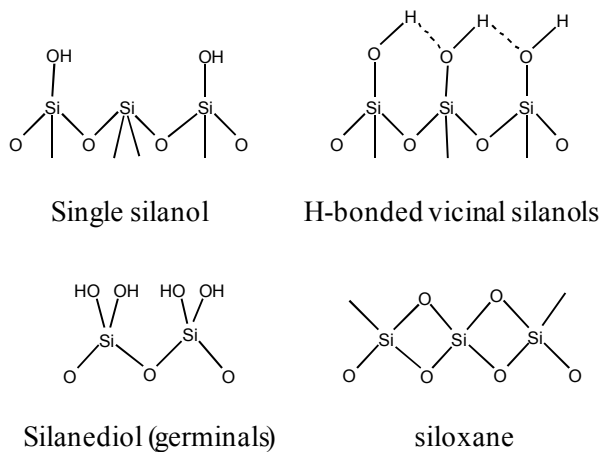
With these kinetic rate constants, we solved the molecular weight moment equations to calculate the weight average molecular weight. The solid lines in Figure 3.17 and 3.18 are the resulting single site model calculations. Here, we observe that the predicted number average molecular weight values are in very good agreement with experimental data but the model calculated weight average molecular weights are lower than the experimentally measured. In a single site model, the polymer chain length distribution follows the Schulz-Flory distribution which gives rise to the predicted polydispersity (\bar{M}_w / \bar{M}_n) of 2.0. As shown in Table 3.1 and Figure 3.17 and

3.18, the sPS polydispersity values are always larger than 2.0, suggesting that catalytic site heterogeneity may exist in the silica-supported catalyst used in our study. It is also possible that metallocene catalyst might have leached out from the solid phase during the polymerization and initiate homogenous polymerization in the bulk liquid phase, contributing to the broadening of MWD [69, 77].

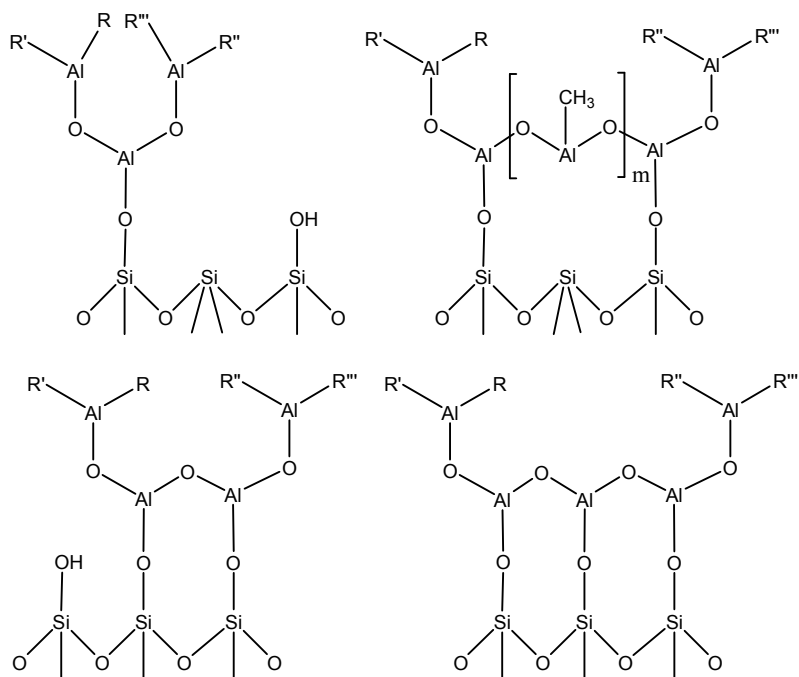
Although many homogeneous metallocene catalysts are known to have a uniform type of catalyst site and hence called as single site catalysts, there are many reports that heterogenized metallocene catalysts often result in broad polymer molecular weight distributions, most notably in α -olefin and styrene polymerizations. For example, Frauenrath *et al.* [78, 79] report that deviations from the single site behavior of metallocene catalysts occur in 1-hexene polymerization with zirconocene/MAO catalyst system. Kou *et al.* [80] propose two active sites model of ethylene polymerization with silica-supported metallocene catalysts. Kou's model is based on the reactivity of several surface functional groups of a silica support and metallocene catalysts. Deviations from single site catalytic behavior of metallocene catalysts have also been observed in the previous sPS polymerization studies (See Schellenberg and Tomotsu's review paper [7]). It is now generally accepted that the broadening of MWD in heterogeneously catalyzed olefin polymerization is caused primarily by the presence of multiple active sites of different catalytic activity and selectivity. Monomer diffusion resistance and catalyst leaching effect can also affect the MWD broadening but their effects may not be as strong as that of catalytic site heterogeneity.

3.3.4 Two-site model

We shall modify the single site model by considering the site heterogeneity in the silica-supported $\text{Cp}^*\text{Ti}(\text{OCH}_3)_3/\text{MAO}$ catalyst as a main cause of MWD broadening. When a metallocene catalyst is supported onto a silica by forming a complex with MAO that is already anchored onto a silica surface, it is likely that the activity of the catalyst will be influenced by the heterogeneity of the silica-MAO complex, causing the site heterogeneity [81]. A silica surface is known to have different types of surface structures represented by single (isolated) silanols, silanediols (geminal), H-bonded vicinal silanols (vicinals), etc [72]. The concentrations of surface hydroxyl groups that may affect the catalyst reactivity are dependent upon the calcination temperature [82]. For example, when a silica gel is calcined at 250-300 °C or above, geminal groups exist only in limited amount, and single silanol and vicinal groups exist almost 50 percent each [83, 84]. Figure 3.20 illustrates the possible surface structures of silica gel and the complexes of MAO and surface groups of the silica. If the main catalyst component is supported onto the surface hydroxyl groups of different structures, it is quite possible that each catalyst site can exhibit different polymerization activity.



Surface structures of silica gel



R, R', R'', R'''.. are $\text{-(AlCH}_3\text{-O)-}_n\text{-Al-(CH}_3\text{)}_2$ or CH_3

Some possible formations between SiO_2 and MAO

Figure 3.20 The surface groups of silica gel and the complexes of MAO and the surface groups of silica [72, 85, 86].

It should be pointed out that although the site heterogeneity of a silica surface may be present, it will be a challenging task to identify the number of different

catalytic site types and their functions as active catalysts. One of the pragmatic methods used by many researchers is the MWD deconvolution technique where experimentally measured broad MWD of heterogeneously polymerized polyolefins is matched with multiple Schulz-Flory distribution curves [87-89]. In this technique, it is assumed that the polymer chain length distribution at each type of catalyst site follows the Schulz-Flory distribution. By adjusting the kinetic constants and the mass fraction of each site, one can match the experimentally observed MWD with the model. In practice, it is difficult to determine the unique set of relevant kinetic parameters for each site.

In our model, we shall employ a two-site model as an approximation of a multisite model to calculate the MWD of sPS. We assume that the catalytic sites have same polymerization activity (propagation activity) but they differ in their chain transfer capabilities. The two-site model is the simplest of the multi-site model and its main advantage is that the number of adjustable parameters is minimal. Certainly if the two-site model fails to fit the experimentally measured polymer molecular weight distribution, more active sites can be added into a model. Of course, then, there is a burden that increased number of parameters needs to be estimated by numerical means (parameter optimization methods). In our analysis, we fix the propagation and deactivation rate constants to minimize the arbitrariness in fitting the MWD.

For a catalyst of multiple active sites, the weight fraction of the polymer of chain length x produced by the active site i ($W_i(x)$) is given by the following Schulz-Flory distribution function: [87-89]

$$W_i(x) = \tau_i^2 x \exp(-\tau_i x) \quad (3-37)$$

where the parameter τ_i is defined as follows:

$$\tau_i = \frac{R_{t,i} + R_{d,i}}{R_{p,i}} \quad (3-38)$$

Then, the weight chain length distribution of sPS is calculated by the following equation

$$X_w = \sum_i \phi_i x W_i(x) \quad (3-39)$$

where ϕ_i is the weight fraction of active site i . With the propagation and deactivation rate constants fixed for each site, τ_i is changed by adjusting the termination rate constants ($k_{t\beta}$, and k_{tM}) and the weight fraction of each active site ϕ_i . The overall termination rate constant determined from Figure 3.17 is also kept constant. Then, only three parameters - $k_{t\beta,1}$, $k_{tM,1}$ and ϕ_1 - are needed to be estimated. Using the non-linear least squares regression technique in MATLAB[®], these three parameters were estimated. $k_{t\beta,2}$, $k_{tM,2}$ and ϕ_2 are calculated as

$$\phi_2 = 1 - \phi_1 \quad (3-40)$$

$$k_{t\beta} = \phi_1 k_{t\beta,1} + \phi_2 k_{t\beta,2} \quad (3-41)$$

$$k_{tM}' = \phi_1 k_{tM,1}' + \phi_2 k_{tM,2}' \quad (3-42)$$

Table 3.6 Two-site model parameters.

$k_{p,1}'$	$k_{p,2}'$	k_d	$k_{t\beta,1}$	$k_{t\beta,2}$	$k_{tM,1}'$	$k_{tM,2}'$	K_2	ϕ_1
[L/mol-hr]	[L/mol-hr]	[1/hr]	[1/hr]	[1/hr]	[L/mol-hr]	[L/mol-hr]	[L/mol]	[-]
8150	8150	1.67	10.98	3.94	5.10	0.68	0.47	0.55

The kinetic parameters for the two-site model were estimated using the experimentally measured MWD data shown in Figure 3.21 and Figure 3.22 and Table 3.6 shows the parameter values determined using the optimal parameter estimation technique. Figure 3.21 shows the comparison of experimental MWD data (symbols) and the two-site model predictions (long dashed lines). The two small curves marked by dashed lines are the MWD for each of the two single sites used in the two-site model. Also shown in Figure 3.21 is the MWD curve by the single site model (solid line). Notice that the single site model is inadequate in predicting the MWD whereas the two site model yields a significantly improved prediction of MWD. With the model parameter values shown in Table 3.6, we also calculated the MWD for other polymerization experiments with different initial monomer concentrations. The model predictions and the experimental MWD curves are shown in Figure 3.22. Some discrepancies between the data and model predictions are clearly present but the two-site model provides a reasonable quality prediction of MWD for each case without additional adjustment of parameter values. Certainly, the model fidelity can be improved by adding third active site into the model but as mentioned earlier, it will be very difficult to find unique set of parameters without uncertainty unless additional data of site characteristics are available.

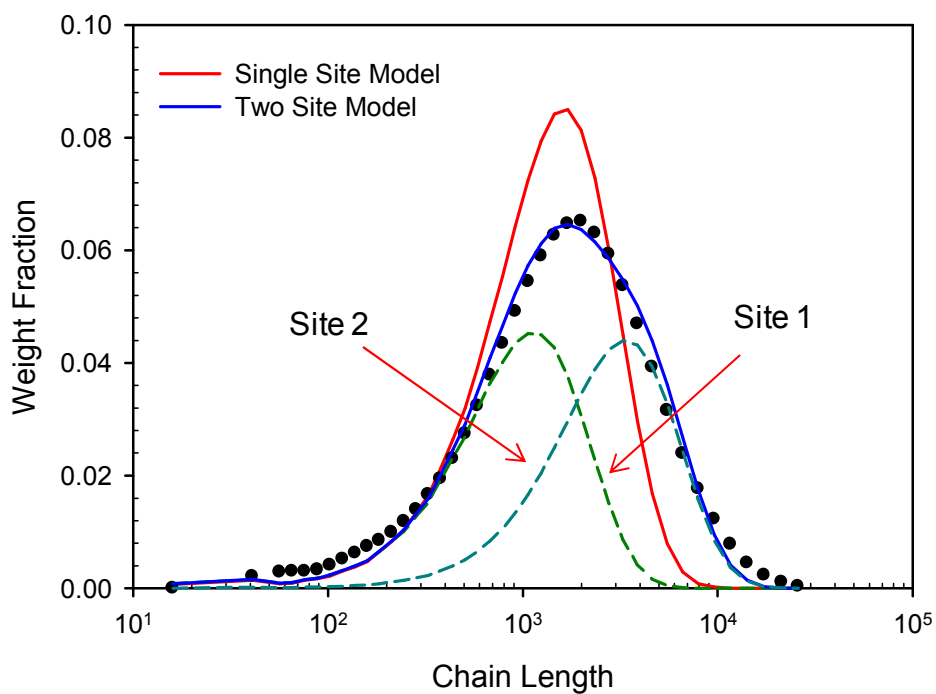


Figure 3.21 Experimental and model-predicted molecular weight distribution curves for $[M]_{b0} = 3.24 \text{ mol/L}$, $t = 30 \text{ min}$, symbols - data).

Finally, we would like to remark on the underpredicted polymerization rates at $t = 120 \text{ min}$ shown earlier in Figure 3.6 (c) (lines). Recall that the polymerization rate was predicted using the single site model. In our two-site modeling, we assumed that the two different sites are represented by the same propagation rate constant (k_p') and the deactivation rate constant (k_d). Therefore, both the single site model and the two-site model yield the same polymerization rate. However, it is certainly possible that each site can also have different propagation and deactivation rate constants, making one of the two sites to deactivate faster than the other, affecting the overall polymerization rate. Practically, however, it will be very difficult, if not impossible, to discern the differences in the polymerization activities of the two different catalytic

sites when the overall polymerization rate and molecular weight data are the only available process data that can be measured. Let us go back to the polymerization rate data in Figure 3.6 (c): Although the predicted polymerization rates at $t = 120$ min are lower than the experimentally measured, these underpredicted polymerization rates have little effect on the polymer yield as shown in Figure 3.6 (a). It is because the amount of polymer produced after 60 min is very small.

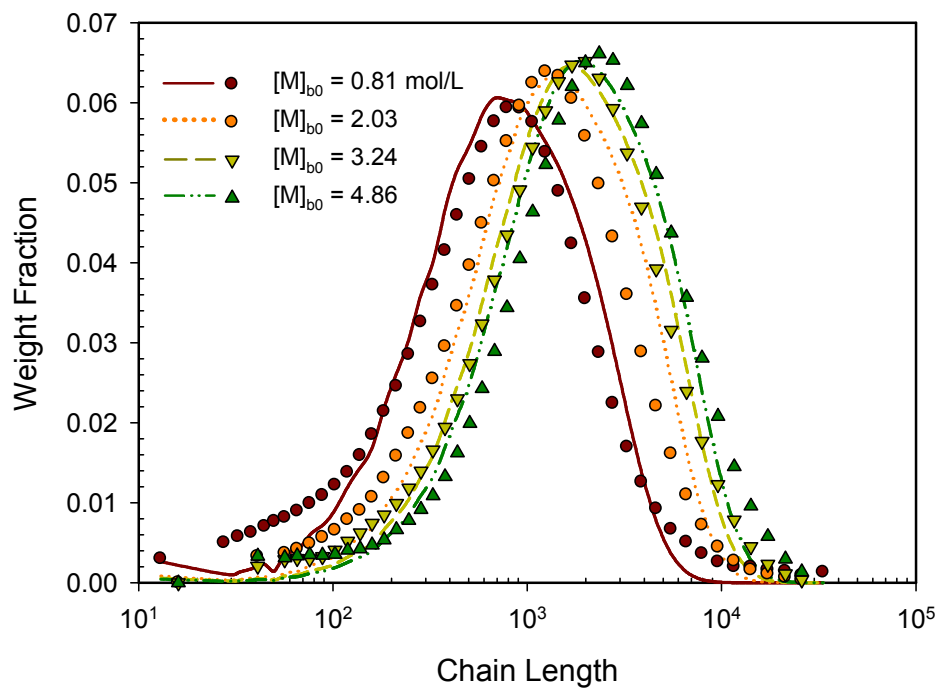


Figure 3.22 Experimental and model-predicted molecular weight distribution curves at different initial monomer concentration ($t = 30$ min, symbols – data).

3.4 Conclusions

In this chapter, new experimental and theoretical modeling analysis of the syndiospecific polymerization of styrene over silica-supported $\text{Cp}^*\text{Ti}(\text{OCH}_3)_3/\text{MAO}$ catalyst has been presented. The use of silica-supported catalyst in a liquid slurry polymerization has been very effective in obtaining non-agglomerated sPS particles. We observed that sPS polymerization rate is nonlinearly dependent on the bulk phase monomer concentration. This is attributed to the partition of monomer between the solid and the liquid phases. We incorporated the monomer partition effect into our kinetic model and obtained a very good fit of the experimental data. The estimated partition parameter values suggest that the monomer concentration in the solid phase is lower than the bulk liquid phase concentration. Another important point in a liquid slurry polymerization of styrene is that an sPS slurry undergoes a series of physical changes during the polymerization.

In general, very narrow MWD is obtained when a homogeneous metallocene catalyst is used. In our experiments with a heterogeneous silica-supported $\text{Cp}^*\text{Ti}(\text{OCH}_3)_3/\text{MAO}$ catalyst, we observed that sPS molecular weight distributions were broad (i.e., $\bar{M}_w / \bar{M}_n > 2.0$), indicating a significant departure from the single site polymerization kinetics. We modeled the MWD distribution broadening by employing a two-site kinetic model. Using the polymerization rate and MWD data, we estimated the relevant model parameters. The two site model provided improved predictions of the molecular weight distribution, clearly suggesting the presence of multiple active sites in the silica-supported metallocene catalyst used in our study.

The use of silica-supported metallocene catalyst was quite effective in preventing the formation of gels in the reactor. We observed that a separate liquid phase can completely disappear at about 15-20 wt.% of solid phase when high monomer concentrations are used. It is because unreacted monomer and diluent are absorbed by the solid polymer phase.

Chapter 4: Nascent Morphology of Syndiotactic Polystyrene in Homogeneous and Heterogeneous Reaction Systems²

4.1 Introduction

The morphological study of polymer is one of important parts of polymer research. For example, the interpretation of polymer particle formation mechanism can give us to better understand the polymerization reaction mechanism. Even though lots of researchers have published papers about the nascent morphology of polyolefins with metallocene catalyst, the nascent morphology of sPS has rarely been investigated.

The morphology of sPS has been recently studied for re-crystallized samples by several groups [39, 40, 90-98]. Ray *et al.* [90] observed fibrillar networks of sPS from sPS film that was prepared by solvent induced crystallization with benzene and toluene using scanning electron microscope (SEM) and atomic force microscope (AFM). They suggest that thin layer sPS film can have fibrillar networks, whereas thick sPS film from the bulk solution cannot form fibrillar networks. It was also supposed that low polymer concentration promoted the formation of sPS fibrillar structures [90]. Guenet *et al.* [40, 93, 96, 97] also made sPS thin membrane with naphthalene and its derivatives such as biphenyl, tetralin, and benzophenone. After sublimation of naphthalene through vacuum extraction, fibrillar networks of sPS were

² The main part of this chapter has been published in Han, J.J., W. J. Yoon, H. W. Lee and K. Y. Choi (2008). "Nascent morphology of syndiotactic polystyrene synthesized silica-supported metallocene catalyst." *Polymer* **49**(19): 4141-4149.

observed [40, 93, 96, 97]. According to their experimental data, polymer lamella structures interconnected by sPS fibrils (average diameter: 20 ~ 50 nm) are formed below 0.10 g/g of polymer fraction of sPS gel, but only fibrillar networks of sPS are observed at above 0.20 g/g of sPS fraction [40]. When *trans*-decalin was used, only spherulite morphology was observed, whereas fibrillar morphology was observed when naphthalene and tetralin were used. They proposed that helix stabilization by benzene rings on the main chain might play an important role to form fibrillar structures [93, 96]. *Trans*-decalin has weak interaction with benzene rings on the sPS backbone because *trans*-decalin is totally protonated naphthalene derivative [93]. It has been suggested by Itagaki *et al.* [39] that the fibrous and network morphology of sPS is induced by the mobile solvent molecules that disturb the isotropic growth of polymer crystals into a three-dimensional structure. Daniel *et al.* [91, 94] made sPS aerogels by dissolving sPS with several solvents such as chloroform, tetrahydrofuran, and trichloroethane and drying them with supercritical CO₂. They observe sPS fibrils having 20 – 110 nm of diameter. They address that the correlation length of sPS crystalline planes increases with the strength of sPS main chain-solvent molecule interactions [91]. The solvents used for crystallization and the morphology in the literature are summarized in Table 4.1.

Solvent induced crystallization is a good method to make micro porous (between fibrillar structures of sPS) and nano porous (cavities of δ form of sPS) membranes [40, 93, 96, 97]. Fibrillar networks are micro porous structures, and they can be used in many applications. For example, emptied δ -form that can be made by removing solvent molecules in the cavities of δ -form should be applied to water

purification [99] and methanol purification [32]. Daniel *et al.* shows the availability of sPS aerogels that can be applied to insulations and catalysis [91]. The availability of δ -form of sPS as an optical chemosensor by means of nanoporous cavities has been studied by Giordano groups [100-102]. They successfully detected chloroform and toluene by using thin δ -form of sPS film. The possibility of using sPS δ -form as a gas storage was also investigated [103].

Table 4.1 Solvents used for crystallization and the morphology of sPS films

Solvent	Morphology	Reference
Benzene	Fibrillar structure	[90]
Toluene	Fibrillar structure	[90]
Naphthalene	Fibrillar structure	[40, 92, 95, 96]
Tetralin	Fibrillar structure	[93]
Biphenyl	Fibrillar structure	[96]
benzophenone	Fibrillar structure	[96]
Chloroform	Fibrillar structure	[39, 91, 94]
tetrahydrofuran	Fibrillar structure	[94]
1,2-dichloroethane	Fibrillar structure	[94]
trichloroethane	Fibrillar structure	[94]
trans-decalin	Spherulite	[93]
diphenylmethane	Spherulite	[96]

Although there are many reports on the crystallization of sPS from a dilute solution, little has been reported on the morphology of sPS during the polymerization with homogeneous and heterogeneous metallocene catalysts. In the study of styrene

polymerization kinetics with heterogenized metallocene catalyst [51, 52, 68], the morphology of sPS is quite different from that of α -olefin polymers (e.g., polyethylene and polypropylene) produced by heterogeneous Ziegler-Natta or solid-supported metallocene catalysts. With embedded $\text{Cp}^*\text{Ti}(\text{OCH}_3)_3/\text{MAO}$ catalyst, film or fiber shaped polymer fractions are observed in SEM photographs [52]. Since nascent sPS is a semi-crystalline polymer with δ -form, there should be morphological similarities between solvent-induced sPS crystals and nascent sPS. Understanding the morphological development such as catalyst fragmentation a catalyst/polymer particle undergoes is also important issues for the design of high activity catalyst and for the control of polymer properties. In this chapter, the morphologies of sPS synthesized over homogeneous and silica-supported metallocene catalyst in a liquid slurry polymerization process are discussed.

4.2 Experimental

sPS polymerizations in homogeneous and silica-supported catalyst systems were carried out and the experimental conditions were summarized in Table 4.2. The morphology of the polymer was investigated by scanning electron microscopy (SEM) using Hitachi S-4700 and SU-70. The sPS samples were coated with AuPd layer of thickness 5 nm in a Denton DV-503 vacuum evaporator coating apparatus (Denton Ltd.). The polymer crystallinity and melting points were measured by differential scanning calorimetry (DSC) with a heating rate of 20 °C/min under nitrogen gas flow using Q100 System (TA Instruments). EDAX (Ametek) attached to AMRAY-1610

was used for energy dispersive X-ray spectroscopy (EDX/EDS) analysis of sPS. X-ray diffraction (XRD) patterns were obtained by D4 ENDEAVOR diffractometer (Bruker AXS Inc.) with Cu K α as a radiation source in the range of 5 ~ 30° of 2 θ . Thermogravimetric analysis (TGA) was performed in the temperature range of 30 ~ 550 °C at a heating rate of 10°C/min under nitrogen atmosphere (nitrogen flow rate: 100 mL/min) using 2050 TGA system (TA Instruments).

Table 4.2 Experimental sPS polymerization data

Catalyst type	Styrene/solvent (v/v ratio)	[M] ₀ [mol/L]	[Ti] × 10 ⁴ [mol/L]	Reaction time (min)	Conv. (%)
Homogeneous	2.5/7.5	2.14	1.60	10	13.03
	4/6	3.49	1.60	10	7.86
			0.68	30	9.75
	6/4	5.24	1.60	10	6.17
			0.26	60	9.34
	8/2	6.98	1.60	10	3.24
Silica-supported	1/9	0.81	2.62	10	26.5
			2.62	60	49.4
	2.5/7.5	2.02	2.62	10	22.6
			2.62	60	43.7
	6/4	4.71 ²⁾	3.95	2	4.04
		4.86	2.62	10	9.5
			2.62	60	31.0
	4/6 ¹⁾	3.24	1.73	30	6.95

* Solvent: n-heptane, T = 70°C, [Al]/[Ti] = 500 (mol/mol)

1) 6 nm pore sized silica

2) No agitation

4.3 Results and Discussion

4.3.1 Particle morphology

Prior to the morphological study of nascent sPS particle, solvent induced crystallization experiment was carried out for observing the morphology of solvent induced crystalline sPS. sPS synthesized over homogeneous catalyst was used for re-crystallization and chloroform was used to re-crystallize sPS sample. Table 4.3 lists the polymerization and re-crystallization conditions. In Figure 4.1, the SEM photographs of solvent induced crystalline sPS film are shown. Figure 4.1 shows that re-crystalline sPS has fibrillar morphology. Note that the average diameter of fibrils is about 30 – 50 nm.

Table 4.3 Polymerization and re-crystallization conditions for making crystalline sPS film

Polymerization condition		Recrystallization condition	
[M] ₀	5.14 mol/L	Solvent	chloroform
Solvent	<i>n</i> -heptane	Concentration	1.9 wt. %
[Ti]	2.56x10 ⁻⁵ mol/L	Temperature	80°C
[Al]/[Ti]	1000 mol/mol	Dissolving time	120 min
Reaction temperature	70°C	Crystallization at room temperature	
Reaction time	60 min	Dry <i>in vacuo</i>	
Catalyst type	homogeneous		

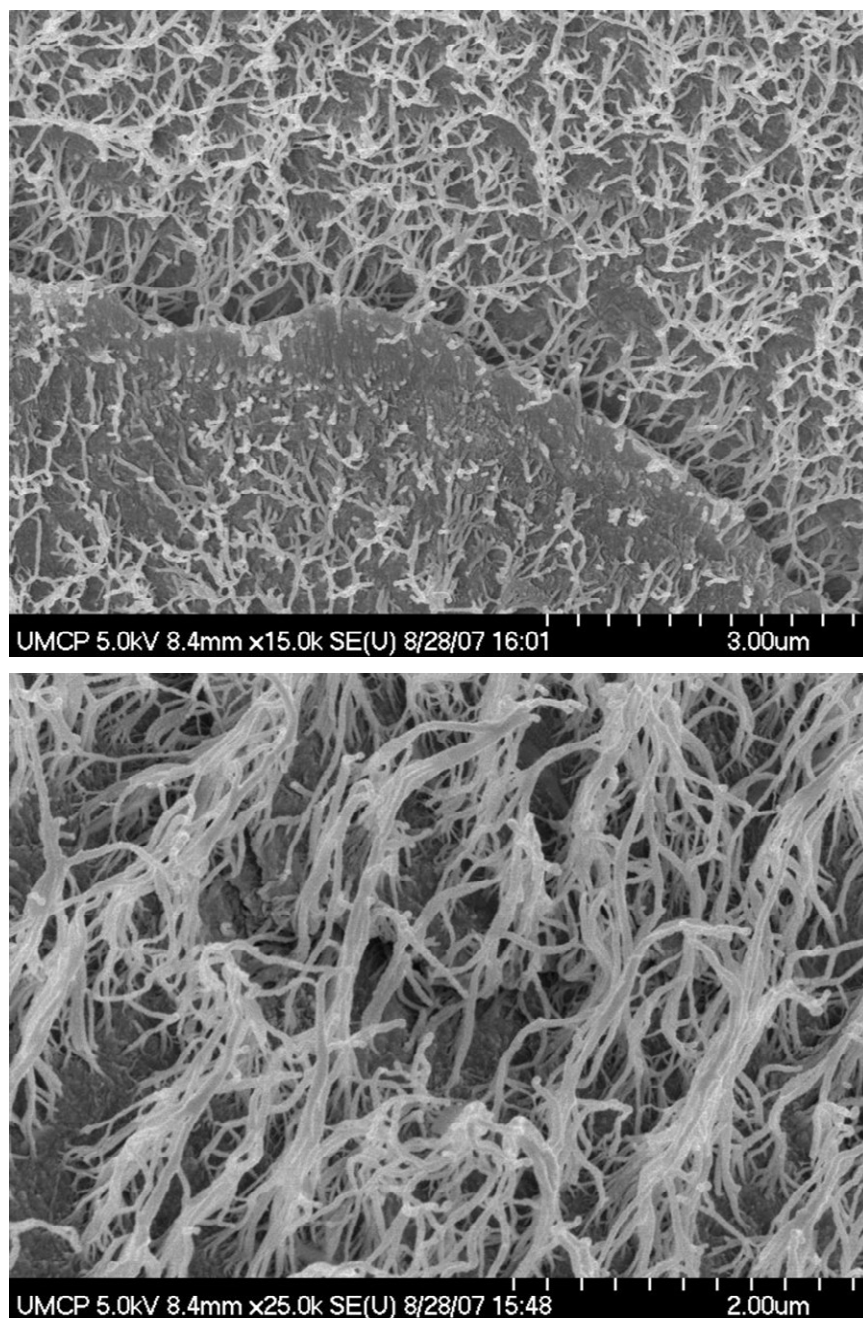


Figure 4.1 SEM images of sPS film produced by solvent induced crystallization:
solvent: chloroform.

Figure 4.2 shows the SEM images of sPS produced over homogeneous (unsupported) catalyst. During the liquid slurry polymerization with homogeneous catalyst, sPS particles are deformed by shear and collision with other particles in the reactor. Hence, the shapes and sizes of sPS particles become irregular as shown in Figure 4.2 (a). The surface of sPS particle is smooth in most regions (Figure 4.2 (b)). However, fibrillar forms are also observed at the some edges (Figure 4.2 (c)) or on the flat surface (Figure 4.2 (d) and (e)) of the particle. Figure 4.2 (f) shows the fibrillar structures in the region where sPS particles are split into two pieces. This implies that interior morphology of an sPS particle might be different from the exterior morphology of particle. In general, the outer surface of polymer particles can be deformed during polymerization process by colliding with other particles. Fibrillar forms can be fused together when the polymer particles are dried after polymerization, making the sPS outer surface of sPS particles smooth. Thus, observation of the interior morphology of an sPS particle is needed to understand the sPS gel physical structure.

Figure 4.3 illustrates the SEM images of the sPS particle produced over homogenous metallocene catalyst. Before SEM analysis, sPS particle was mechanically fractured. Figure 4.3(b) and (d) show the close-up view of the cross-section of the fractured polymer particle. The particle interior is densely packed with polymer nanofibrils of quite uniform diameter (ca. 30-50 nm). The dimension of these nanofibrils is the same as that observed at the particle surface (Figure 4.2) and polymer film obtained by solvent induced crystallization (Figure 4.1).

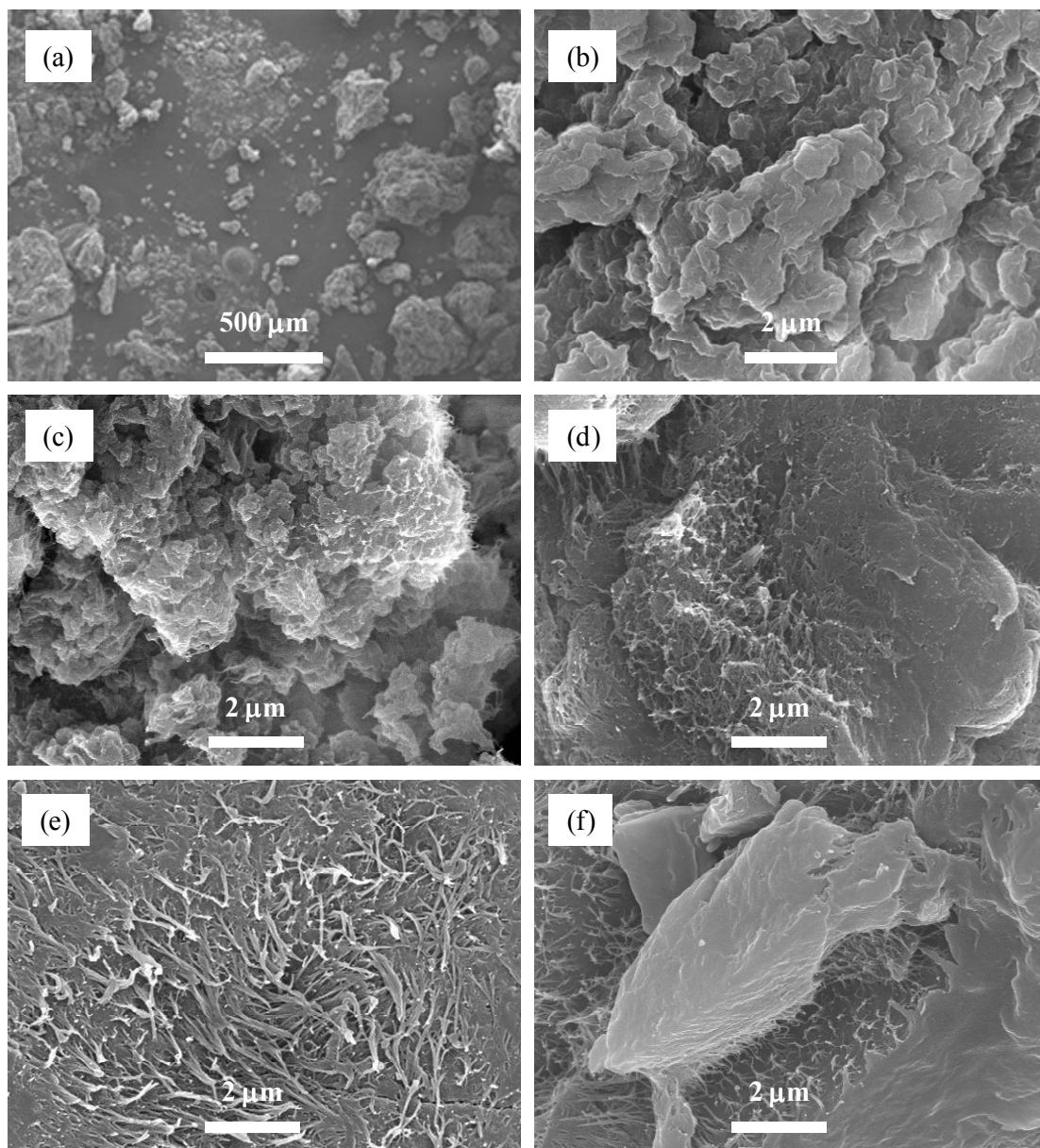


Figure 4.2 SEM images of sPS produced over homogeneous catalyst: (a) and (b)

$[M]_0 = 3.49$ mol/L, reaction time = 10 min, (c) $[M]_0 = 3.49$ mol/L, reaction time = 30 min, (d) $[M]_0 = 5.24$ mol/L, reaction time = 10 min, (e) $[M]_0 = 2.14$ mol/L, reaction time = 10 min, (f) $[M]_0 = 6.98$ mol/L, reaction time = 10 min.

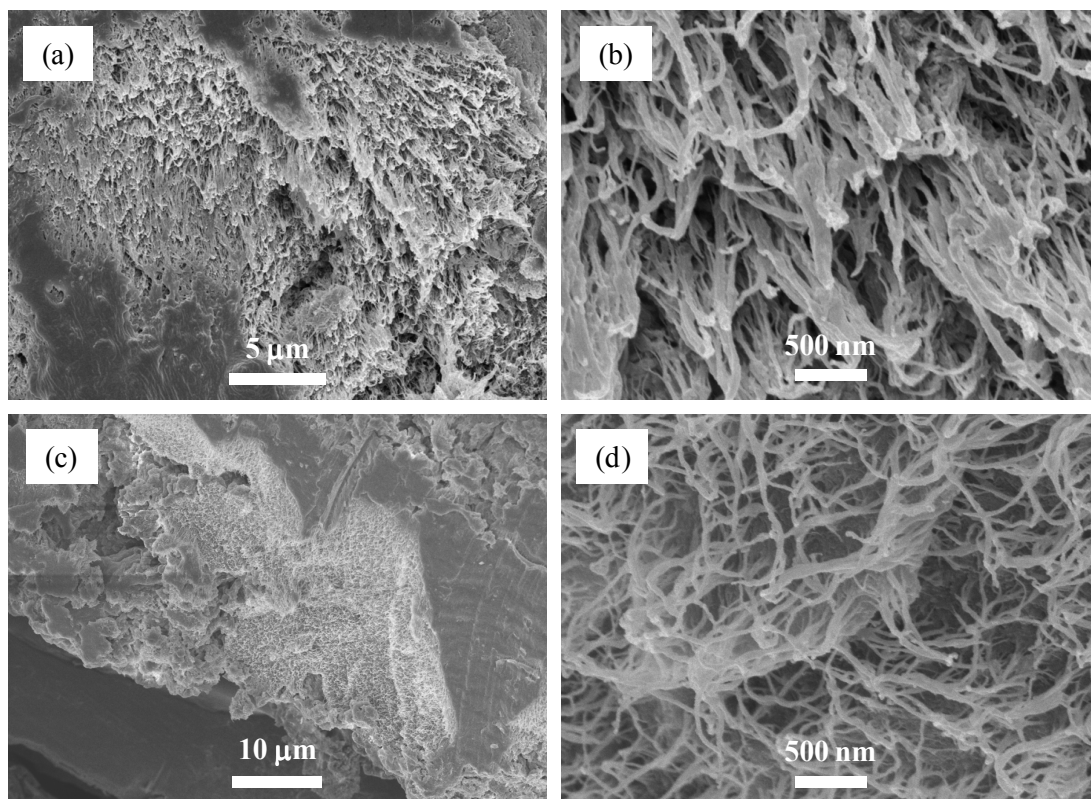


Figure 4.3 SEM images of sPS particle cross-sections: homogenous catalyst system, (a) and (b) $[M]_0 = 3.49 \text{ mol/L}$, $T = 70^\circ\text{C}$, reaction time = 10 min, (c) and (d) $[M]_0 = 5.24 \text{ mol/L}$, $T = 70^\circ\text{C}$, reaction time = 60 min.

Similar observations were made for the sPS particles synthesized with silica-supported metallocene catalyst. In the first series of experiments, agitation was not applied. To observe the nascent morphology of sPS at its early stage, a polymer sample was taken 2 min after polymerization at the initial styrene concentration of 4.71 mol/L . Since the catalyst activity is very high, the monomer conversion reached 4.0% at 2 min, which corresponds to the total solid content (TSC) of 2.67%. When the sample was taken, the polymerization mixture was a turbid slurry of polymer

particles. Figure 4.4(a) illustrates a large 100-120 μm sPS particle sample. The exterior surface of the particle is very rough. The close-up images of the polymer particle surface shown in Figure 4.4(b) and 4.4(c) reveal that the sPS particle surface is covered with heavily entangled long nanofibrils of 30-50 nm in diameter. Unlike the surface morphology of the sPS particles with agitation over homogeneous catalyst system, the SEM images of the surface of sPS particles without agitation in silica-supported catalyst system shows the fibrillar structures on the particle surface. Although it is difficult to measure the exact lengths of the nanofibrils from the SEM images, these nanofibrils appear to be quite long and rigid. Figure 4.4(d) shows the polymer sample taken at 10 min of reaction time. The surface morphology of the particle is same as seen in Figures 4.4(a), 4.4(b) and 4.4(c).

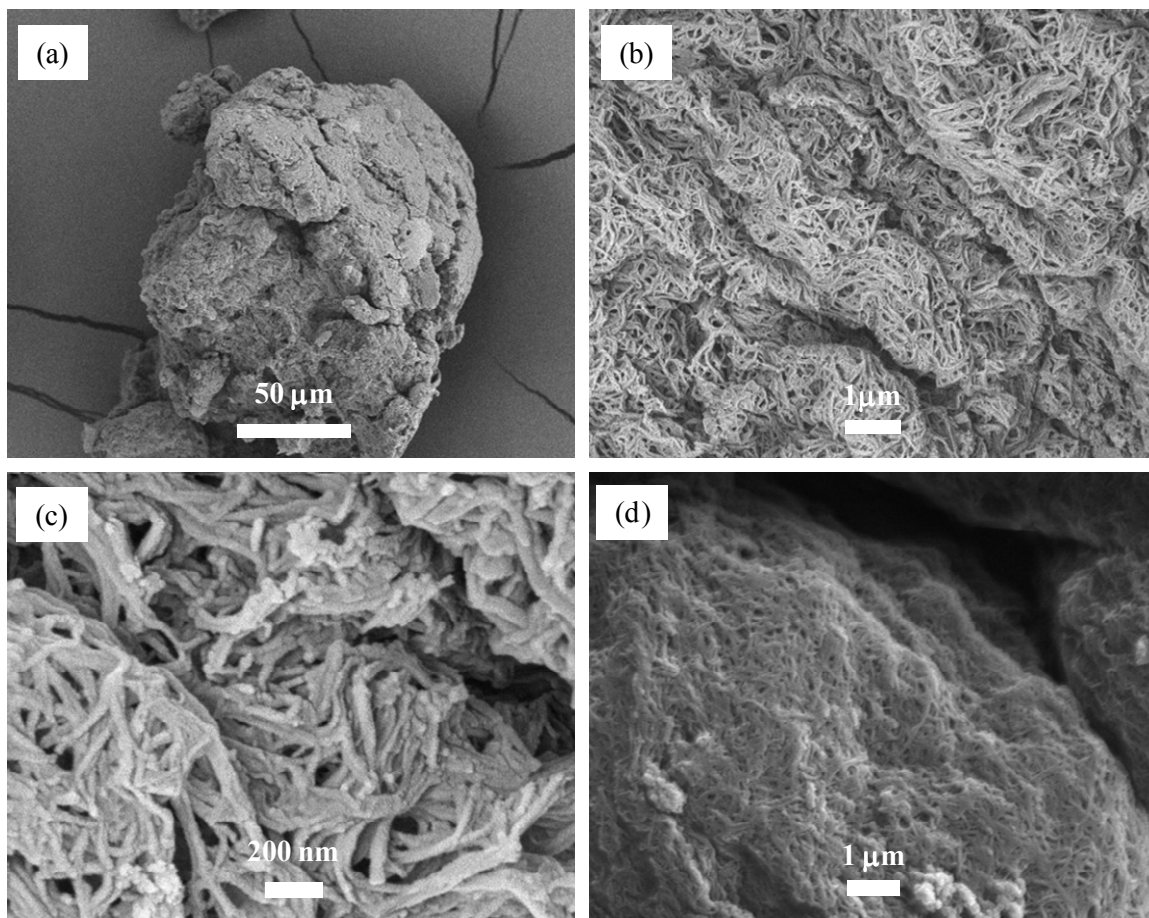


Figure 4.4 SEM images of sPS particle produced over silica-supported $\text{Cp}^*\text{Ti}(\text{OCH}_3)_3/\text{MAO}$ catalyst in *n*-heptane: pore size of silica gel = 20nm; (a)-(c), $[\text{M}]_0 = 4.71 \text{ mol/L}$, reaction time = 2 min; (d), $[\text{M}]_0 = 4.86 \text{ mol/L}$, reaction time = 10 min.

The fibrillar morphology of sPS shown in Figure 4.4 is very different from the granular particle morphology commonly observed in polyolefins synthesized over heterogeneous Ziegler-Natta catalysts or silica-supported catalysts [104-107]. In silica-supported metallocene catalyzed polyolefin processes, the fragmentation of catalyst supports lead to the exposure of active catalytic sites to monomers for high

activity and the fragmented catalyst particles grow to larger polymer particles. There are still some aspects of morphological changes of polyolefin particles that are not fully understood in heterogeneous α -olefin polymerization processes. However, it is generally agreed that the growth of polyolefin particles over high activity heterogeneous catalysts follows the multigrain model paradigm [108, 109]. For example, ca. 30-50 μ m size high activity catalyst particles disintegrate shortly after they are exposed to monomers. The catalyst fragments are loosely connected by polymers and these grow to a macroparticle of size of several hundred microns. Hence, the macroparticle is a large congregate of microparticles. Such morphological development has been confirmed by numerous electron microscopic analysis studies [105, 110-112].

To observe the interior structure of a polymer particle, we mechanically fractured an sPS particle sample taken at 10 min of reaction (Figure 4.5(a)). Figure 4.5(b) shows the close-up view of the cross-section of the fractured polymer particle. The most prominent feature of the polymer morphology revealed in Figure 4.5(b) is that the particle interior is densely packed with polymer nanofibrils of quite uniform diameter (ca. 30-50 nm). The dimension of these nanofibrils is the same as that observed at the particle surface (Figure 4.4). Since the polymer particle is packed with thin and long nanofibrils, the particle interior seems to have a large fraction of void space.

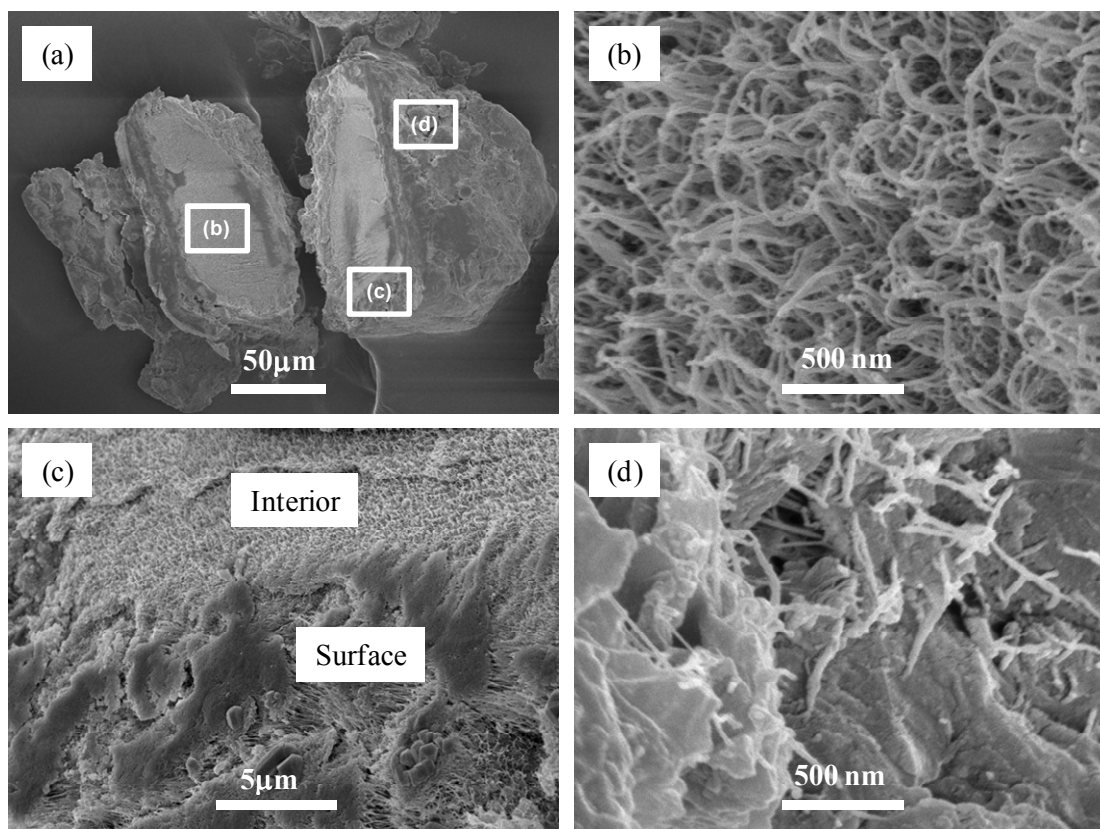


Figure 4.5 SEM images of sPS particle cross-sections: pore size of silica gel = 20nm, $[M]_0 = 4.86$ mol/L, $T = 70^\circ\text{C}$, reaction time = 10 min; (a) fractured sPS particle, (b) particle interior, (c) edge portion of the sPS particle, (d) close-up of the particle surface.

In Chapter 3, we showed that one gram of nascent sPS particles polymerized over the same silica-supported catalyst can absorb more than 6 mL of solvent (*n*-heptane) (Table 3.4). The interior morphology of the sPS particle shown in Figure 4.5(b) and 4.3 (b) and (d) suggest that the nanofibrillar growth is probably responsible

for such a high solvent absorbability of sPS particles. It is also interesting that the nanofibrils inside the particle are not entangled but rather straight and separated from each other. The interior morphology of the sPS particle synthesized over silica-supported catalyst is similar as that of the sPS particle synthesized over homogeneous catalyst (Figure 4.3). Figure 4.5(c) shows the edge portion of the fractured particle surface and Figure 4.5(d) is the close-up view of the particle surface. It is seen in both Figure 4.5(c) and Figure 4.5(d) that the nanofibrils grow out from the particle interior and they collapse and fuse at the particle surface as they are exposed to the bulk liquid phase during the polymerization. The shear force exerted by agitation in the reactor might have also promoted the adhesion of sPS nanofibrils at the surface, making them look like a fused layer.

To investigate the effect of the pore size of silica gel on the dimension of sPS nanofibrils, polymerization experiments were carried out with the same catalyst supported on the silica gel with smaller pore diameter (Davisil™ 633, average pore size: 6nm). Figure 4.6 shows the interior morphology of a polymer particle. Again, we can see that the particle interior is densely packed with nanofibrils of 30-50 nm-diameter, which is very similar to that observed with Davison 952 catalyst support having much larger average pore diameter (20 nm). Figure 4.6(b) shows that some polymer fibrils are as thin as about 10-15 nm and some nanofibrils aggregate to larger-diameter bundles. The results shown in Figures 4.4-4.6 indicate that the silica pore size has no effect on the diameter of sPS nanofibrils. These phenomena also observed in Figure 4.2 – 4.3 (homogeneous catalyst system). In other words, the sPS nanofibrils are the intrinsic morphology of the polymer.

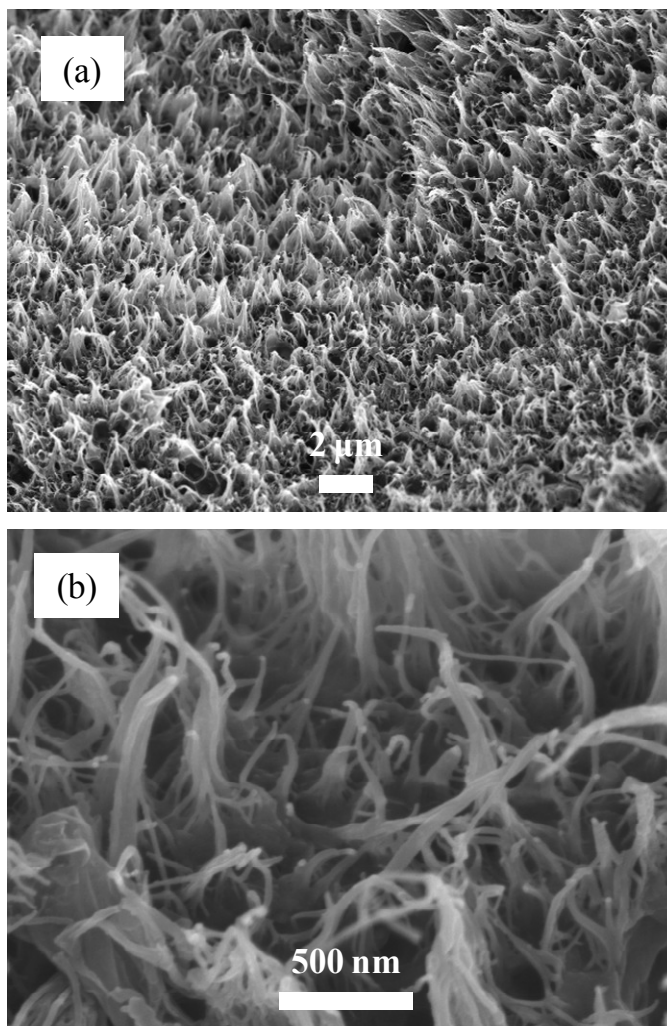


Figure 4.6 SEM images of sPS produced over silica-supported $\text{Cp}^*\text{Ti}(\text{OCH}_3)_3/\text{MAO}$ catalyst having smaller pore size: pore size of silica gel = 6nm, $[\text{M}]_0 = 3.24 \text{ mol/L}$, reaction time = 30 min.

4.3.2 Crystalline structure of sPS

sPS has four main polymorphs (i.e., α , β , γ , δ forms) that differ with respect to the chain conformation and the chain packing within the unit cell [23]. The α and β

forms have the sPS chains in the trans-planar, zigzag conformation, while the γ and δ forms have a 2_1 -helix conformation. When a thin layer of sPS melt is slowly cooled to room temperature, the polymer crystallizes in lamellar or spherulite morphology to a mixture of α and β forms of crystals [113-116]. However, when sPS is crystallized by solvent-induced crystallization, δ -form crystal is obtained. In a typical crystallization experiment, a homogeneous solution of sPS dissolved in a solvent at high temperatures is cooled to lower temperatures, leading to the formation of thermoreversible gels of fibrillar network structure or paste-like systems with spherulites [90]. The solvent does not bind with the sPS chains but acts as a solvating agent to cause the formation and stabilization of helical chains.

The formation of δ -form crystal or co-crystal is also related to the formation of nanofibrils because the sPS chain rigidity increases with a strong interaction between polymer chain (host) and solvent molecules (guest), leading to an increased correlation length [94]. δ -form sPS crystal is nanoporous with its cavity volume to be about 120 \AA^3 and has a density (0.977 g/cm^3) lower than amorphous sPS (1.04 g/cm^3) [33, 117]. Figure 4.7 shows a single δ -form sPS chain of a 2_1 -helix conformation with 1,000 styrene units ($\text{MW} = 104,000$) constructed by using Materials Visualizer (Accelrys Software Inc.). The diameter of the polymer chain is 1.1 nm. Using the unit cell dimension of a δ -form sPS crystal ($a = 17.47 \text{ \AA}$, $b = 13.42 \text{ \AA}$) [36], we can calculate that about 350 sPS polymer chains are needed to constitute the diameter of a single sPS fibril of 30 nm observed by SEM. Since the length of sPS nanofibrils observed in the previous SEM images is quite larger than the length of a single sPS chain (e.g., 180 nm for $\text{MW} = 104,000$, $1.8 \text{ }\mu\text{m}$ for $\text{MW} = 1,040,000$), we can say that

the observed sPS nanofibrils are the aggregates of a large number of polymer chains grown from the active catalyst sites in the direction of fibrillar growth. The nanoporous δ -form sPS can rapidly absorb certain organic compounds and form the clathrates. With the clathration, the unit cell of the δ -form is enlarged and the cavity can include molecules larger than its original size [118, 119].

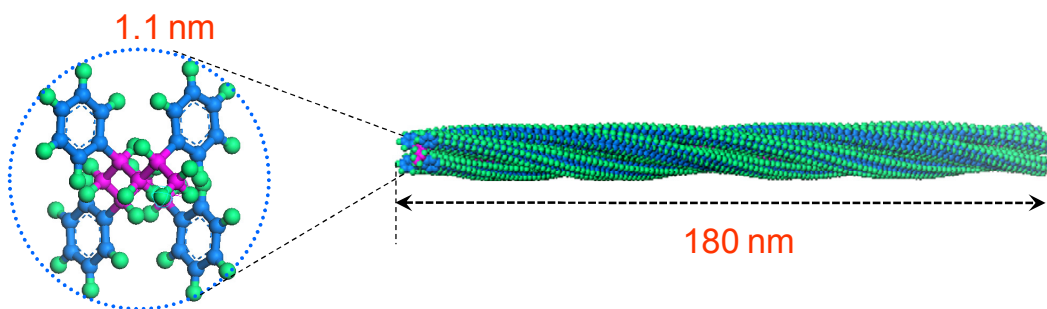


Figure 4.7 2_1 -helix of a single sPS chain with 1000 styrene units: drawing based on Materials Studio[®] modeling package (Accelrys Software Inc.).

The crystalline properties of sPS particles were investigated using differential scanning calorimetry (DSC), thermogravimetric analysis (TGA), and X-ray diffraction (XRD). Degree of crystallinity and melting temperature of sPS measured by DSC are listed in Table 4.4. The degree of crystallinity of sPS polymer is calculated as:

$$\% \text{ of crystallinity} = \frac{\Delta H_m - \Delta H_c}{\Delta H_m^0} \times 100 \quad (4-1)$$

where ΔH_m , ΔH_c , and ΔH_m^0 are heat of melting, heat of crystallization and heat of melting of 100% crystalline polymer (= 53.2 J/g) [120].

Table 4.4 Degree of crystallinity and melting temperature of sPS produced over silica-supported catalyst.

$[M]_0$ (mol/L)	Reaction Time (min)	Reaction Temp. (°C)	Crystallinity (%)	T_m (°C)
0.81	10	70	24.2%	270.7
	30	70	40.0%	270.1
	60	70	40.0%	270.1
2.03	10	70	26.9%	269.7
	30	70	40.6%	269.8
	60	70	43.5%	269.5
	120	70	42.4%	269.9
4.86	10	70	29.8%	270.2
	30	70	34.2%	269.3
	60	70	40.0%	269.7

The measured melting temperatures of sPS particles are ca. 270°C. At 10 min of reaction time, the degree of crystallinity of sPS is about 24 ~ 30 wt. %, and the degree of crystallinity of sPS increase with reaction time. After 60 min, all samples have over 40 wt% of degree of crystallinity. At 60 min of reaction time, different initial monomer concentration might not affect sPS crystal structures and the degree of crystallinity. As initial monomer concentration increases, the degree of crystallinity

of sPS at 10 min also increases. The degree of crystallinity of most solvent induced crystalline sPS crystals are about 40 % [118, 121-124].

Figure 4.8(a) shows the DSC thermograms of the sPS produced over homogeneous catalyst and Figure 4.8(b) shows the DSC thermograms of the sPS synthesized over silica-supported catalyst. There are two melting endotherms in the first scan of both samples. The broad first melting endotherm (A and A') corresponds to the transformation of the δ -form crystals to the γ form crystals [23]. As discussed in Chapter 1, the δ -form crystals have guest molecules in the structure and γ form crystals have not. Thus, in temperature range of the first melting endotherm, the guest molecules are removed from the sPS particles. The boiling temperature of styrene (145°C) is higher than that of *n*-heptane (98.4°C). The peak position of the first melting endotherm in Figure 4.8(a) is higher than that of the first melting endotherm in Figure 4.8(b) because the styrene concentration of sPS over homogeneous catalyst is higher than that of sPS over silica-supported catalyst. The melting endotherm at about 270°C corresponds to the melting of the α form crystals of sPS [23]. The second scan shows the glass transition point at 100°C (B and B'). Since the solvent in the sPS samples have been removed during the first scan, no melting endotherm is observed at 100-170°C in the second scan thermogram.

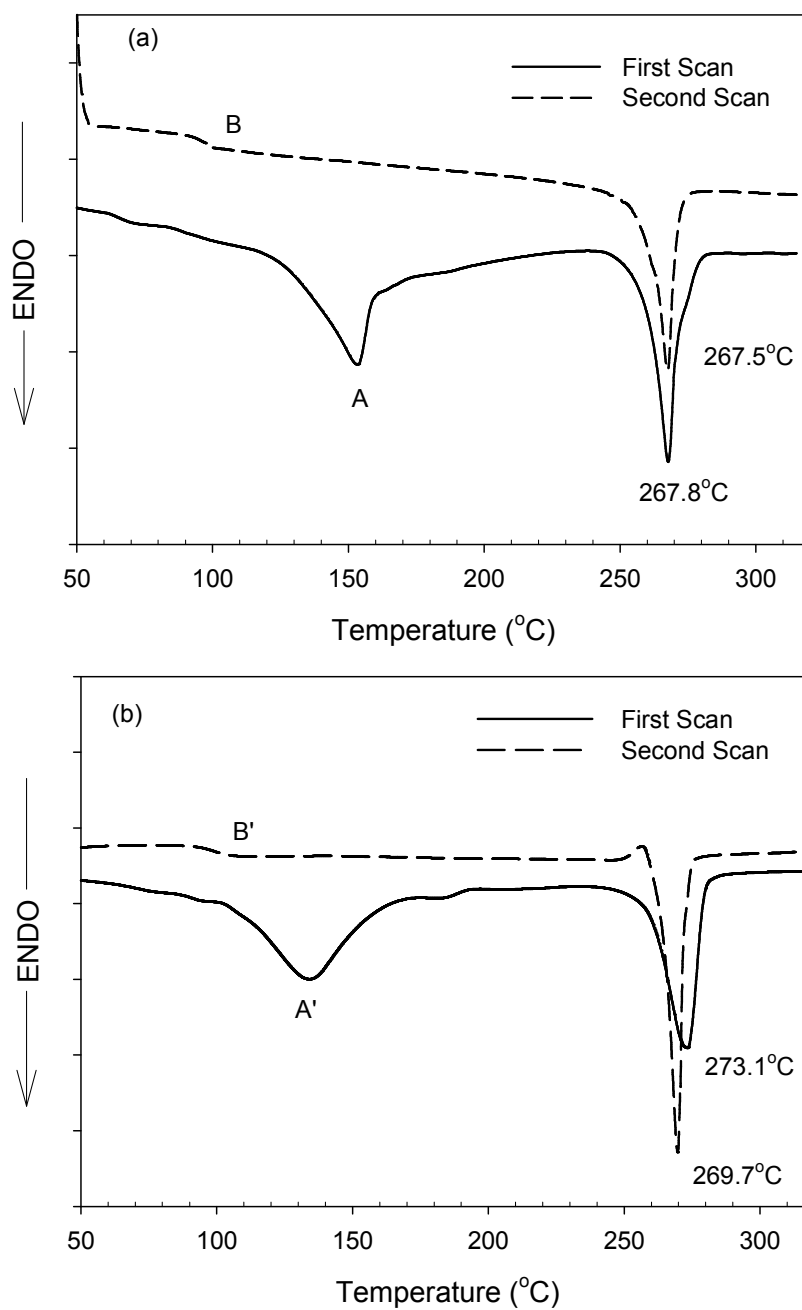


Figure 4.8 DSC thermograms of the sPS; (a) homogeneous $\text{Cp}^*\text{Ti}(\text{OCH}_3)_3/\text{MMAO}$ catalyst, $[\text{M}]_0 = 8.73 \text{ mol/L}$, reaction time = 30 min, (b) silica-supported $\text{Cp}^*\text{Ti}(\text{OCH}_3)_3/\text{MAO}$ catalyst: pore size of silica gel = 20nm, $[\text{M}]_0 = 4.86 \text{ mol/L}$, reaction time = 60 min.

The XRD patterns of sPS particles are shown in Figure 4.9 for the homogeneous catalyst and silica-supported catalyst systems. Before the X-ray diffraction analysis, the nascent sPS samples were dried *in vacuo* overnight at ambient temperature. All these XRD patterns show that these polymers are of the co-crystals or filled δ -form crystals of sPS clathrated with the residual monomer styrene or *n*-heptane (diluent) as characterized by the peaks at $2\theta \approx 8$, and 10.5° [30, 33, 125].

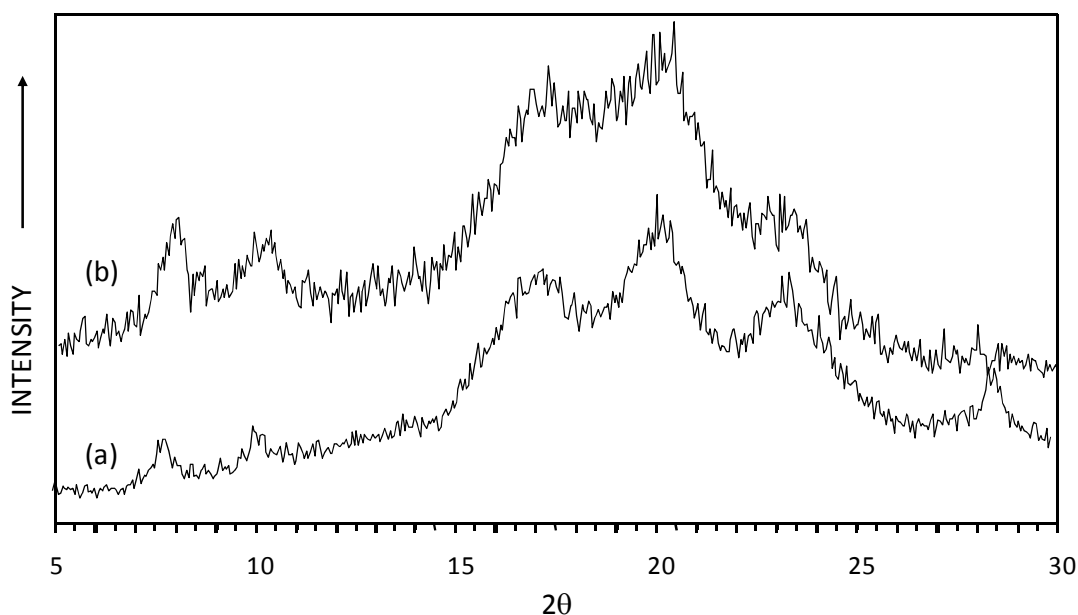


Figure 4.9 XRD patterns of sPS particles (a) homogeneous $\text{Cp}^*\text{Ti}(\text{OCH}_3)_3/\text{MMAO}$ catalyst, $[\text{M}]_0 = 8.73 \text{ mol/L}$, reaction time = 60 min, (b) silica-supported $\text{Cp}^*\text{Ti}(\text{OCH}_3)_3/\text{MAO}$ catalyst: pore size of silica gel = 20nm, $[\text{M}]_0 = 2.03 \text{ mol/L}$, reaction time = 60 min.

The thermogravimetric analysis (TGA) of sPS particles produced over silica-supported metallocene catalyst shown in Figure 4.10 indicates 5-8 % weight loss of the sPS samples at 80-120 °C, confirming the presence of low molecular weight guest molecules co-crystallized with sPS. The DSC and XRD data show that the crystalline structure of the sPS particles polymerized over homogeneous and silica-supported Cp*Ti(OCH₃)₃/MAO catalysts is very similar to those of the thin sPS films crystallized by solvent induced crystallization technique as reported in the literature [39, 40, 90-98].

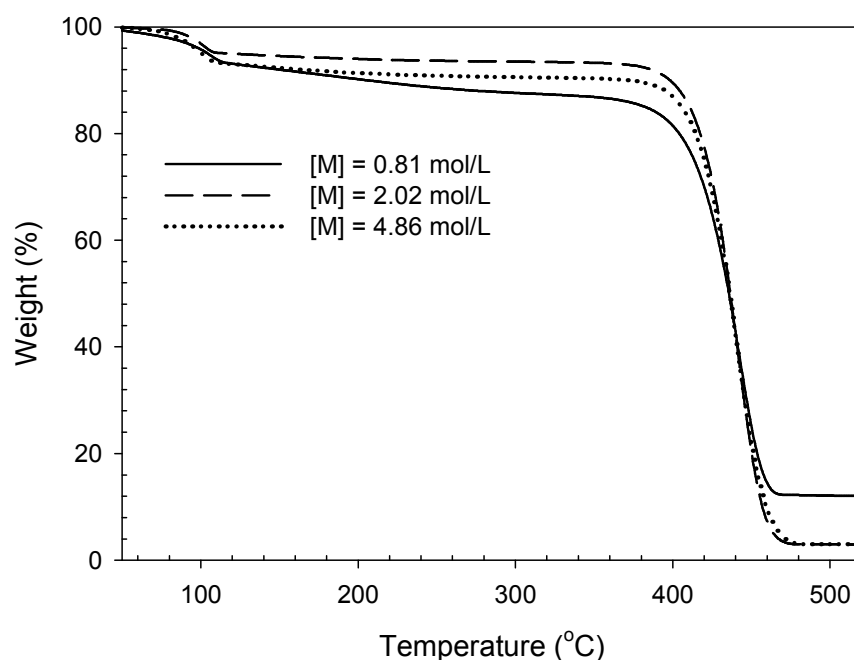


Figure 4.10 TGA thermograms of nascent sPS samples synthesized over silica-supported Cp*Ti(OCH₃)₃/MAO catalyst in *n*-heptane: pore size of silica gel = 20nm, reaction time = 60 min.

4.3.3 Macroscopic growth of sPS particles synthesized over silica-supported metallocene catalyst

Different from homogeneous catalyst system, sPS particles grows during the slurry phase polymerization of styrene over silica-supported catalyst. Figure 4.11(a) and Figure 4.11(b) show the SEM micrographs of Davison 952 silica gel particles (average pore size of 20 nm) and the polymerized sPS particles produced after 60 min in silica-supported catalyst system, respectively. We can see that the size of the original catalyst-supported silica gel particles is about 30-100 μm and the sPS particles have grown to about 100-300 μm -diameter. It is also interesting to observe that the fully grown sPS particles seem to have replicated the shapes of the original silica particles. Although the particle interior morphology of sPS is quite different from that of polyolefins (e.g., globular), Figure 4.11 suggests that the 'shape replication' phenomena commonly observed in heterogeneous α -olefin polymerization processes also occur in sPS polymerization with silica-supported catalysts. The uniform dispersion of catalyst in the original catalyst and the uniform growth of sPS nanofibrils in a polymer particle with silica fragmentation are believed to be the reason for such shape replication phenomena. Note that the shape and size of sPS particles over homogeneous catalysts are irregular.

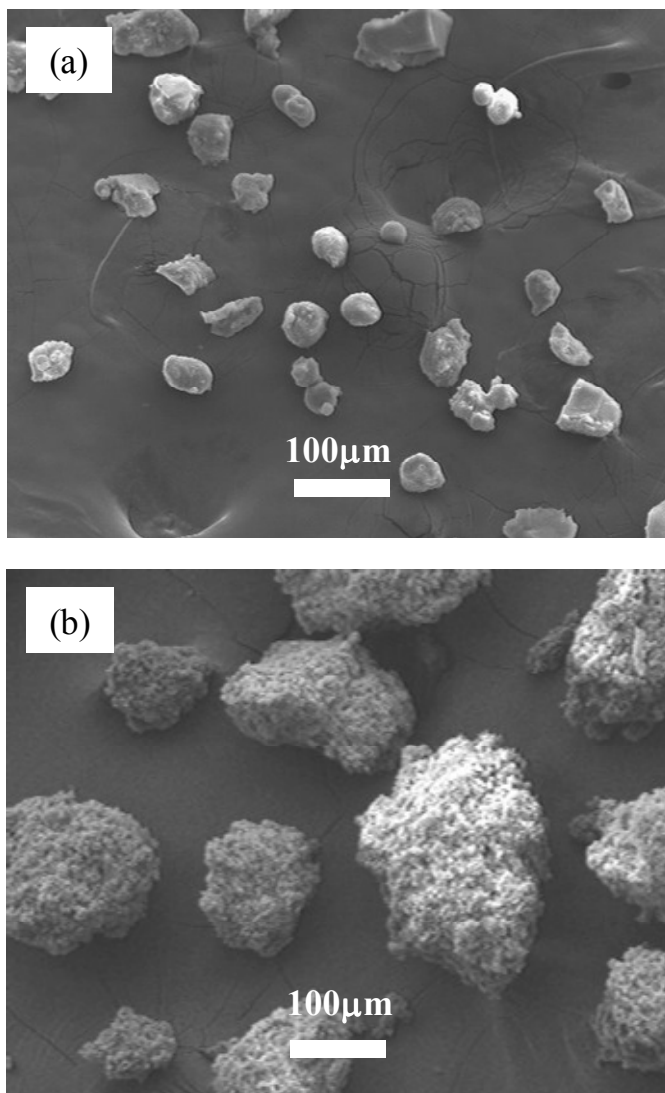


Figure 4.11 SEM images of silica gel and sPS particles: (a) Davison 952 silica gel, (b) polymerized sPS particles, $[M]_0 = 2.02$ mol/L, reaction time = 60 min.

Before we consider the sPS particle growth mechanism during the polymerization, let us briefly review the particle growth phenomena observed in ethylene or propylene polymerization over silica-supported chromium oxide or metallocene catalysts. The silica particle fragmentation and the development of

polymer particle morphology in olefin polymerization are most succinctly described by Fink and coworkers [110, 126]: Initially, a thin polymer shell is formed on the silica particle surface. The polymer shell creates a diffusion barrier for monomer. As polymerization continues, the buildup of hydraulic forces in the particle pore increases, leading to the fragmentation of the silica support from the particle surface to the interior. New active centers are exposed by the fragmentation for increased rate of polymerization. The ultimate catalyst fragment size is about 20-100 nm, which is also an agglomerate of smaller primary silica particles of about 5-10 nm. Each fragmented particle is encapsulated in polymer and tied to its neighbor through polymer entanglements [127].

Figure 4.12 shows several SEM images of the sPS particle interior. In Figure 4.12(a), we can see a silica particle fragment of about 5-6 μm -diameter embedded in a densely populated sea of sPS nanofibrils. In some edge portion of the unfragmented silica particle, sPS nanofibrils are attached to the silica surface, suggesting that sPS chains grow at the catalytic sites anchored onto a silica surface. The lack of sPS nanofibrils on the silica particle surface in Figure 4.12(a) might have been caused by the absence of catalyst or no particle fragmentation.

Figure 4.12(b) shows the unfragmented silica particles at a different location in the polymer particle sample. Notice that the exposed silica top surface has no polymer fibrils whereas the bottom part of the silica clearly shows the sPS nanofibrils growing from the surface of the silica where active catalyst sites are expected to be present. Figure 4.12(c) shows an interesting cross-sectional view of another polymer particle. There is a large cavity in the center which is believed to be left by a silica

particle removed during the sample fracture. Around the large cavity, we can also see many smaller cavities (circular shape) that might have also been left by smaller silica particles removed during the sample fracture.

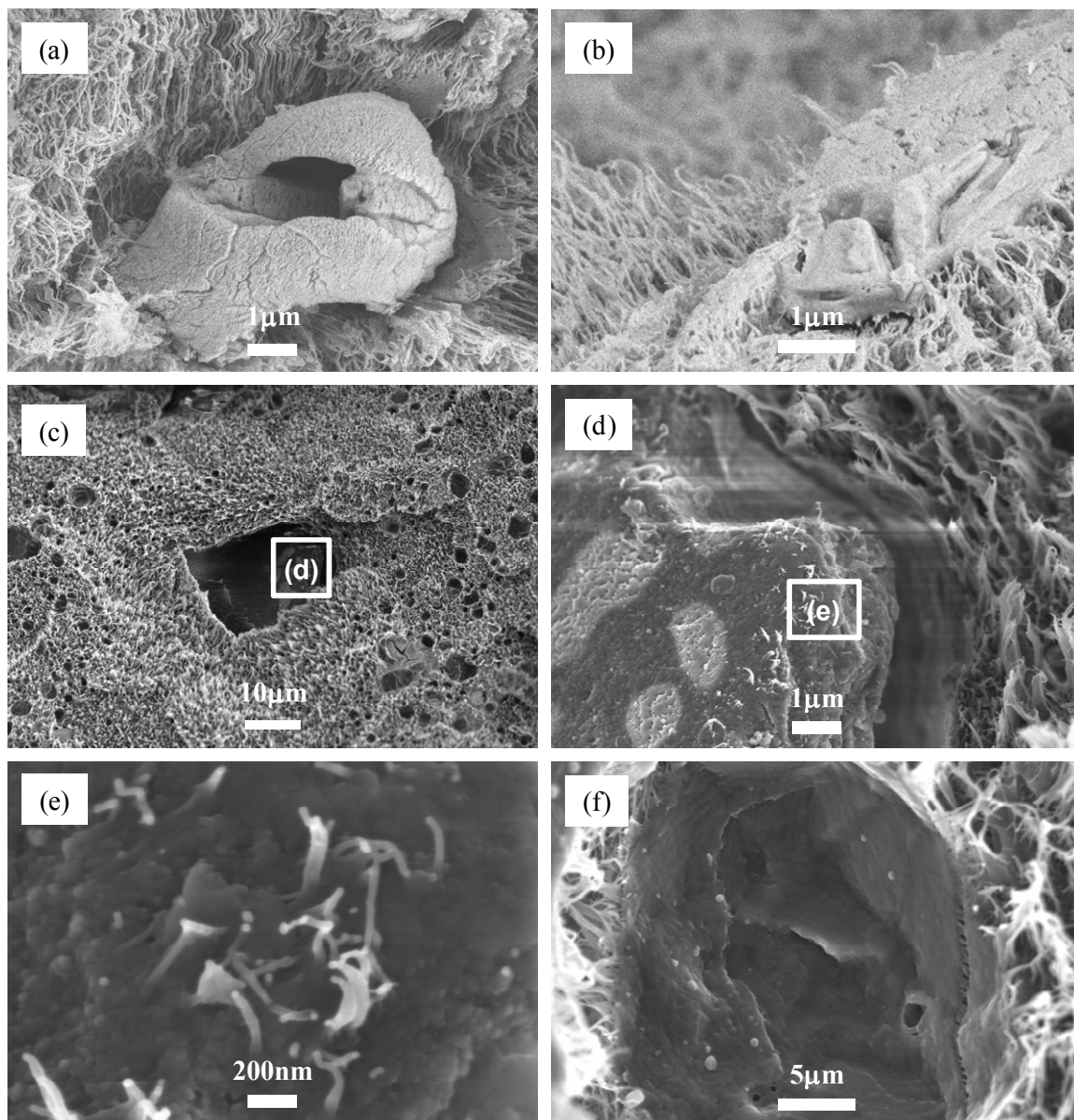


Figure 4.12 SEM images of fractured sPS particles: (a)-(b), pore size of silica gel = 20nm, $[M]_0 = 4.71$ mol/L, reaction time = 2 min; (c)-(f), pore size of silica gel = 6nm, $[M]_0 = 3.24$ mol/L, reaction time = 30 min.

Figure 4.12(d) is the close-up image of the large cavity in Figure 4.12(c). We can see that another silica particle is embedded underneath surrounded by sPS nanofibrils. It is also seen that the silica particle surface has several lighter regions where few polymer fibrils are visible. If we carefully observe the surface texture of the 'bare' silica particle in Figure 4.12(d), we can see the original silica micrograins as observed in Figure 3.1(a) in Chapter 3. No reaction might have occurred in these bare regions. Interestingly, a similar SEM image was reported for a silica-supported chromium oxide catalyst for gas phase ethylene polymerization [71]. Figure 4.12(e) is a close-up view of the edge portion of the embedded silica particle in Figure 4.12(d). It shows that sPS nanofibrils formed inside the void between the silica aggregates are extruding out or sPS nanofibrils are growing from the silica surface. Figure 4.12(f) is a close-up image of another empty cavity left by a large silica particle fragment. It appears that some part of the original silica fragment is still present because the sPS nanofibrils growing from the particle surface are holding the particle.

We also analyzed the polymer particle by EDX analysis to examine how the fragmented silica particles are distributed in an sPS particle. Figure 4.13(a) shows the SEM image of a cut surface of a sPS particle and Figure 4.13(b) and 4.13(c) show the silicon and aluminum mapping. It is seen that both silicon and aluminum are quite homogeneously dispersed in the polymer, suggesting that the fragmentation of MAO-activated silica-supported metallocene catalyst have occurred with the particle expansion.

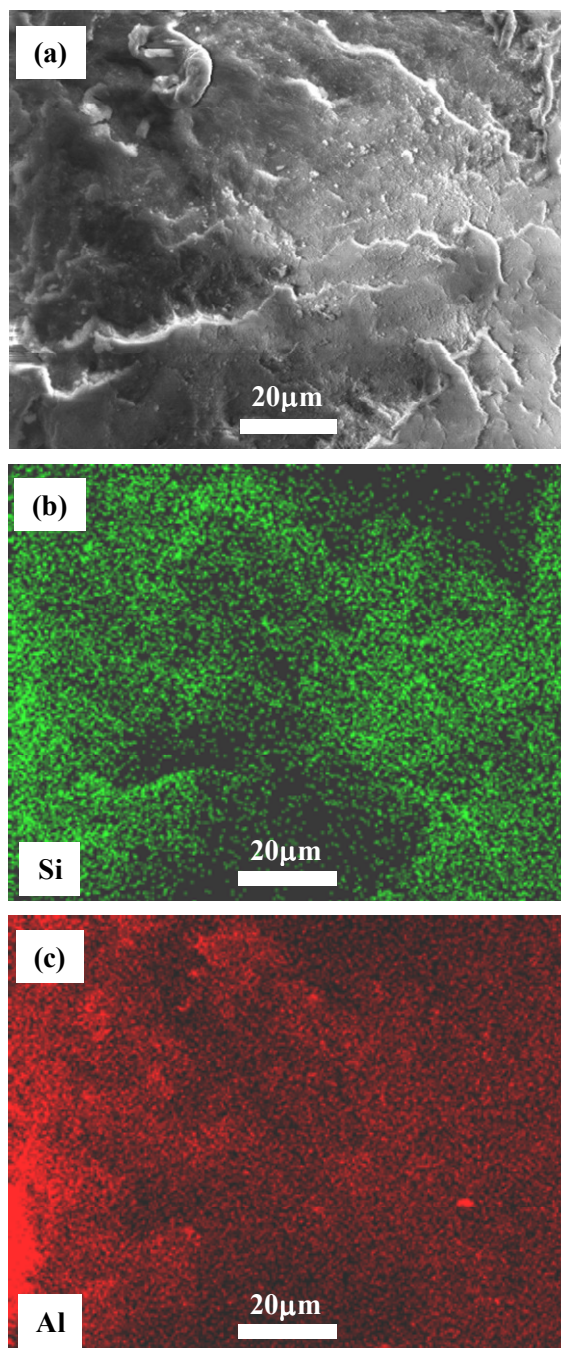


Figure 4.13 Element distribution mappings of a fractured sPS particle produced over silica-supported $\text{Cp}^*\text{Ti}(\text{OCH}_3)_3/\text{MAO}$ catalyst: pore size of silica gel = 20nm, $[\text{M}]_0 = 4.86 \text{ mol/L}$, Reaction time = 10 min: (a), SEM image; (b) Si mapping; (c) Al mapping.

4.3.4 Particle growth mechanism in silica-supported catalyst system

The turnover frequency (TOF) is defined as the number of molecules of monomer that convert to polymer chain per catalytic site per unit time. The TOF can be calculated from polymerization rate as follows:

$$\text{TOF} = \frac{R_p}{[C^*]_t} \quad (4-2)$$

where, R_p is the polymerization rate (mol-St/L.sec), $[C^*]_t$ is the total active site concentration (mol-Ti/L) and the unit of TOF is molecules-St/molecules-Ti.sec (or 1/sec). From the experimental catalyst activity data shown in Table 4.2, we can estimate the TOF of the silica-supported catalyst. Table 4.5 lists the TOF of silica-supported catalyst for different monomer concentrations at 10 min of reaction time.

Table 4.5 Turnover frequency of silica-supported catalyst

$[M]_0$ (mol/L)	St. Vol. % (%)	Reaction Time (min)	Avg. Activity $\times 10^{-3}$ (g-sPS/mol-Ti.min)	TOF (1/sec)
0.81	10	10	8.58	1.37
2.02	25	10	18.22	2.92
3.24	40	10	20.65	3.30
4.86	60	10	18.40	2.94

If we assume that all the titanium sites are active, the TOF value is about 1-3 styrene molecules per Ti site per second. If a comparison is made with MgCl_2 -

supported TiCl_x catalysts for propylene polymerization, the TOF for propylene polymerization is estimated to be about 30-60 C_3H_6 molecules per second if the number of active sites is 10% of the surface titanium ions [128]. If the number of active sites in the silica-supported catalyst used in our study is also only 10%, the TOF for sPS polymerization will be 10-30, which is quite comparable to that of polypropylene catalysts. The fraction of active titanium sites can be even lower than 10%.

The crystallization rate of sPS in solvent-induced crystallization has been known to be fast, hence limited by solvent vapor diffusion through a solid sPS matrix [129, 130]. There are few works about crystallization kinetics for solvent induced crystallization with time-resolved measurements of Infrared Spectra [129-133]. Because of solvent diffusion from outside polymer film into inside film, solvent-induced sPS crystallization has induction period. Solvent-induced crystallization is affected by the kind of solvent and temperature. Over 40 °C, sPS film crystallization is completed in 5 min [129, 131-133]. Especially, at 50 °C solvent induced crystallization with toluene is finished in 3 min [133]. In our polymerization system, reaction temperature is 70°C and such monomer or solvent diffusion resistance is not expected to be present because the polymerization occurs in the solid phase saturated with the liquid monomer and solvent. Since the TOF value estimated from the polymerization kinetic data is not very large, we expect that the sPS co-crystallizes as soon as it is formed at the catalyst site and both styrene/*n*-heptane molecules and sPS chain have sufficient time to intercalate. As a result, the polymer chains can easily form rigid nanofibrils.

From the foregoing SEM and EDX analysis, we can propose a following particle forming and growth mechanism. In a liquid phase slurry polymerization of styrene with silica-supported catalyst, monomer and solvent penetrate into silica gel pores and monomer polymerizes at the surface of silica micrograins. As sPS is formed, it rapidly crystallizes in presence of monomer and solvent molecules. The sPS-monomer/solvent intercalates are rigid and the polymer grows as a thin nanofibril. The nanofibrils from the neighboring active catalyst sites quickly self-assemble to a bundle of nanofibrils of larger diameter of about 30 nm. As these bundles of nanofibrils fill up the void space, a buildup of hydraulic pressure occurs within the catalyst particle and eventually leading to the disintegration of the primary silica particles. Then the expanded void space between the fragmented silica particles are filled up with growing sPS nanofibrils. Since the fibrillar morphology offers a large void space, monomer transport resistance from the bulk liquid phase to the polymer particle is expected to be very small. As a result, the entire polymer particle grows with a uniform interior morphology created by the uniform sized sPS nanofibrils. Also, some nanofibrils can intertwine and form larger fibrils. Finally, polymer particles continue to expand as more sPS fibrils are produced. The sPS fibrils at the surface of the particle are exposed to the liquid phase and the shear stress by mechanical agitation. Then, they collapse and stack themselves like a fused layer. When the reaction time is very short (e.g., 2-10 min), the sPS fibrils at the surface still maintain their fibrillar structures but at longer reaction times, such fibrillar structure is hard to see at the particle surface because the fibrils are exposed to the liquid phase too long and they deform.

4.4 Conclusions

In this chapter, the morphology and crystalline structure of sPS particles synthesized over homogeneous and silica supported $\text{Cp}^*\text{Ti}(\text{OCH}_3)_3$ catalyst with MMAO was reported. The SEM analysis of the nascent sPS particles reveals that the morphology of the sPS particles is characterized by the nanofibrillar morphology in both systems. Our experimental data also indicates that the dimension of sPS nanofibrils is 30-50 nm which is independent of the type of catalyst and the pore size of catalyst support. The XRD analysis shows that the sPS obtained in a liquid slurry polymerization experiments is of the co-crystal. For silica-supported catalytic system, we observed that fragmentation of silica particles has occurred during the polymerization by the SEM and EDX analysis. Although the sPS particle growth is through nanofibrils, the experimental observations indicate that the particle shape replication also occurs in a silica supported sPS polymerization. Based on the observations in our study, we have proposed a mechanism for the growth of sPS particles.

Chapter 5: Syndiotactic Polystyrene Nanofibrils in Silica Nanotube Reactors³

5.1 Introduction

In Chapters 2, 3 and 4, the kinetics of syndiospecific polymerization of styrene, physical changes of a reaction mixture, and the nascent morphology of sPS have been discussed. It was an interesting discovery that the sPS grows in a nanofibrillar form in both the homogeneous and heterogeneous (e.g., over silica-supported catalyst) polymerizations. The study of styrene polymerization in nanoporous reactors to be discussed in this chapter was motivated from the need to understand the mechanism of polymer growth that is believed to be strongly affected by rapid crystallization and gelation of sPS.

Advances in nanoscience and nanotechnology are making rapid and significant impacts in various fields including polymer science and engineering. For example, very high electrical conductivity and high modulus of synthesized in nanoscale pores have been reported [134-137]. Menon *et al.* [134] chemically synthesized nanofibrils of polypyrrole using the pores of nanoporous polycarbonate membrane filters as templates and found that the nanofibrils of polypyrrole can have enhanced conductivities relative to more conventional forms of the polymer.

³ The main part of this chapter has been published in Choi, K. Y., J. J. Han, B. He and S. B. Lee (2008). "Syndiotactic polystyrene nanofibrils in silica nanotube reactors: Understanding of synthesis with ultrahigh molecular weight." *Journal of the American Chemical Society* **130**(12): 3920-3926.

Demoustier-Champagne *et al.* [135] also synthesized polypyrrole nanotubules with polycarbonate particle track-etched membranes via electrochemical polymerization. Higher electrical conductivity of polypyrrole nanotubules compared to the bulk conductivity was shown [135]. Arinstein *et al.* [137] showed the increase in Young's modulus in polymer nanofibers.

Template synthesis, chiral reaction, self assembly, interfacial polymerization, and electro spinning methods are commonly used to make polymeric nano materials [138, 139]. A template synthesis is a very effective method to synthesize nano-structured polymer. The main advantage of template synthesis is that nanotubes, nanowires, and nanorods can be easily prepared and the dimensions of these nanostructured materials can be precisely controlled [138]. For example, Cepak *et al.* [136] prepared polymeric microtubules and nanofibrils with 30 nm-diameter composed of polystyrene, poly(2,6-dimethyl-1,4-phenylene oxide), poly(vinylidene fluoride), poly(methyl methacrylate), polycarbonate, and poly(lactic acid) by depositing a solution of the desired polymer within the pores of microporous alumina and polyester templates. Poly(3,4-ethylenedioxythiophene) (PEDOT) nanotubes of 200 nm-diameter and 20 nm-thickness and 60 nm-diameter and 10 nm-thickness for electrochromic display were synthesized in the porous anodized alumina template via electrochemical polymerization [140]. Mulvihill *et al.* [141] synthesized poly (methyl methacrylate) (PMMA)/silica nanotubes having narrow size distribution using silica nanofiber template via atom transfer radical polymerization (ATRP). They functionalized a silicon core-silica shell nanowire surface with initiators for ATRP.

Then, PMMA polymerization was performed with silica nanotemplate. Finally, PMMA/silica nanotubes were obtained after etching silicon core.

Recently, several reports have been published on the use of mesoporous silica such as MCM-41 or mesoporous silica fiber (MSF) as a new reactor for synthesizing α -olefin polymers with transition metal catalysts. Most notably, Aida and coworkers used mesoporous silica fiber (MSF) with a pore diameter of 2.9 nm as a support for titanocene catalyst to polymerize ethylene [142, 143]. Figure 5.1 shows the mechanism of polymer nanofiber formation over mesoporous silica fiber. The resulting polyethylene had a surprisingly high molecular weight ($> M_v = 6,000,000$ g/mol) with the polymer nanofibrils extruding out from the mesopores of MSF. The extruded polymers formed cocoon-like nanofiber bundles with diameters of about 30–50 μm . The nanofiber bundles were comprised of ultrathin extended-chain crystal fibers 30–50 nm in diameter. Similar observations of polymer morphology were made by several other researchers with mesoporous silica [144–146].

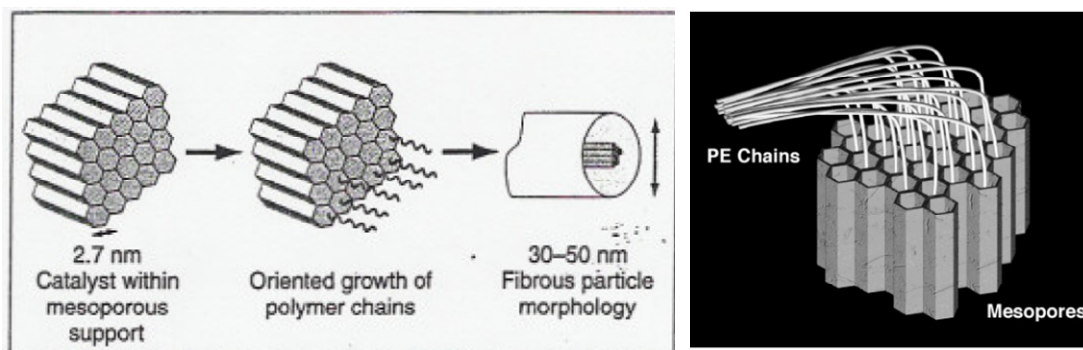


Figure 5.1 Polymer nanofiber formation mechanisms with mesoporous silica fiber [142, 143].

Although these reports offer interesting experimental results of heterogeneous polymerization in nano-scale catalyst pores, not much fundamental mechanistic studies have been reported in the literature. The confined geometry in the nanoscale pores or channels is expected to affect the polymerization reaction kinetics that may lead to the formation of polymers of unusual properties such as ultrahigh molecular weight and crystalline structures. It is also observed that the effects of confinement in the cases of polyethylene and polypropylene reported in the literature are often inconsistent (e.g., some researchers report increased molecular weight while some report no effect on molecular weight) [147].

Several important factors may influence polymerization kinetics and polymer chain growth in the catalyst-anchored nanoscale pores: (i) physical factors, such as dispersion of catalyst on the pore surface, monomer and pore sizes, hindered diffusion of monomer into the pore, and restricted mobility of polymer chains or fibrils; and (ii) chain transfer reaction, such as β -hydride elimination, and chain transfer to monomer and aluminum alkyls that determine the polymer chain length.

In this chapter, we present new experimental results on the use of silica nanotube reactors as a new tool for the polymerization of styrene to sPS using metallocene catalyst. The morphology of the growing polymers in the nano-scale tubes or channels is analyzed using scanning electron microscopy (SEM). Transmission electron microscopy (TEM) is also used to observe the interior of nanotube reactors in which sPS of fibrillar morphology grows. In our work, a silica-coated nanoporous anodized aluminum oxide (AAO) film [148-152] was used as a polymerization reactor (we notate this as SNTRs - *silica nanotube reactors* or as an

SNTR film). A metallocene catalyst ($\text{Cp}^*\text{Ti}(\text{OCH}_3)_3$, pentamethyl cyclopentadienyl titanium trimethoxide) was supported onto the pore surfaces of a silica-coated nanoporous AAO film. Then, monomer is supplied from the bulk liquid phase. As monomer diffuses into the nanopores or channels, polymerization occurs and the polymer extrudes out from the tubes to the bulk phase. Figure 5.2 illustrates the schematic of silica nanotube reactors for sPS polymerization.

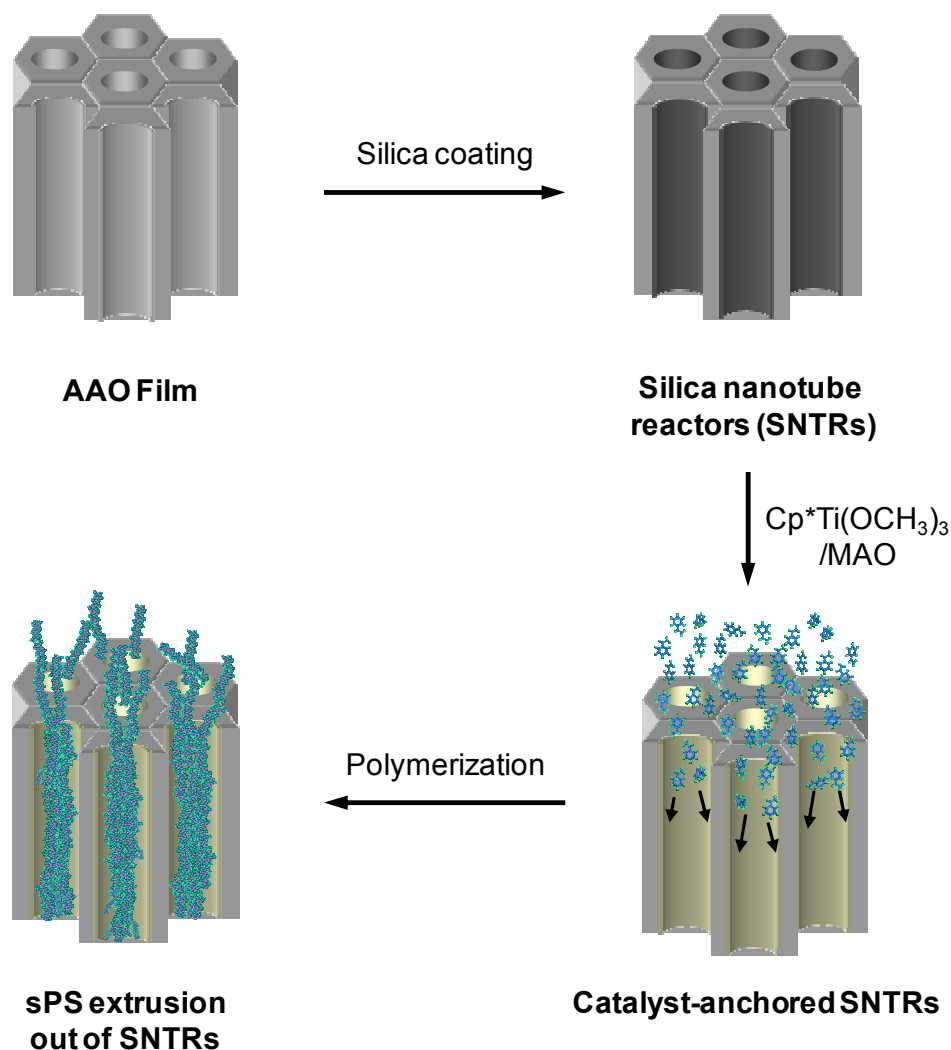


Figure 5.2 Scheme of the synthesis of sPS nanofibrils in catalyst-anchored silica nanotube reactors.

The SNTRs have several important advantages: (i) the film has well-defined nano-scale pores, and the pore length can be readily controlled; (ii) a metallocene/MAO catalyst complex can be effectively anchored onto a silica surface; (iii) the silica layer can be liberated from the AAO film as silica nanotubes containing sPS after polymerization, enabling a direct visual observation of polymer growth by transmission electron microscopy (TEM). A mathematical model is also developed to simulate the molecular weight distribution of sPS in the SNTRs.

5.2 Experimental

5.2.1 Preparation of silica nanotube reactor (SNTR)

An anodized aluminum oxide (AAO) film is used as a basic frame for the nanotube reactor for styrene polymerization was used. The AAO porous film with 200 nm pores (diameter) were purchased from Whatman and the AAO films with smaller size pores (60 nm) were synthesized at the nanoscience laboratory (Department of Chemistry, University of Maryland, Prof. Sang Bok Lee) [151, 152]. Homemade AAO film with a 60 nm pore diameter was prepared electrochemically from an aluminum foil (Alfa Aesar, 99.9995%) via two-step anodization process [153]. The first anodization process was conducted in 0.4 M oxalic acid solutions at 15°C under a constant voltage of 40 V, while the electrolyte was mechanically stirred. To get highly ordered pores of aluminum oxide, the produced alumina layer was removed by wet chemical etching in a mixture of phosphoric acid ~ 6 wt % and

chromic acid ~1.5 wt % at 60°C [153]. The second anodization was carried out under the same conditions and continued until there was no current flow in the electrochemical cell. It is note that commercial AAO films (200 nm) used in our study are open on both ends whereas the homemade AAO films synthesized at Prof. Lee's laboratory are open only one end. Table 5.1 shows the main features of these commercial and homemade AAO porous films. Note that the cross-sections of the commercial AAO films are rather irregular whereas the homemade AAO films have very uniformly shaped cross-sections. Figure 5.3 shows the SEM images of these commercial and homemade AAO films. Note that the cross-sections of the commercial AAO films are rather irregular whereas the homemade AAO films have very uniformly shaped cross-sections.

Table 5.1 Basic properties of anodized aluminum oxide (AAO) porous film

AAO membrane	Commercial	Homemade
Pore diameter	200 nm	60 nm
Membrane thickness	60 μm	5 μm
Pore density	10^9 pores/ cm^2	2.1×10^{10} pores/ cm^2
Pore surface area	3.77×10^{-7} cm^2 /pore	9.42×10^{-9} cm^2 /pore
Avg. surface area	2.3 m^2 /g	23 m^2 /g
Pore volume	1.88×10^{-12} cm^3	8.48×10^{-14} cm^3

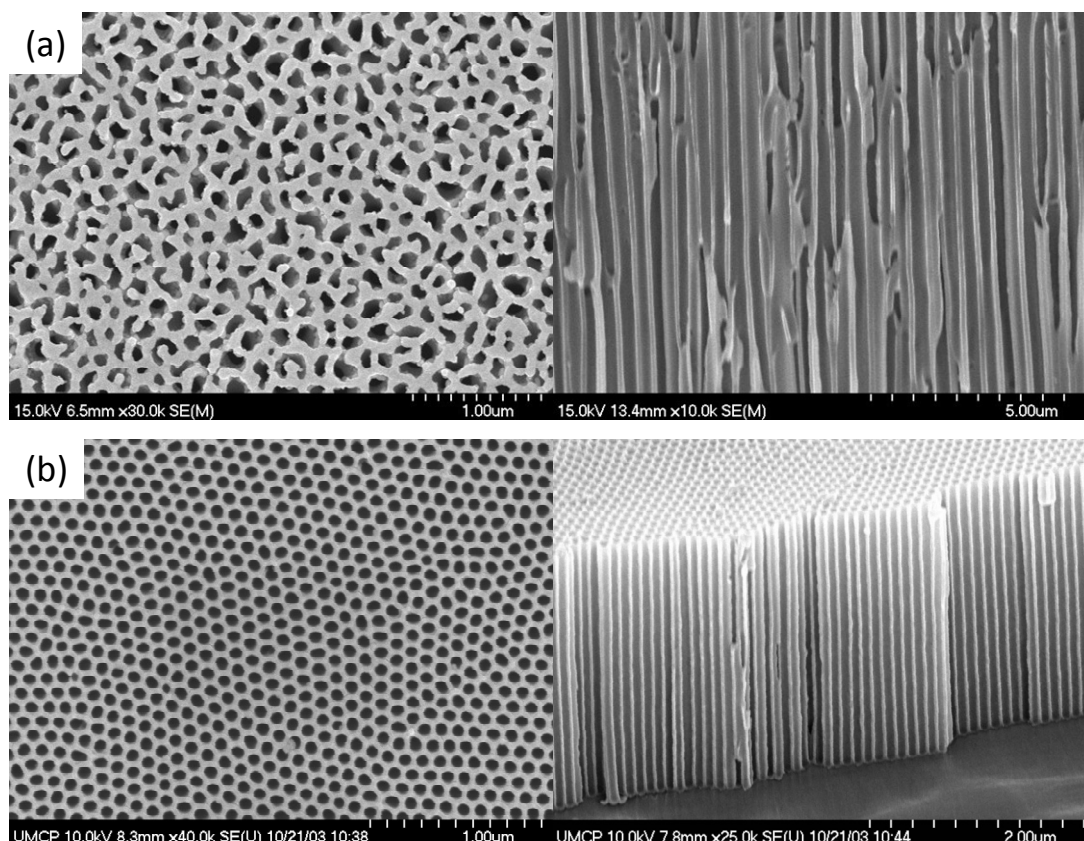


Figure 5.3 SEM images of AAO porous membranes: (a) commercial membrane (pore diameter: 200 nm, pore height: 60μm, (b) homemade membrane (pore diameter: 80 nm, pore height: 3μm).

In our work, the pores inside the AAO films were coated with silica by surface sol-gel (SSG) method as follows. An AAO film is first soaked in SiCl_4 (99.8%) solution. The film is then quickly immersed and washed with fresh hexane for 4 times to remove unabsorbed SiCl_4 . The top surface of the AAO film is gently polished mechanically and the AAO film is placed in methanol/hexane (1:1 v/v) and ethanol mixture before drying in nitrogen flow. Finally, the film is placed in a deionized water bath, followed by washing with methanol and drying step. This

procedure was repeated five to ten times to obtain 3-7 nm thick layer of silica at the pore surfaces.

To support metallocene catalyst onto the inner walls of a silica nanotube reactor, we used the same catalyst preparation technique used to make a silica-supported metallocene catalyst (anchoring catalyst on the surfaces of porous silica particles) as described in Figure 3.4 (Chapter 3). An SNTR film is first treated with a MAO solution in toluene (7.5 vol%) at ambient temperature for 24 hr, washed with toluene, and dried in vacuo. This treatment process is repeated twice. Then, the SNTR film is mixed with a $\text{Cp}^*\text{Ti}(\text{OCH}_3)_3$ catalyst solution in toluene (0.013 mol/L) at ambient temperature for 24 hr, washed with toluene, and dried in vacuo. The top and bottom surfaces of the SNTR film are mechanically polished to remove the catalyst exposed to the bulk liquid phase.

5.2.2 Polymerization in SNTRs

The catalyst deposited SNTR film is placed in a 20 mL glass bottle reactor containing a liquid mixture of styrene and *n*-heptane. MAO was used as a cocatalyst. The concentration of styrene was varied from 2.5 to 5.0 mol/L. The glass reaction bottle was placed in a constant temperature oven. All experiments were carried out at 70°C. The polymerization time for high activity catalyst was 1 - 2 hr and for low activity catalyst, the polymerization was maximum 8 hr. After polymerization, the reaction mixture was removed from the bottle, washed with excess amount of

methanol, and dried *in vacuo*. Reaction conditions of sPS polymerization in the SNTRs are listed in Table 5.2.

Table 5.2 Reaction conditions of sPS polymerization in SNTRs

Run ID	SNTR diameter (nm)	[M] ₀ (mol/L)	[Al] (mol/L)	Reaction Time (min)
C-1	200	2.53	0.048	72
C-2	200	2.53	0.048	120
C-3	200	4.99	0.072	60
C-4	200	5.07	0.048	60
C-5	200	5.13	0	480
H-1	60	2.53	0.048	120
H-2	60	4.99	0.072	120

Solvent: *n*-heptane

5.2.3 Polymer analysis

Dried SNTR/polymer samples were coated with AuPd layer in a Denton DV-503 vacuum evaporator and analyzed by scanning electron microscopy (Hitachi S-4700). Transmission electron microscopic (TEM) analysis was carried out using Zeiss EM10CA. ¹³C Nuclear Magnetic Resonance (NMR) spectrum was obtained at 90°C with Bruker 500 MHz DRX-500 spectrometer. The polymer solution was prepared by dissolving in 1,1,2,2-tetrachloroethane-d₂ (~ 1mg/mL). The solvent peak was observed at 75 ppm and an impurity peak (< 1%) was observed at 120.5 ppm. Differential scanning calorimetry (DSC) analysis was performed at a heating rate of

20°C/min under nitrogen atmosphere using Q1000 (TA Instruments). The molecular weights of sPS samples were measured by high temperature gel permeation chromatography (PL GPC 220, Polymer Laboratories) with trichlorobenzene (TCB) at 160°C. X-ray diffraction (XRD) analysis was performed using Bruker D8 Advanced with GADDS (Bruker AXS).

5.3 Results and Discussion

5.3.1 Morphology and properties of sPS synthesized in SNTRs

The first series experiments of sPS polymerization were carried out using SNTR films a pore diameter of 200 nm. Figure 5.4 shows the reaction vials after sPS polymerization over the SNTR films. Interestingly, sPS fibers emerging from the AAO films are observed. Detaching sPS fibers from the SNTR films is very difficult.

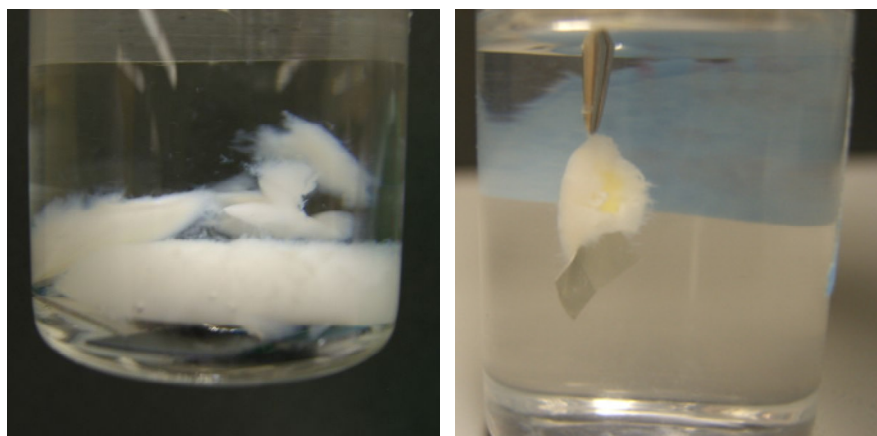


Figure 5.4 white sPS polymers emerging from the SNTR films

Figure 5.5 shows several panels of SEM images that illustrate various aspects of the polymer morphology. Figure 5.5(a) shows a vertical cross-sectional view of the fractured sample near the top of the SNTR surface which is covered with a thick polymer layer (50-60 μm). Here, polymer fibrils formed on the top surface of the silica-coated AAO film have been partially removed. Figure 5.5(a1) shows a very revealing image of the SNTR film surface after removing the top polymer layer. In this SEM photograph, the polymer nanofibrils are seen coming out of the pores. The diameter of these sPS nanofibrils (30-50 nm) is smaller than the pore diameter (200 nm), and the outlet of the 200 nm diameter pores is not completely filled with the polymer nanofibrils. In some pores, several sPS fibers of 30-50 nm are coming out independently or as a bundle (See inset in a1). Figure 5.5(a1) is the direct evidence that sPS fibrils are formed inside the pores and extruded out to the bulk liquid phase.

A magnified image of the cross-section of the polymer layer above the SNTR surface is shown in Figure 5.5(a2). The polymer layer consists of a massive amount of nanofibrils with 30-50 nm diameters. When the top surface of the polymer layer is ~~also~~ magnified as shown in Figure 5.5(a3), we can see that the polymer layer consists of polymer nanofibrils with diameters of about 30-50 nm that are stacked on top of each other. These nanofibrils are stuck together as if they are partially fused. Figure 5.5(b) shows the vertical cross-section of the sPS-filled nanopore channels in the SNTR film below the polymer layer at the surface. It is seen that a large fraction of silica nanotubes are completely filled with long sPS nanofibrils. Some nanotubes are empty, most likely because the sPS nanofibrils are attached to the opposite side of the

fractured SNTR channels. Figure 5.5(b) also shows that the diameters of the nanofibrils detached from the pores are very close to the pore diameter (200nm).

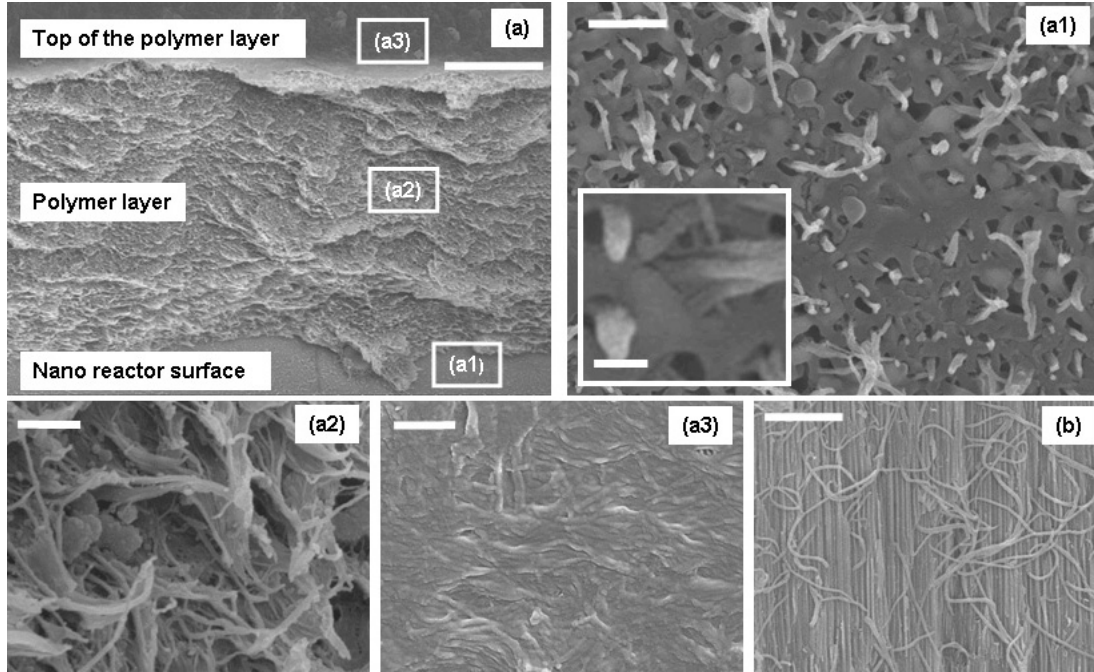


Figure 5.5 SEM images of sPS nanostructures: (a) vertical cross-section of the polymer layer on the SNTR film surface, Run ID: C-4, (a1) top-down view of sPS nanofibrils extruded out from SNTR channels after polymer layer was removed, (a2) sPS fibrils in the vertical cross-sectional view of the polymer layer, (a3) top-down view of the surface of the polymer layer, (b) vertical cross-section of the polymer-filled nanopore channels, Run ID: C-3, scale bars: (a) 20 μm , (a1-a3) 500 nm, inset of (a1) 100 nm, and (b) 5 μm .

The diameters of the sPS nanofibrils (30-50 nm) observed at the outlet of the SNTR film in Figure 5.5 are significantly smaller than the 200 nm diameter sPS

nanofibrils observed inside the pores. It is interesting to note that the 30-50 nm sPS nanofibrils observed in our study are quite similar to those observed in other geometrically confined catalytic polymerization systems. For example, when a mesoporous silica fiber or MCM-41 with a pore diameter of about 3 nm was used for ethylene polymerization with metallocene catalysts, polyethylene chains formed inside the mesopores aggregate into nanofibrils of about 30-50 nm as they exit from the mesopores[142, 143]. These polyethylene nanofibrils aggregate further into polymer nanofibers of about 30-60 μm diameter. But such a large diameter sPS nanofiber bundle was not observed in the current study. Recently Kim and coworkers have reported gas phase ethylene polymerization in a bare AAO film deposited with a $\text{TiCl}_4/\text{Al}(\text{C}_2\text{H}_5)_3$ catalyst.[154]. They observed the bundles of polyethylene nanofibers of 200 nm diameter and 3-5 μm length at the top surface of the AAO film and proposed that the polymer nanofibers were extruded out of the pores. For comparison, the SEM photographs in Kim and coworkers paper are shown in Figure 5.6. Their experimental results indicate that the gas phase ethylene polymerization occurred mostly near the inlet portion of the AAO film pores, forming a thick layer of polyethylene at the film surface. The nanochannels far from the pore entrance were mostly empty, and only small polymer dots and short fibers were observed. It is probably because of severe diffusion resistance for the gaseous ethylene monomer to the active catalytic sites inside the nanochannels.

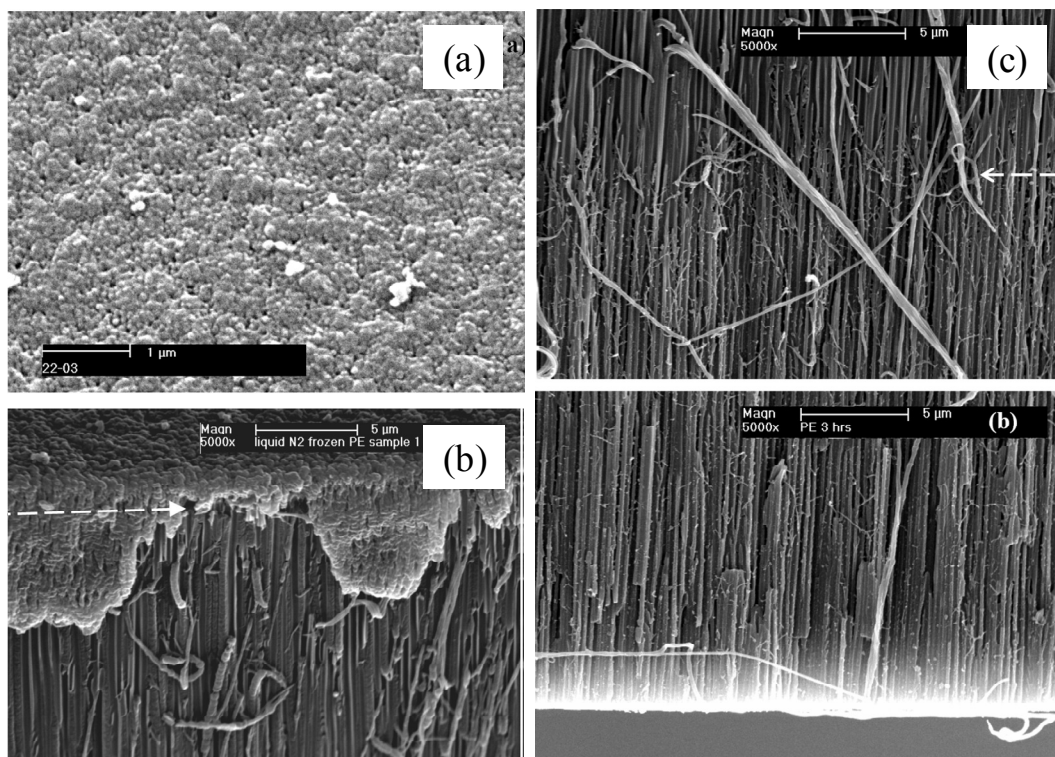


Figure 5.6 SEM photographs of polyethylene synthesized over a bare AAO film deposited with a $\text{TiCl}_4/\text{Al}(\text{C}_2\text{H}_5)_3$ catalyst with gas phase polymerization; (a) top-view, (b) side view, (c) side view of AAO film [154].

To investigate how sPS nanofibrils grow inside the 200-nm SNTR film, we carried out two polymerization experiments, one with MAO for high catalyst activity and the other without MAO cocatalyst for low catalyst activity. The low activity polymerization without MAO enables us to observe the initial stage of fibrils growth. With high activity polymerization with MAO, the later stage of nanofibrils growth can be observed. Figures 5.7(a) and (b) show the cross-sectional views of the SNTR with low activity catalyst and high activity catalyst, respectively. For low catalyst activity, very thin nanofibrils are observed. The diameter of thin nanofibrils is less

than 10 nm. Figure 5.7(a) shows sPS nanofibrils are grown from the pore wall surface. Figure 5.7(b) shows the magnified SEM photo shot of the image shown in Figure 5.5(b). In Figure 5.7(b) sPS nanofibrils (coming off of the left side of the nanotube wall) are observed interconnecting and linking with each other to form a larger nanofibril that is approximately 200 nm in diameter.

The SEM images shown in Figure 5.7 allow us to propose a three-stage growth mechanism for the nanofibrils as follows:

- (i) Stage 1: Very thin nanofibrils, less than 10 nm in diameter as shown in Figure 5.7(a) are formed at the catalytic sites inside the nanopores;
- (ii) Stage 2: These thin nanofibrils aggregate by intertwining with each other to form a larger, rope-like cord. This newly-formed structure has an approximately 50 nm diameter.
- (iii) Stage 3: These larger nanofibrils become intertwined again to form an even larger nanofibril. In Figure 5.7(b), the second-stage nanofibrils (coming off of the left side of the nanotube wall) are observed interconnecting and linking with each other in the third-stage to form a larger nanofibril that is approximately 200 nm in diameter.

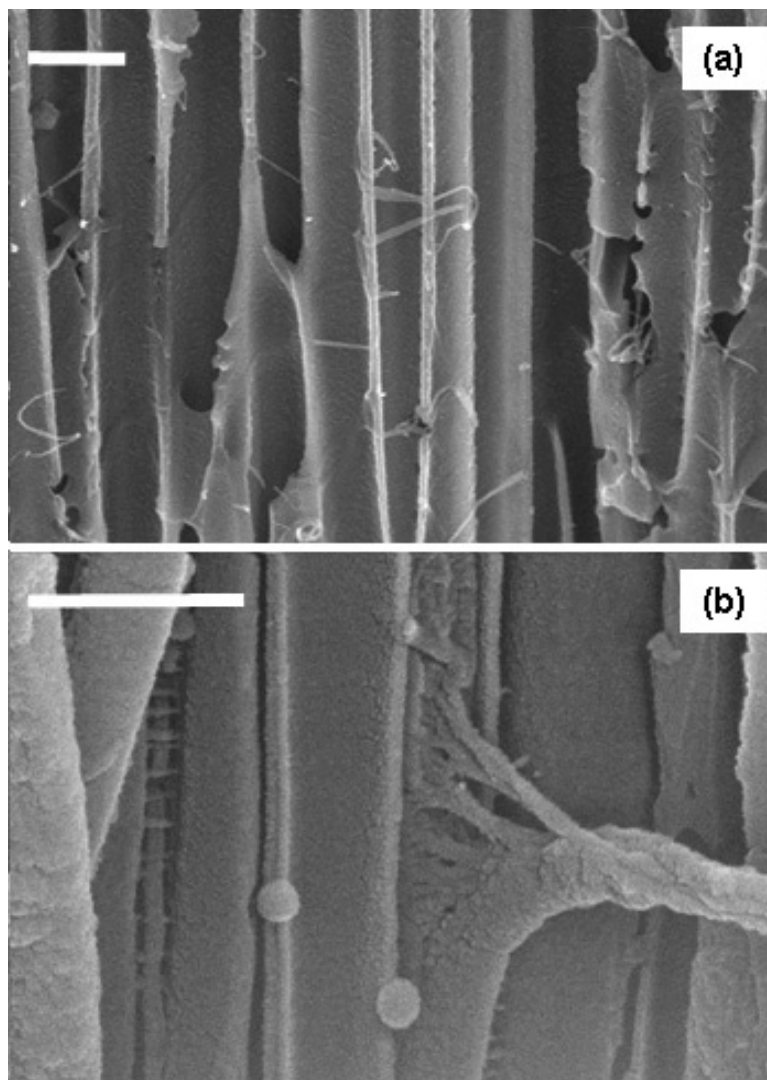


Figure 5.7 SEM images of sPS nanofibrils inside SNTR pores of diameter 200 nm:

(a) low catalyst activity without MAO treatment, Run ID: C-5; (b) high catalyst activity with MAO treatment, Run ID: C-3, scale bars: 500 nm.

It is interesting that this final, large nanofibril in Stage 3 is approximate to the size of the SNTR pore itself: only one large nanofibril in each pore is seen in a vertical cross-sectional view of the SNTR nanopore (Figure 5.7(b)). It is in contrast to

the top-down view shown in Figure 5.5(a1) where multiple strands of sPS are seen extruding from each pore. It is thought that these multiple strands might be the second-stage nanofibrils that later intertwine to form the final, large nanofibril in the third stage. Within the nanopore, the movement of the second-stage nanofibrils can be restricted because of the increased tube pressure and minimal presence of liquid. Thus, these nanofibrils further intertwine into a large nanofibril. However, at the surface of the nanopore, the nanofibril exists in a liquid environment at a far lower pressure. Since there is ample room for the sPS nanofibril to spread out, this large, coiled nanofibril can then become loosened. The second-stage nanofibrils can separate from each other into multiple sPS strands, and we believe that this is the image that we see in Figure 5.5(a1).

The growth of sPS nanofibrils inside the SNTR is further investigated using a 60-nm SNTR film with a smaller pore diameter (inner diameter = 45 nm, outer diameter = 60 nm) and a length of 5 μm . Figure 5.8 shows the resulting SEM images of the SNTR and the polymer fibers in the cross-section of the 60-nm silica nanotube reactor. Unlike the sPS sample analyzed in Figures 5.5 and 5.7, the 60-nm SNTR film in Figure 5.8 was fractured incompletely so that it was not vertically split through to the bottom. Instead, the membrane was split only $\sim 4 \mu\text{m}$, as opposed to the full height of 5 μm . Fortunately, this cut enabled the film sides to split open, and both the vertical and horizontal cross-sectional areas could be viewed. Figure 5.8(b) shows the interior of the split-open SNTR. Notice that most of the silica nanotubes are filled with sPS nanofibrils. Some of these nanofibrils are detached from the reactor tube walls, but they remain connected to the tubes underneath. It is also seen that some of

these nanofibrils are cut and hung loose between the top and bottom pieces of the film. Figure 5.8(c) is the magnified image of the horizontal cross-section. Notice that some of the nanofibrils inside the silica nanotubes are still connected to the side wall of the fractured reactor tube surfaces. Also, only one polymer nanofibril is filling each of the 60-nm nanotubes. Recall that in Figure 5.5 for the 200-nm SNTR, multiple sPS fibrils were present in the tubes.

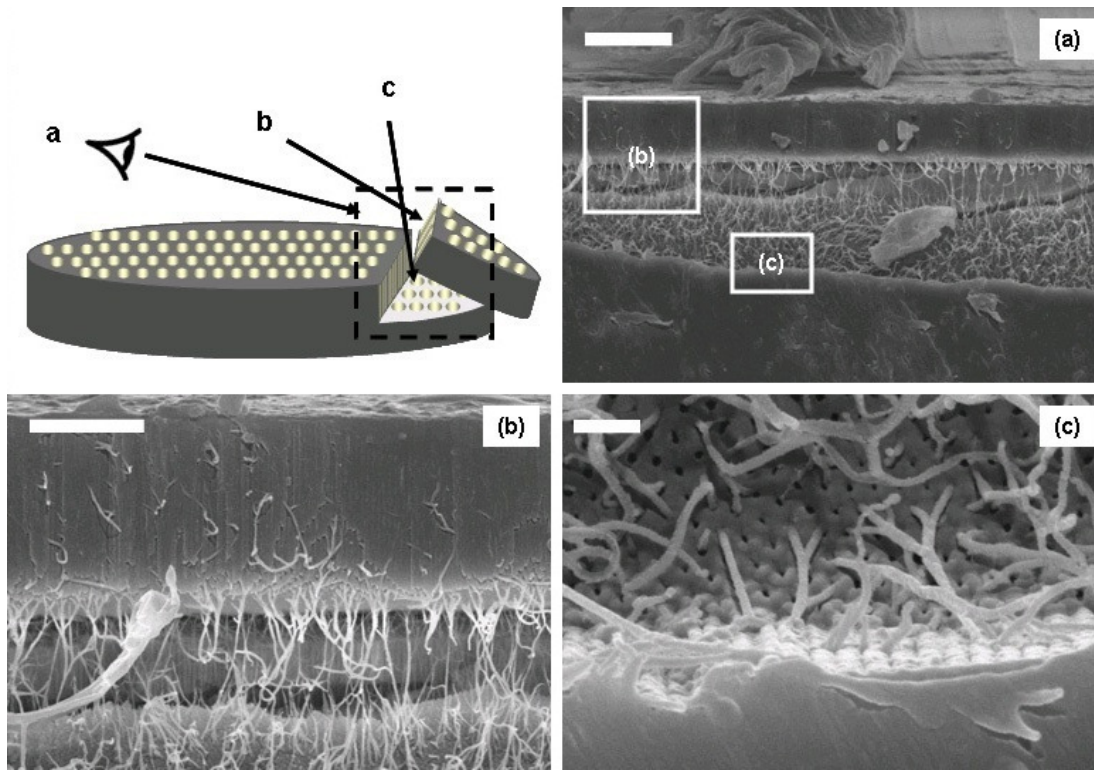


Figure 5.8 SEM images of sPS nanostructures synthesized in a 60-nm SNTR film, Run ID: H-1, (a) vertical cross-section of the SNTR film, pore diameter = 60 nm, (b, c) magnified images. The cartoon in the top left corner illustrates the viewing angles for the images (a)-(c). The polymer layer on the SNTR film and the sPS nanofibrils are omitted for clarity, scale bars: 5 μm for (a), 2 μm for (b), 250 nm for (c).

The sPS nanofibrils were directly observed inside the 60-nm silica nanotubes (SNTs) by TEM. The top of the 60-nm SNTR film was mechanically polished to remove the polymer layer that was extruded out from the pores of silica nanotubes and deposited on the top surface. The silica nanotubes containing sPS were liberated after dissolving alumina selectively in a 0.1N NaOH solution, and then collected by filtration. Figure 5.9(a) shows the TEM images of the nanotubes containing sPS. Each silica nanotube is partially filled with a single sPS nanofibril whose diameter is smaller than the pore diameter. Since the inner pore diameter is only 45 nm, the sPS nanofibrils cannot intertwine into larger fibrils that were observed in Figure 5.7(b) as the third-stage nanofibrils. Figure 5.9(b) shows the pieces of broken silica nanotubes. Inside a broken silica nanotube, the sPS remains unbroken but bent with the same angle as the silica tube. It is quite interesting to observe that the sizes of the sPS nanofibrils are nearly constant along the tube length. This suggests that the polymerization reaction occurred uniformly throughout the interior of SNTR nanochannel, which implies that the catalysts are anchored well and are homogeneously active throughout the SNTR channels. Figure 5.9(c) shows a high resolution TEM image of the exposed area of a sPS nanofibril out of the broken silica nanotube in Figure 5.9(b).

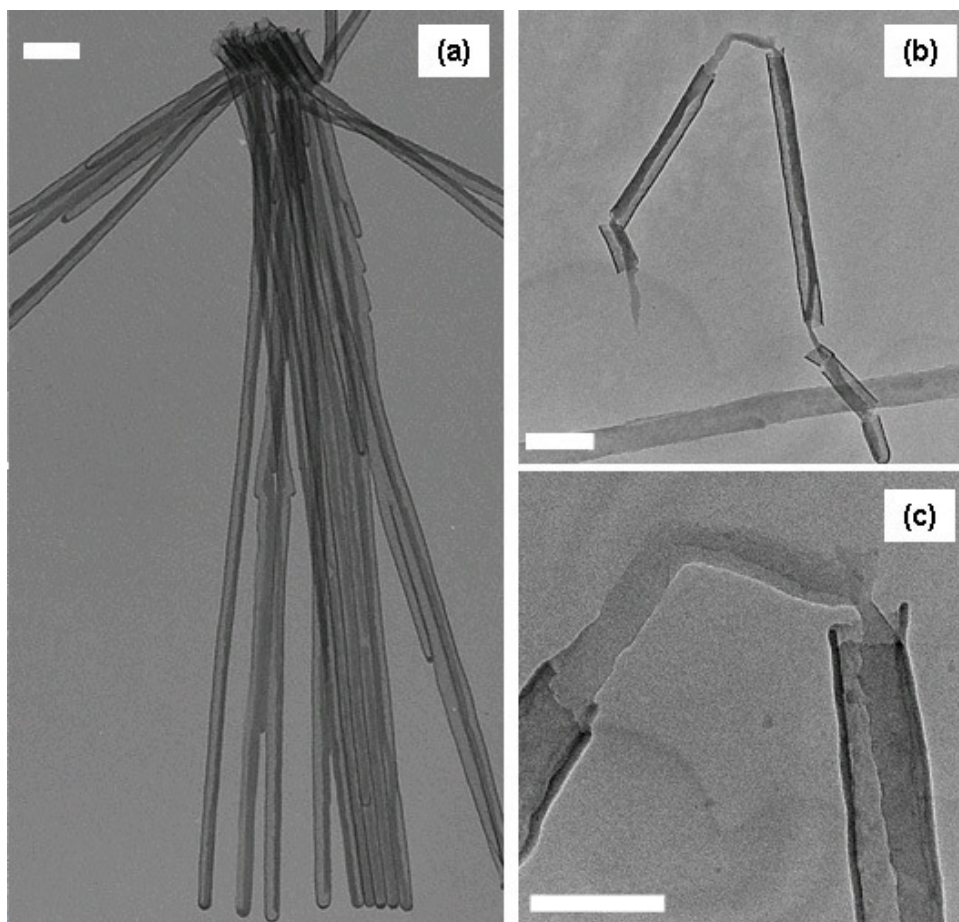


Figure 5.9 Transmission electron micrographs (TEM) of 60 nm diameter silica nanotubes containing sPS polymerized at the inner surface of the pore walls, Run ID: H-2, scale bars: 250 nm for (a) and (b), 100 nm for (c).

The sPS nanofibrils were analyzed by ^{13}C NMR spectroscopy (Figure 5.10). The characteristic peak at 145.5 ppm confirms that the polymer fibrils obtained are syndiotactic polystyrene, and the entire spectrum matches very well with those of sPS reported in the literature [6, 155]. The syndiotacticity of the sPS fibrils measured by the ^{13}C NMR is 100% (i.e., single peak at 44.3 ppm in the 43.0-47.0 ppm range). It is

quite interesting that the sPS produced in the SNTRs have near perfect syndiotacticity whereas the same catalyst used in the SNTRs produce sPS with 91-98% syndiotacticity when polymerized over silica supported catalyst or homogenous catalyst.

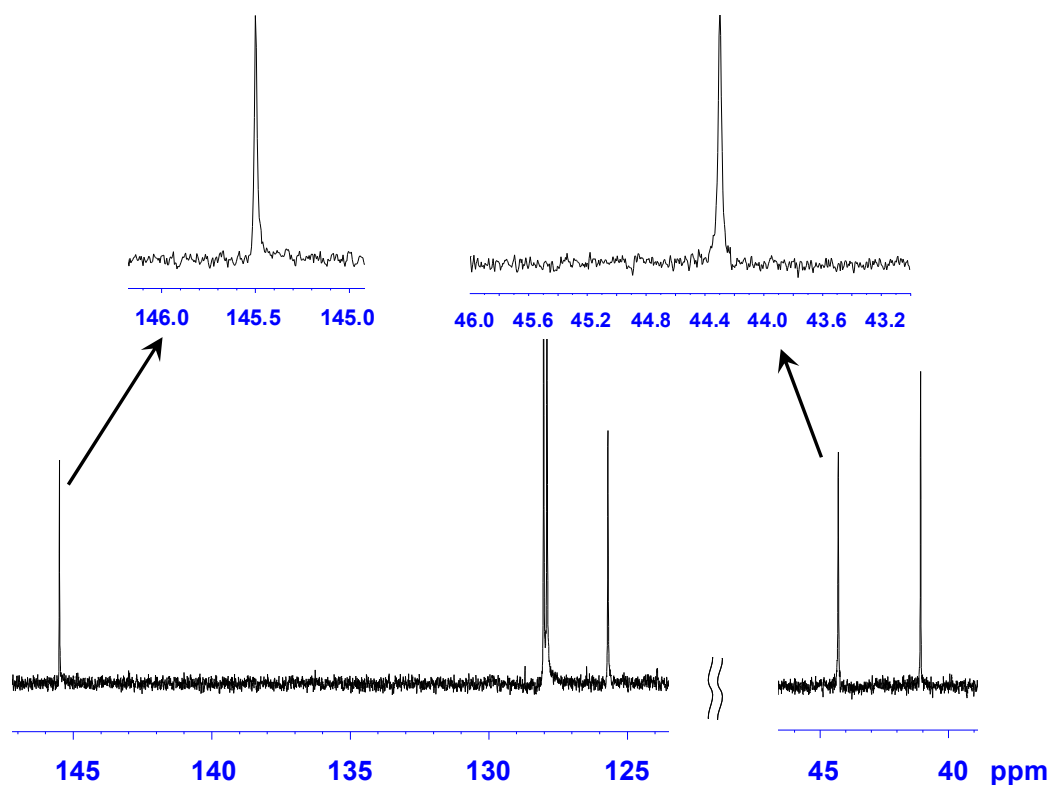


Figure 5.10 ^{13}C NMR spectrum of sPS nanofibrils,

Molecular weight and molecular weight distribution (MWD) are important polymer parameters that have significant impacts on the polymer's physical, mechanical, and rheological properties. Figure 5.11 shows two MWD curves of the sPS polymerized using the silica nanotube reactor and the silica-supported $\text{Cp}^*\text{Ti}(\text{OCH}_3)_3$ catalyst at 70°C . Here, a striking difference between the two sPS

samples is observed: the sPS produced in the SNTR has the molecular weight ($M_w = 928,000$ g/mol) which is 4.2 times larger than the molecular weight of the sPS obtained using silica-supported catalyst at higher monomer concentration ($M_w = 221,000$ g/mol). In the MWD curve for the SNTR polymer, we observe that about 40 wt.% of sPS has molecular weight larger than 1,000,000 g/mol. The largest molecular weight detected in the MWD curve is very close to 5,000,000 g/mol. This extremely large molecular weight has not previously been reported in the literature for the sPS synthesized over heterogeneously supported metallocene catalysts.

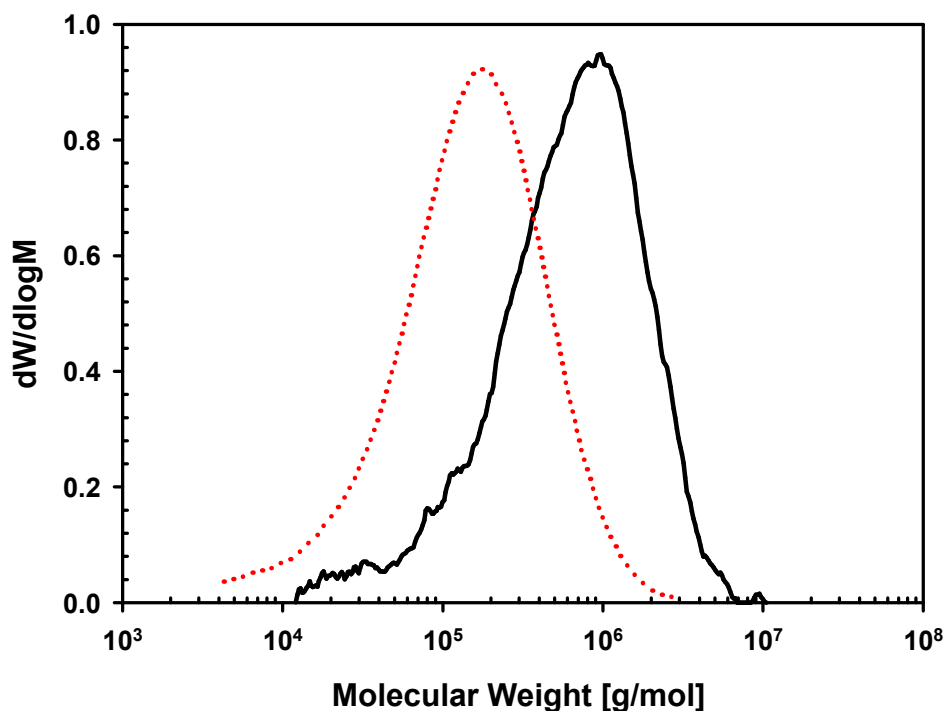


Figure 5.11 Molecular weight distributions of sPS: SNTR (200 nm), Run ID: C-2, $M_n = 275,000$ g/mol, $M_w = 928,000$ g/mol (solid line); silica-supported catalyst, $[M]_0 = 3.24$ mol/L, reaction time = 60 min, $M_n = 68,400$ g/mol, $M_w = 221,000$ g/mol (dotted line).

Let us consider the reason why the sPS produced in the SNTRs has higher molecular weight than the sPS produced with silica-supported catalyst. To obtain high molecular weight, propagation reaction rate must be far larger than the chain transfer reaction rates. In sPS polymerization termination of polymer chain growth occurs by The chain transfer reactions that occur in sPS polymerization are: chain transfer to monomer, chain transfer to aluminum components, and β -hydride elimination [15]. The high molecular weight observed from the SNTRs might be caused by the steric hindrance for the chain transfer reactions at the propagating active centers. According to the literature, the molecular weight enhancement was also observed in ethylene polymerization with the mesoporous silicas that have pore diameters (~ 3 nm), which are far smaller than the silica nanotubes used in this study [143, 146]. Yet, the confined geometry effect in sPS polymerization in SNTR film is quite significant. We have found that the sPS in the 60 nm SNTR was extremely difficult to dissolve in trichlorobenzene at 160°C for several days. GPC analysis of the partially soluble fraction of the polymer sample from the 60 nm SNTR was attempted but the results were inconsistent.

The sPS polymer synthesized in SNTRs was also analyzed by differential scanning calorimetry (DSC). DSC thermograms of three sPS samples synthesized with SNTR, silica-supported catalyst, and homogeneous catalyst are shown in Figure 5.12. From DSC thermograms, it was found that the first scan melting point was 278.5°C, which is much higher than the reported value of 270°C for sPS [3, 7]. Such a high melting point of nascent sPS of ultrahigh molecular weight has not been reported in the literature for a nascent sPS synthesized over heterogeneous catalysts.

A similar phenomenon of increased crystalline melting point was also observed in polyethylenes synthesized over metallocene catalysts on mesoporous silica fibers or MCM-41 [146]. With the MCM-41-supported $\text{Cp}_2\text{TiCl}_2/\text{MAO}$, Ye *et al.* [146] synthesized PE fibers which had high melting temperature ($T_m = 140^\circ\text{C}$) in comparison with the melting temperature of PE ($T_m = 133\text{-}135^\circ\text{C}$) synthesized by conventional methods. The increase in the melting point has been attributed to the formation of extended chain crystals when polyethylene nanofibers are extruded out of the mesopores of 3 nm diameter that prevented the polyethylene chains from folding within the mesopores [69, 146, 156, 157].

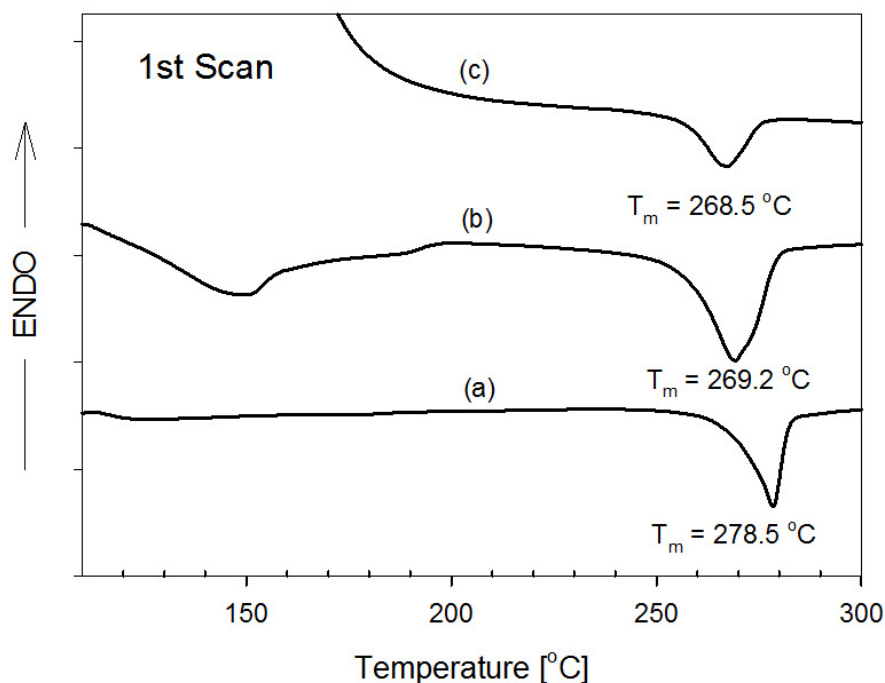


Figure 5.12 DSC thermograms of sPS: (a) SNTR, Run ID: C-1, (b) silica supported catalyst, $[\text{M}]_0 = 4.86 \text{ mol/L}$, reaction time = 10 min, and (c) homogeneous catalyst, $[\text{M}]_0 = 3.42 \text{ mol/L}$, reaction time = 10 min.

The crystalline structure of nascent sPS nanofibrils was analyzed by XRD. As discussed in Chapter 4.3, sPS is known to have complex crystalline structures (α , β , γ , and δ form crystals) depending upon the crystallization methods such as solvent casting and thermal annealing [23, 35, 132]. Figure 5.13 shows the XRD patterns of the sPS samples polymerized over homogeneous $\text{Cp}^*\text{Ti}(\text{OCH}_3)_3$ catalyst, silica-supported $\text{Cp}^*\text{Ti}(\text{OCH}_3)_3$ catalyst, and SNTR. The vertical lines indicate the characteristic peak positions of δ -form sPS crystal ($2\theta \approx 8, 10, 17, 20, 23.4^\circ$). [29] The sPS samples synthesized over homogeneous and silica-supported catalysts show δ form crystalline structures. The XRD pattern (a) for the sPS nanofiber sample synthesized in SNTR also show the peaks at 8 and 10° but the characteristic peaks at $2\theta \approx 17, 20$, and 23.4° are not distinctive. The crystalline morphology of sPS is affected by several factors such as the complex formation with solvent molecules and thermal treatment procedure [158]. The exact reasons for the discrepancies in the XRD patterns at $17, 20$, and 23.4° are not clear at this point.

For α or β -form sPS crystals, the crystalline melting point (T_m) tends to increase, as the thickness of lamellar is increased. [159-161] The XRD analysis indicates that all the sPS samples obtained in our polymerization experiments have the δ -form crystalline structures. When a δ -form crystal is heated above the glass transition temperature, it is transformed to the γ -form crystal, and above 200°C , the γ -form is transformed to α -form crystals [23].

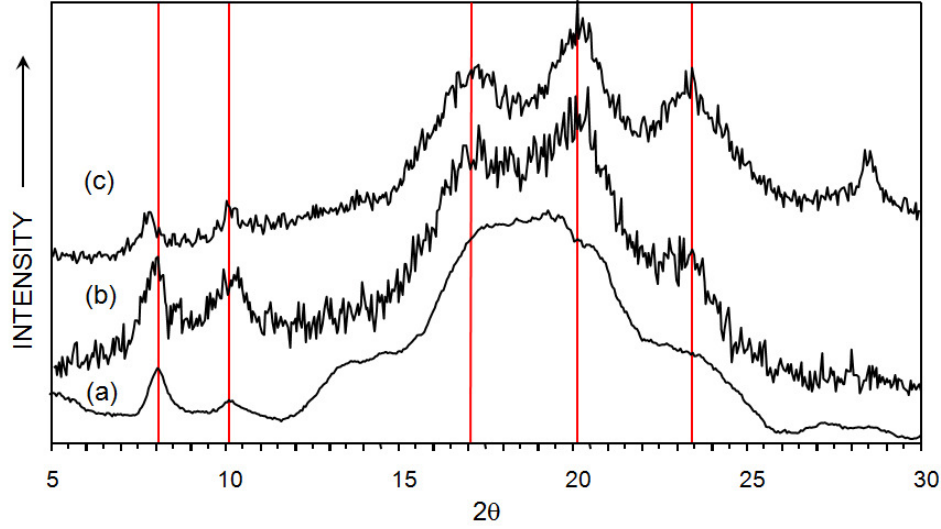


Figure 5.13 XRD patterns of sPS samples: (a) sPS nanofibrils synthesized in 200-nm SNTR, Run ID: C-1 (b) sPS particles synthesized over silica-supported catalyst, $[M]_0 = 2.03$ mol/L, reaction time = 60 min (c) sPS particle synthesized with homogeneous catalyst, $[M]_0 = 8.74$ mol/L, $T = 50$ °C, reaction time = 60 min.

The effect of lamellar thickness (ℓ_c) on the crystalline melting temperature (T_m) can be represented by the Gibbs-Thompson equation[161]:

$$T_m = T_m^0 \left[1 - \frac{2\sigma_e}{\Delta H_f^0 \ell_c} \right] \quad (5-1)$$

where T_m^0 is the equilibrium melting temperature, ΔH_f^0 is the enthalpy of fusion per unit volume, and σ_e is the fold-surface energy. The Gibbs-Thompson equation indicates that the larger the crystalline lamellar thickness is, the higher the melting temperature becomes. With the parameters of the Gibbs-Thompson equation

(T_m^0 and $\sigma_e / \Delta H_f^0$) for α -form sPS crystals [161], we calculated the lamellar thickness of sPS synthesized in the SNTR. For the sPS with a melting point of 278 °C, the calculated lamellar thickness is 31.6 nm, which is far larger than the lamellar thickness of the sPS with lower melting point (6.33 nm at $T_m = 271.6$ °C) [161]. Since the calculated lamellar thickness for our sPS sample is almost the same as the diameter of a sPS fibril in the 60-nm SNTR, it is thought that crystalline lamellar, if present, would be very hard to see by TEM. Indeed, the high resolution TEM analysis of the sPS nanofibers inside the SNTR indicates the absence of crystalline lamellar structure (Figure 5.9(b)).

5.3.2 Modeling of monomer diffusion and reaction in SNTRs

In a bulk phase reaction, monomer concentration is only affected by polymerization reaction rate. In a slurry phase, however, monomer concentration is also affected by monomer partition between the liquid phase and the solid phase (Chapter 2 and 3). In SNTRs, monomer concentration may change along the pore length due to diffusion and reaction.

In one cylindrical membrane pore, monomer concentration profile can be calculated as

$$\frac{\partial C_A}{\partial t} = D_A \frac{\partial^2 C_A}{\partial x^2} - \frac{4k_s}{d_p} C_A$$

Initial condition:

$$C_A(x, 0) = C_{A0} \quad (5-2)$$

Boundary conditions:

$$C_A(0, t) = C_{A0} \text{ and } C_A(L, t) = C_{A0} \text{ for commercial}$$

$$C_A(0, t) = C_{A0} \text{ and } \frac{\partial C_A(L, t)}{\partial x} = 0 \text{ for homemade}$$

where C_A is monomer concentration, D_A is the diffusivity of monomer, k_s is the rate constant per surface area, and d_p is a diameter of pore.

Since the polymerization occurs only at the wall surface, propagation rate constant needs to be modified so that the reaction rate can be calculated per unit catalytic surface area. We assume that the Ti loading of SNTR surface is almost same as that of silica supported metallocene catalyst, because the surface of SNTR is coated by silica. The Ti loading of silica-supported catalyst surface was 1.1×10^{-6} mol-Ti/m² (The average surface of Davison 952: 280 m²/g-silica, Ti loading of silica-supported catalyst: 2.94×10^{-4} mol-Ti/g-silica). Therefore, rate constant per surface area, k_s , can be calculated as:

$$k_s = \frac{k_p \times \text{Ti loading}}{\text{surface area of silica}} \quad (5-3)$$

and k_s value is 2.4×10^{-9} m/sec.

The sPS polymerization rate can be approximated as the first order with respect to monomer concentration and catalyst concentration, respectively. But such approximation may not be valid in a heterogeneous polymerization system as discussed in section 3.3 in Chapter 3. If we assume no catalyst deactivation, the sPS production rate can be expressed as:

$$R_p' = k_s[M] \times S_A \times \rho_{PS} \text{ (g-sPS/min)} \quad (5-4)$$

where k_s is a propagation rate constant, $[M]$ is mole concentration of monomer (mol/L), S_A is the surface area of pore, and ρ_{PS} is the density of polystyrene.

For the simulation, we selected Run ID: C-2 ($[M]_0 = 2.53$ mol/L (styrene to heptane ratio = 4/6 volume ratio)) for which MWD is shown in Figure 5.11. Using eq. (5-4), the sPS production rate was calculated and the value of the sPS production rate in a commercial AAO film pore is 1.49×10^{-12} g-sPS/min. With the pore volume listed in Table 5.1 and the sPS production rate, pore-filling time was calculated as

$$t_{PF} = \frac{\text{pore volume (cm}^3\text{)} \times \text{density of PS (g/cm}^3\text{)}}{\text{sPS production rate (g-sPS/min)}} \quad (5-5)$$

For commercial AAO film, the time that one pore is filled with polymer is just 1.3 min. Compared to the whole reaction time, 120 min, pore-filling time is very fast. For homemade AAO film, pore-filling time is only 0.4 min. Thus, we can assume that SNTR pores are filled with polymer during whole polymerization time. To solve eq. (5-2), the diffusivity of styrene is needed. Since SNTR pores are filled with polymer at the early stage of polymerization, the diffusivity of styrene in an sPS phase should

be considered. In this simulation, the diffusion coefficient of styrene in atactic PS ($9.6 \times 10^{-13} \text{ m}^2/\text{s}$) [162] is used to calculate monomer concentration profile.

Eq. (5-2) was solved by a PDE solver in MATLAB. Figure 5.14 and 5.15 show the monomer concentration profiles in commercial SNTRs (both ends are open; length = 60 microns) and homemade SNTR SNTRs (only one end is open; length = 5 microns). In commercial SNTRs, monomer concentration drops from 2.53 mol/L at the pore inlet to 0.040 mol/L in the center of a pore. The time to reach equilibrium concentration is very fast (in 4 min). Since the monomer concentration at the center of the pore is very low, polymers are produced mostly near the pore entrance regions. For homemade SNTRs (Figure 5.16), the concentration of monomer at the closed pore end is 1.13 mol/L. The pore length of homemade SNTRs is only 5 microns and the monomer concentration ~~is~~ gradient is not quite significant. Therefore, the overall polymerization rate is higher for the homemade SNTRs.

5.3.3 Modeling of molecular weight distribution (MWD)

The effect of the monomer concentration gradient on the molecular weight and MWD has also been analyzed. For MWD calculation, we sectioned an SNTR pore into 60 sub-regions, and average monomer concentration and molecular weight distribution were calculated at every sub-region. Figure 5.16 illustrates how to section a pore.

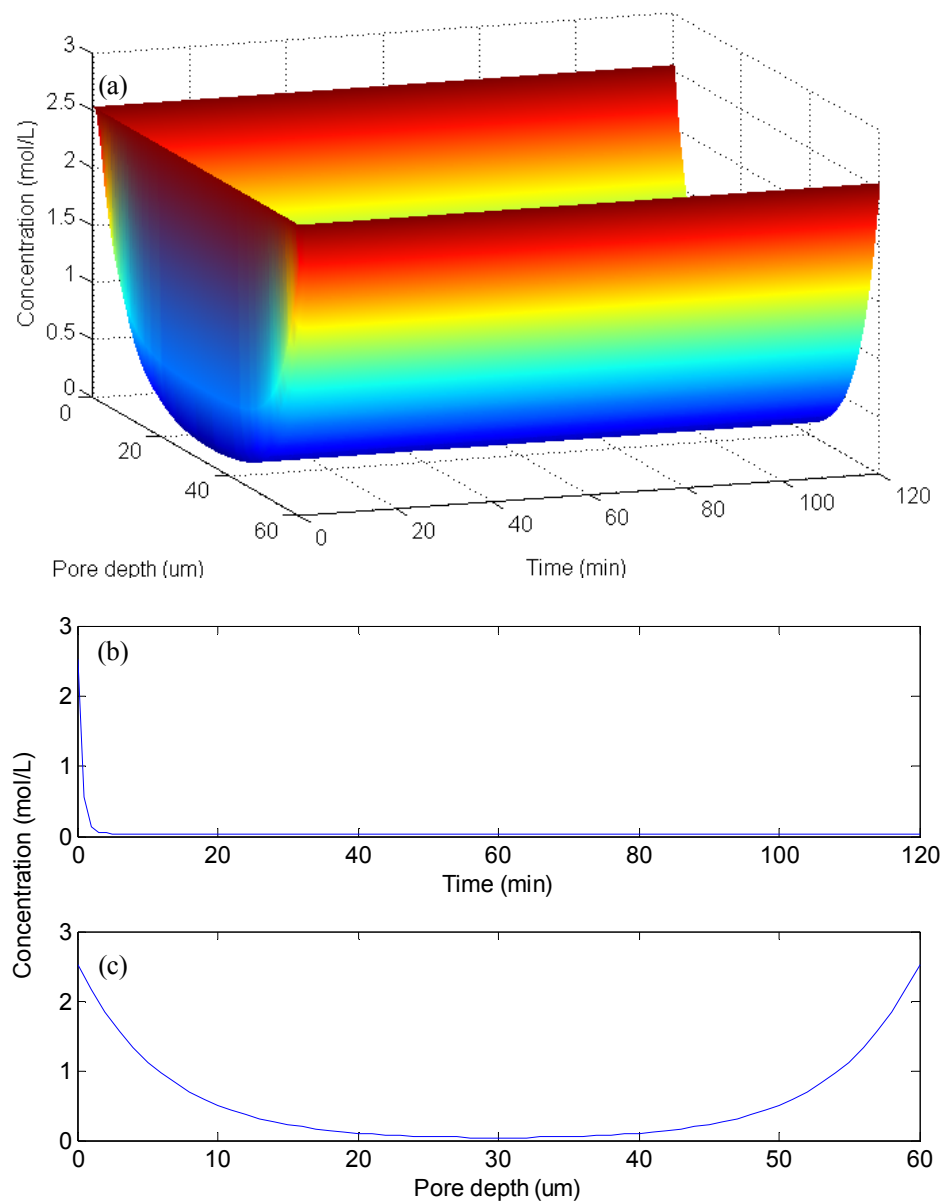


Figure 5.14 Monomer concentration profile in SNTR pore; $[M]_0 = 2.53$ mol/L, Commercial SNTR; pore diameter: 200 nm, pore length: 60 μm , (a) 3D plot of monomer concentration, (b) monomer concentration at the center of a pore, (c) monomer concentration along the pore depth.

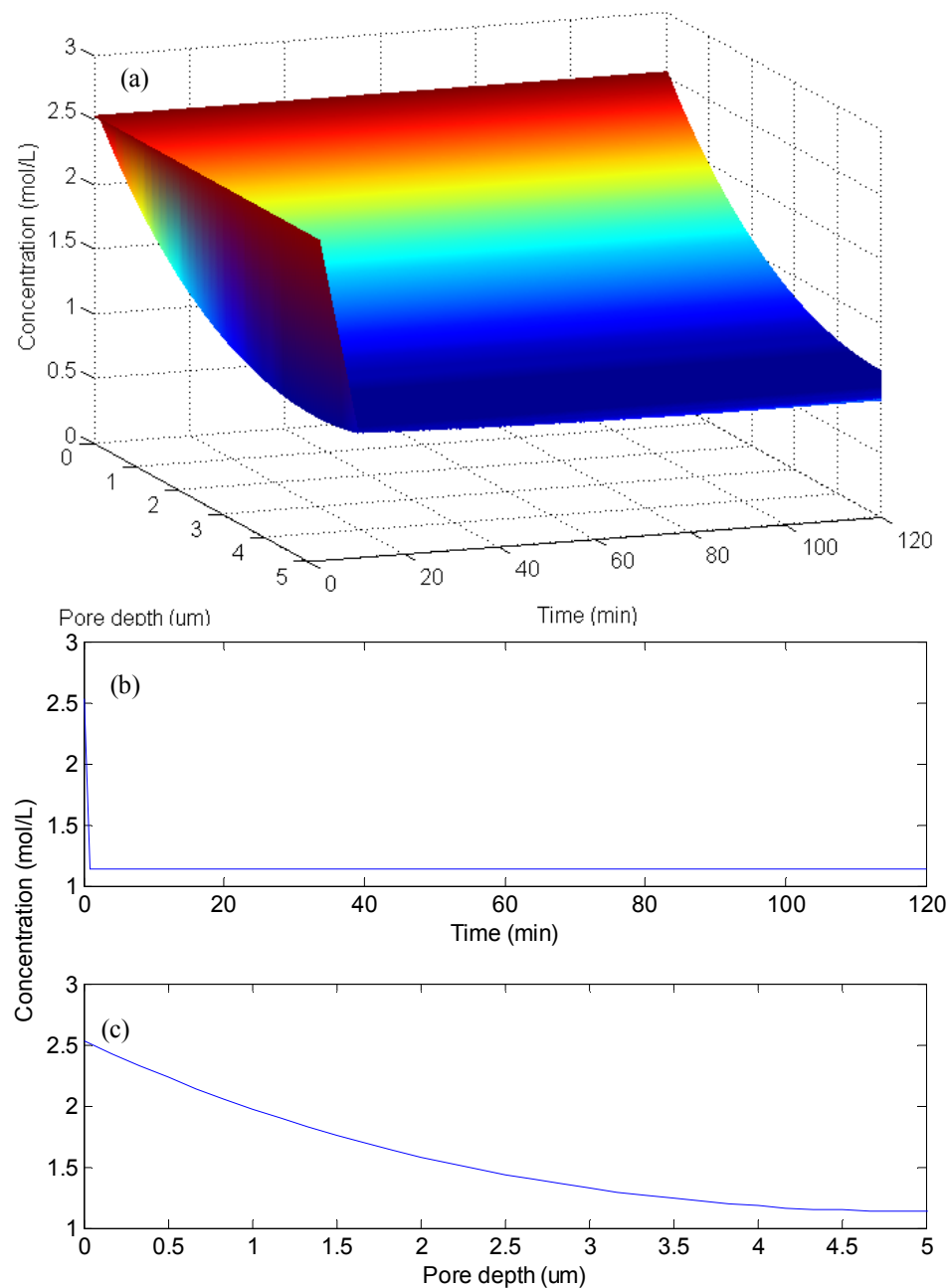


Figure 5.15 Monomer concentration profile in an SNTR pore; $[M]_0 = 2.53$ mol/L, Homemade SNTR; pore diameter: 60 nm, pore length: 5 μm , (a) 3D plot of monomer concentration, (b) monomer concentration at the center of a pore, (c) monomer concentration along the pore depth.

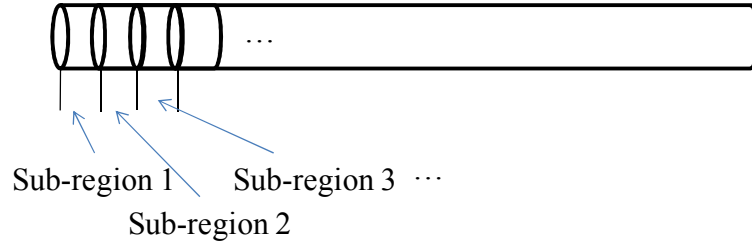


Figure 5.16 Schematic diagram of sectioning method.

For the simulation of MWD, the weight fraction of the polymer of chain length x produced in sub-region i , ($W_i(x)$), is given by the following Schulz-Flory distribution function:

$$W_i(x) = \tau_i^2 x \exp(-\tau_i x) \quad (5-6)$$

where the parameter τ_i is defined as follows:

$$\tau_i = \frac{R_{t,i} + R_{d,i}}{R_{p,i}} = \frac{k_{tM}[M]_s[P] + k_{t\beta}[P] + k_d[P]}{k_p[M]_s[P]} = \frac{k_{tM}[M]_s + k_{t\beta} + k_d}{k_p[M]_s} \quad (5-7)$$

$$(\text{or } \tau_i = \frac{R_{t,i}}{R_{p,i}} = \frac{k_{tM}[M]_s[P] + k_{t\beta}[P]}{k_p[M]_s[P]} = \frac{k_{tM}[M]_s + k_{t\beta}}{k_p[M]_s})$$

$[P]$ represents the total active site concentration (i.e., $[P] = [C^*] + \sum_{n=1}^{\infty} [P_n]$).

Then, the weight chain length distribution of sPS is calculated by the following equation

$$X_w = \sum_i \phi_i x W_i(x) \quad (5-8)$$

The following parameters, obtained for the silica-supported catalyst system, are used in the model simulations. Table 5.3 lists the model parameters.

Table 5.3 the model parameters for MWD calculation

k_s	$k_{t\beta,s}$	$k_{tM,s}$	D_A
m/sec	1/sec	m/sec	m ² /s
2.4×10^{-9}	2.3×10^{-12}	9.2×10^{-13}	9.6×10^{-13}

Figure 5.17 shows the MWD curves of sPS obtained over SNTRs. Symbols are the experimental data from GPC analysis and line curve is the simulation result. Calculated weight average molecular weight of polymer is 156,000 g/mol and polydispersity index (PDI) is 3.77. Table 5.4 compares the experimental results and the simulation results. Although PDI is broad enough for model calculation compared with experimental result, weight average molecular weight is much smaller than real data (symbols). In the model simulations, the nonuniform monomer concentration profiles in the SNTR pore were taken into consideration but it appears that the monomer concentration effect on the molecular weight distribution is almost negligible.

Table 5.4 MWD calculation without chain transfer rate constant change

	Experimental	Simulation
Mn, g/mol	275,000	41,400
Mw, g/mol	928,000	156,000
PDI	3.37	3.77

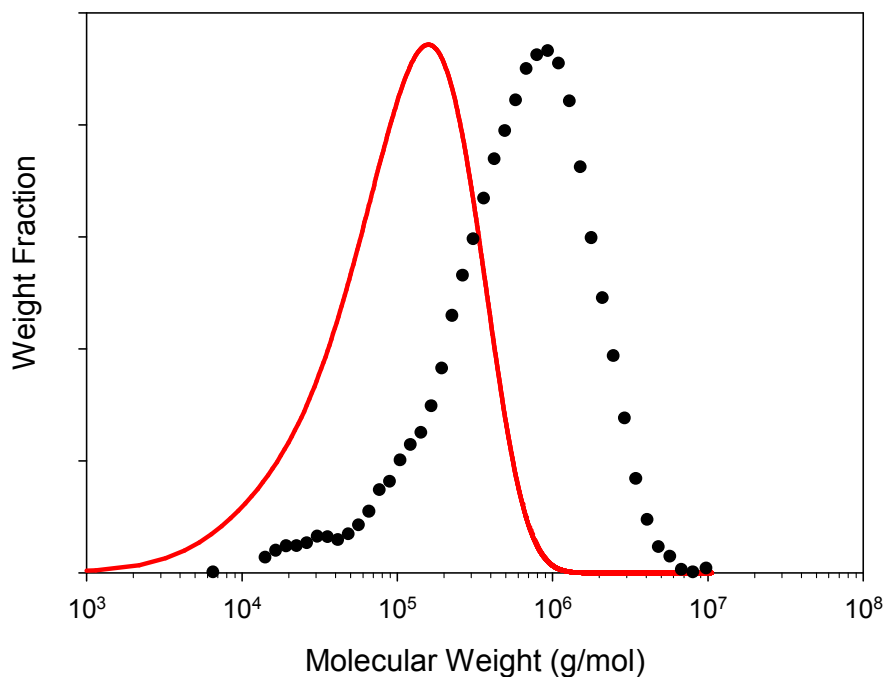


Figure 5.17 Molecular weight distributions of sPS in SNTR, no chain transfer constants change; experimental results, $M_n = 275,000$ g/mol, $M_w = 928,000$ g/mol (symbol); simulation result, $M_n = 41,400$ g/mol, $M_w = 156,000$ g/mol (line).

Since the monomer concentration nonuniformity has negligible effect on the polymer MWD, we need to consider other factors that can affect the MWD. The molecular weight enhancement observed in ethylene polymerizations with the mesoporous silicas were attributed to the steric inhibition effect on chain transfer reactions [143, 146]. However, the SNTRs used in our study have pore diameters that are much larger than mesoporous silicas used by other workers for ethylene polymerization. From the SEM images presented in Figure 5.5, 5.7, and 5.8, we can postulate that the presence of sPS nanofibrils near the active catalytic centers may inhibit the β -hydrogen elimination reaction. It is certainly possible because for the beta hydrogen elimination reaction to occur, the growing polymer chain end must

coordinate properly but the presence of the solid phase (nanofibrils) in the proximity of the active sites can greatly reduce the mobility of the polymer chains.

To reflect the confinement effect of SNTR pores on the polymer molecular weights, chain transfer rate constants, $k_{t\beta,s}$ and $k_{tM,s}$, were optimized using the non-linear least squares regression technique (*nlinfit* function in MATLAB[®]). Optimized values of $k_{t\beta,s}$ and $k_{tM,s}$ are 0.065 times smaller than those in Table 5.3. Figure 5.18 shows the MWD curves of sPS polymerized in commercial SNTR pores with 0.065 times smaller chain transfer rate constants. Overall shape and weight average molecular weight were well matched with experimental data.

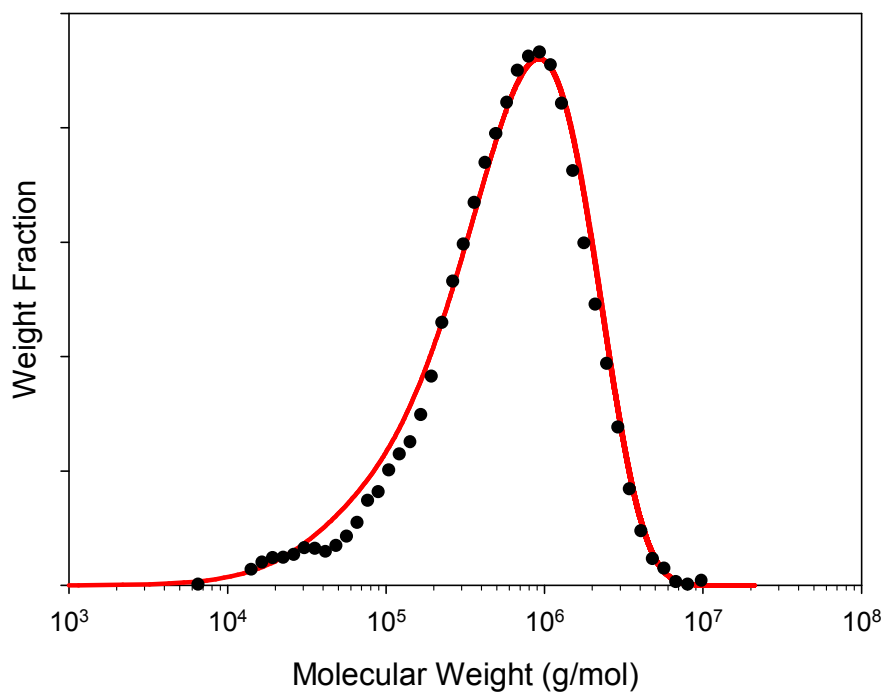


Figure 5.18 Molecular weight distributions of sPS in SNTR, chain transfer change, $k_t' = 0.065k_t$; experimental results, $M_n = 275,000$ g/mol, $M_w = 928,000$ g/mol (symbol); simulation result, $M_n = 209,000$ g/mol, $M_w = 908,000$ g/mol (line).

The MWD curves of sPS polymerized in homemade SNTRs with optimized chain transfer rate constants were shown in Figure 5.19 and compared with commercial SNTR pores. Because of small change of monomer concentration due to short pore length, polydispersity of sPS synthesized in homemade SNTRs is very small ($PDI = 2.10$). However, molecular weight of polymer with homemade SNTRs is slightly higher than that with commercial SNTRs because average monomer concentration in a homemade pore is higher than that in a commercial pore. Simulation results were listed in Table 5.5.

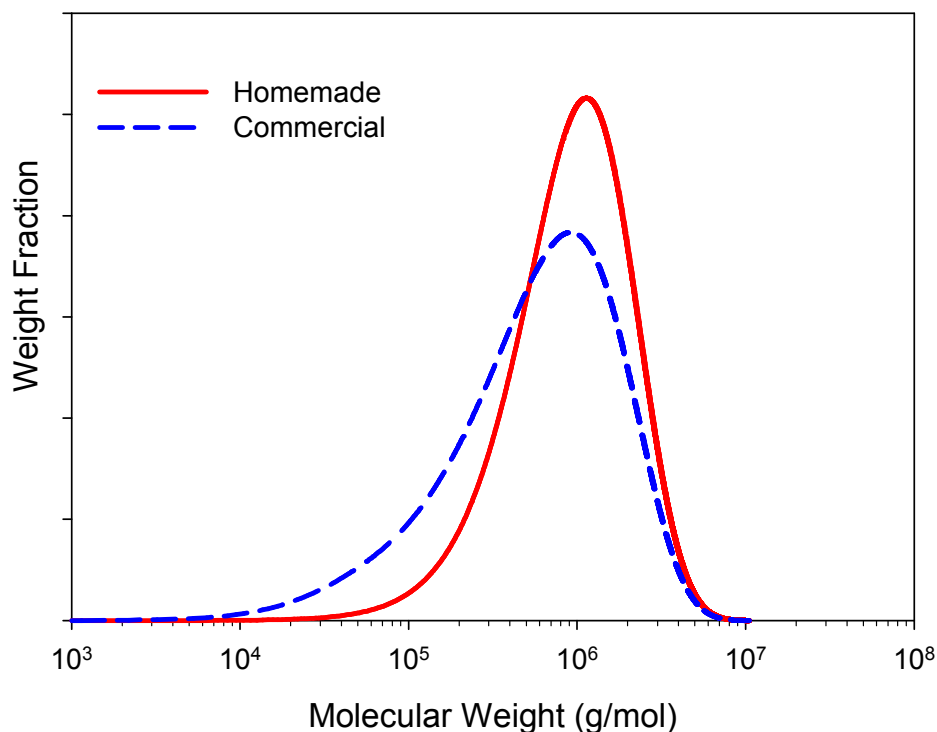


Figure 5.19 Molecular weight distributions of sPS in SNTRs, chain transfer change, $k_t' = 0.065k_t$; homemade, $M_n = 209,000$ g/mol, $M_w = 908,000$ g/mol (solid line); commercial, $M_n = 566,000$ g/mol, $M_w = 1,189,000$ g/mol (dashed line).

Table 5.5 MWD calculation with chain transfer constant rate change

	Commercial	Homemade
Mn, g/mol	209,000	566,000
Mw, g/mol	908,000	1,189,000
PDI	4.34	2.10

5.4 Conclusions

In this chapter, the synthesis of syndiotactic polystyrene in silica nanotube reactors has been presented. This work is the first to show that AAO films can be a framework for the catalytic nanotube reactor for syndiospecific polymerization of styrene. It has been found in this work that sPS nanofibrils synthesized in the nanopores extrude out of the SNTR. We propose that the growth of the polymer nanofibrils can be modeled by a three-stage mechanism: (i) the formation of very thin nanofibrils (less than 10 nm in diameter), (ii) the formation of a larger, rope-like cord with 30 – 50 nm diameter, (iii) the formation of larger nanofibril that is fit in a nanopore. It has also been shown that the SNTRs can be a new see-through tool for the visual observation of polymer chain growth in the silica nanotube reactors. The X-ray diffraction and high-temperature GPC analyses indicate the sPS produced in the SNTR is a δ -form crystal polymer that has an ultrahigh molecular weight with a large fraction of 2,000,000 - 5,000,000 g/mol polymer. It is likely that chain transfer reactions were greatly hindered by the confinement effect of the SNTR. In addition,

the ultrahigh molecular weight sPS has a much higher crystalline melting point than those polymerized over silica-supported metallocene catalysts.

A simplified diffusion-reaction model has been developed to predict the polymerization rate and polymer molecular weight distribution. The steady state monomer concentration profiles are quickly established and the model simulations indicate that the effect of monomer concentration nonuniformity on the MWD is minimal. The two-site catalytic mechanism was also applied to the SNTR modeling. The model simulations show that to match the experimentally observed ultrahigh molecular weight, the effective chain transfer rate constant (i.e., beta hydrogen elimination) must be 0.065 times smaller than the value for the regular silica-supported catalyst system. It is thought that such reduced chain transfer reaction as observed in our model simulations might have been caused by the presence of highly crystalline sPS in the proximity of the active sites. But further study will be required to better understand the steric hindrance effect on the chain transfer reaction and to quantify the molecular weight enhancement effect.

Chapter 6: Summary

This study can be divided into the following four parts: 1) Kinetic analysis of syndiospecific polymerization of styrene in homogeneous and heterogeneous catalysts; 2) Morphological study on the sPS particles produced over homogeneous and heterogeneous catalysts; and 3) Morphology and modeling of sPS synthesized in silica nanotube reactors (SNTRs).

In the part of kinetic analysis of sPS polymerization in homogeneous and heterogeneous catalysts, theoretical modeling analysis of the syndiospecific polymerization of styrene over homogenous and silica-supported $\text{Cp}^*\text{Ti}(\text{OCH}_3)_3/\text{MAO}$ catalyst was accomplished. It has been observed that sPS polymerization rate is nonlinearly dependent on the bulk phase monomer concentration. The monomer partition effect was incorporated into kinetic models. For the silica-supported metallocene catalyst system, molecular weight distribution modeling was also performed by employing a two-site kinetic model. The two site model provided improved predictions of the molecular weight distribution, clearly suggesting the presence of multiple active sites in the silica-supported metallocene catalyst.

In the part of the morphological study, we observed the nanofibrillar morphology of sPS particles in homogeneous and silica-supported metallocene catalyst system. Our experimental data indicates that the dimension of sPS nanofibrils

(30-50 nm). The XRD analysis shows that the sPS obtained in a liquid slurry polymerization experiments is of the co-crystal. In silica-supported metallocene catalyst system, we observed that fragmentation of silica particles has occurred during the polymerization by the SEM and EDX analysis. It is believed that the nanofibrillar structure formation is closely related with polymer crystallization. Based on the observations in our study, we have proposed a mechanism for the growth of sPS particles.

In the last part, morphology and modeling of sPS synthesized in silica nanotube reactor (SNTR), we successfully synthesized sPS in a metallocene catalyst-anchored silica nanotube reactor. Throughout the morphological study of sPS in a pore, we proposed the sPS fibrillar formation mechanism from the catalytic active site in detail. By using SNTR, we obtained sPS δ -form crystal polymer that has an ultrahigh molecular weight. MWD modeling of sPS synthesized in a confined nanopore was tried. It seems that steric hindrance by confined geometry affects the retardation of the chain transfer reaction.

Bibliography

1. Po', R.; Cardi, N. "Synthesis of syndiotactic polystyrene: Reaction mechanisms and catalysis." *Progress in Polymer Science* **1996**, 21, (1), 47-88.
2. Scheirs, J.; Priddy, D. B., *Modern styrenic polymers: polystyrenes and styrenic copolymers*. In John Wiley & Sons, Ltd.: Hoboken, NJ, 2003; p xxxi, 757 p.
3. Schellenberg, J.; Leder, H. J. "Syndiotactic polystyrene: Process and applications." *Advances in Polymer Technology* **2006**, 25, (3), 141-151.
4. Malanga, M. "Syndiotactic polystyrene materials." *Advanced Materials* **2000**, 12, (23), 1869-1872.
5. Hermanson, N. J.; Wessel, T. E., Syndiotactic polystyrene: a new polymer for high-performance medical applications. *Medical plastics and biomaterials* 1998.
6. Ishihara, N.; Seimiya, T.; Kuramoto, M.; Uoi, M. "Crystalline syndiotactic polystyrene." *Macromolecules* **1986**, 19, (9), 2464-2465.
7. Schellenberg, J.; Tomotsu, N. "Syndiotactic polystyrene catalysts and polymerization." *Progress in Polymer Science* **2002**, 27, (9), 1925-1982.
8. Newman, T. H.; Malanga, M. T. "Syndiotactic polystyrene polymerization results using a titanium(III) complex, $\text{Cp}^*\text{Ti}(\text{OMe})_2$ and implications to the mechanism of polymerization." *Journal of Macromolecular Science-Pure and Applied Chemistry* **1997**, A34, (10), 1921-1927.
9. Pellecchia, C.; Grassi, A. "Syndiotactic-specific polymerization of styrene: catalyst structure and polymerization mechanism." *Topics in Catalysis* **1999**, 7, (1-4), 125-132.
10. Zambelli, A.; Longo, P.; Pellecchia, C.; Grassi, A. "Beta-hydrogen abstraction and regiospecific insertion in syndiotactic polymerization of styrene." *Macromolecules* **1987**, 20, (8), 2035-2037.
11. Duncalf, D. J.; Wade, H. J.; Waterson, C.; Derrick, P. J.; Haddleton, D. M.; McCamley, A. "Synthesis and mechanism of formation of syndiotactic polystyrene using a (tert-butylcyclopentadienyl)titanium complex." *Macromolecules* **1996**, 29, (20), 6399-6403.
12. Grassi, A.; Lamberti, C.; Zambelli, A.; Mingozzi, I. "Syndiospecific styrene polymerization promoted by half-titanocene catalysts: A kinetic investigation providing a closer insight to the active species." *Macromolecules* **1997**, 30, (7), 1884-1889.

13. Huang, Q. G.; Chen, L. G.; Lin, S. G.; Wu, Q.; Zhu, F. M.; Shiyan; Fu, Z. F.; Yang, W. T. "Syndiospecific polymerization of styrene catalyzed by half-titanocene catalysts." *Polymer* **2006**, 47, (2), 767-773.
14. Xu, G. X.; Cheng, D. L. "Syndiospecific polymerization of styrene with half-sandwich titanocene catalysts. Influence of ligand pattern on polymerization behavior." *Macromolecules* **2000**, 33, (8), 2825-2831.
15. Kawabe, M.; Murata, M. "Solvent effect on beta-hydride elimination reaction in syndiospecific styrene polymerization with cyclopentadienyltitanium trichloride (CpTiCl₃)/methylaluminoxane (MAO) catalytic system." *Macromolecular Chemistry and Physics* **2001**, 202, (11), 2440-2446.
16. Qian, Y. L.; Zhang, H.; Zhou, J. X.; Zhao, W.; Sun, X. Q.; Huang, J. L. "Synthesis and polymerization behavior of various substituted half-sandwich titanium complexes Cp⁺TiCl₂(OR⁺) as catalysts for syndiotactic polystyrene." *Journal of Molecular Catalysis a-Chemical* **2004**, 208, (1-2), 45-54.
17. Ishihara, N.; Kuramoto, M.; Uoi, M. "Stereospecific polymerization of styrene giving the syndiotactic polymer." *Macromolecules* **1988**, 21, (12), 3356-3360.
18. Huang, Y. H.; Wang, W. J.; Zhu, S.; Rempel, G. L. "ESR study on styrene polymerization with CpTiCl₃/MMAO: Effect of monomer addition on catalyst activity." *Journal of Polymer Science Part a-Polymer Chemistry* **1999**, 37, (16), 3385-3390.
19. Hlatky, G. G. "Heterogeneous single-site catalysts for olefin polymerization." *Chemical Reviews* **2000**, 100, (4), 1347-1376.
20. Huang, J. F.; Rempel, G. L. "A kinetic study of propylene polymerization using Cp₂ZrCl/methylaluminoxane catalysts." *Polymer Reaction Engineering* **1997**, 5, (3), 125-139.
21. Kaminsky, W. "New polymers by metallocene catalysis." *Macromolecular Chemistry and Physics* **1996**, 197, (12), 3907-3945.
22. Hamielec, A. E.; Soares, J. B. P. "Polymerization reaction engineering - Metallocene catalysts." *Progress in Polymer Science* **1996**, 21, (4), 651-706.
23. Guerra, G.; Vitagliano, V. M.; Derosa, C.; Petraccone, V.; Corradini, P. "Polymorphism in Melt Crystallized Syndiotactic Polystyrene Samples." *Macromolecules* **1990**, 23, (5), 1539-1544.
24. Kobayashi, M.; Nakaoki, T.; Ishihara, N. "Molecular-conformation in glasses and gels of syndiotactic and isotactic polystyrenes." *Macromolecules* **1990**, 23, (1), 78-83.

25. Bu, W. S.; Li, Y. Y.; He, J. S.; Zeng, J. J. "An interpretation of the formation of alpha- and beta-form crystals in bulk syndiotactic polystyrene." *Macromolecules* **1999**, 32, (21), 7224-7225.
26. De Rosa, C.; Rapacciuolo, M.; Guerra, G.; Petraccone, V.; Corradini, P. "On the crystal-structure of the orthorhombic form of syndiotactic polystyrene." *Polymer* **1992**, 33, (7), 1423-1428.
27. Rastogi, S.; Goossens, J. G. P.; Lemstra, P. J. "An in situ SAXS/WAXS/Raman spectroscopy study on the phase behavior of syndiotactic polystyrene (sPS)/solvent systems: Compound formation and solvent (dis)ordering." *Macromolecules* **1998**, 31, (9), 2983-2998.
28. Mohri, S.; Rani, D. A.; Yamamoto, Y.; Tsujita, Y.; Yoshimizu, H. "Structure and properties of the mesophase of syndiotactic polystyrene - III. Selective sorption of the mesophase of syndiotactic polystyrene." *Journal of Polymer Science Part B-Polymer Physics* **2004**, 42, (2), 238-245.
29. Rani, D. A.; Yamamoto, Y.; Mohri, S.; Sivakumar, M.; Tsujita, Y.; Yoshimizu, H. "Structure and properties of the mesophase of syndiotactic polystyrene. II. Effect of stepwise extraction on the preparation of the mesophase." *Journal of Polymer Science Part B-Polymer Physics* **2003**, 41, (3), 269-273.
30. Rani, D. A.; Yamamoto, Y.; Saito, A.; Sivakumar, M.; Tsujita, Y.; Yoshimizu, H.; Kinoshita, T. "Structure and properties of the mesophase of syndiotactic polystyrene. I. Effect of casting conditions on the preparation of the mesophase." *Journal of Polymer Science Part B-Polymer Physics* **2002**, 40, (6), 530-536.
31. Uda, Y.; Kaneko, F.; Kawaguchi, T. "Guest exchange with n-alkanes and host-guest interactions in the clathrate phase of syndiotactic polystyrene." *Macromolecules* **2005**, 38, (8), 3320-3326.
32. Mahesh, K. P.; Sivakumar, M.; Yamamoto, Y.; Tsujita, Y.; Yoshimizu, H.; Okamoto, S. "Structure and properties of the mesophase of syndiotactic polystyrene. VIII. Solvent sorption behavior of syndiotactic polystyrene/p-chlorotoluene mesophase membranes." *Journal of Polymer Science Part B-Polymer Physics* **2004**, 42, (18), 3439-3446.
33. De Rosa, C.; Guerra, G.; Petraccone, V.; Pirozzi, B. "Crystal structure of the emptied clathrate form (δ_e form) of syndiotactic polystyrene." *Macromolecules* **1997**, 30, (14), 4147-4152.
34. Trezza, E.; Grassi, A. "Dynamics of aromatic molecules clathrated in crystalline syndiotactic polystyrene: A solid state H-2 NMR investigation of the host/guest complexes." *Macromolecular Rapid Communications* **2002**, 23, (4), 260-263.

35. Evans, A. M.; Kellar, E. J. C.; Knowles, J.; Galiotis, C.; Carriere, C. J.; Andrews, E. H. "The structure and morphology of syndiotactic polystyrene injection molded coupons." *Polymer Engineering and Science* **1997**, 37, (1), 153-165.
36. Tamai, Y.; Fukuda, M. "Nanoscale molecular cavity in crystalline polymer membranes studied by molecular dynamics simulation." *Polymer* **2003**, 44, (11), 3279-3289.
37. Tamai, Y.; Fukuda, M. "Thermally induced phase transition of crystalline syndiotactic polystyrene studied by molecular dynamics simulation." *Macromolecular Rapid Communications* **2002**, 23, (15), 892-895.
38. Daniel, C.; Dammer, C.; Guenet, J. M. "On the definition of thermoreversible gels - the case of syndiotactic polystyrene." *Polymer* **1994**, 35, (19), 4243-4246.
39. Itagaki, H.; Mochizuki, J. "Size and distribution of free volume in thermoreversible gels of syndiotactic polystyrene." *Macromolecules* **2005**, 38, (23), 9625-9630.
40. Malik, S.; Rochas, C.; Guenet, J. M. "Syndiotactic polystyrene/naphthalene intercalates: Preparing thermoreversible fibrillar gels from a solid solvent." *Macromolecules* **2005**, 38, (11), 4888-4893.
41. Daniel, C.; Deluca, M. D.; Guenet, J. M.; Brulet, A.; Menelle, A. "Thermoreversible gelation of syndiotactic polystyrene in benzene." *Polymer* **1996**, 37, (7), 1273-1280.
42. Daniel, C.; Menelle, A.; Brulet, A.; Guenet, J. M. "Thermoreversible gelation of syndiotactic polystyrene in toluene and chloroform." *Polymer* **1997**, 38, (16), 4193-4199.
43. Beaudoin, D. A. Syndiotactic vinylaromatic polymerization using multiple reactors in series. US 6,242,542 B1, Jun. 5, 2001, 2001.
44. Yamamoto, K.; Ishikawa, K.; Imabayashi, H.; Izumi, T. Process for producing styrene-based polymers. U.S. 5,254,647, 1993.
45. Fan, R.; Cao, K.; Li, B. F.; Fan, H.; Li, B. G. "Morphology and crystallinity of nascent sPS in bulk polymerization with homogeneous metallocene catalyst." *European Polymer Journal* **2001**, 37, (11), 2335-2338.
46. Fan, R.; Li, B. G.; Cao, K.; Zhou, W. L.; Shen, Z. G.; Ye, M. "Full-range kinetic study on bulk syndiotactic polymerization of styrene with homogeneous metallocene catalysis." *Journal of Applied Polymer Science* **2002**, 85, (13), 2635-2643.
47. Tomotsu, N.; Ishihara, N.; Newman, T. H.; Malanga, M. T. "Syndiospecific polymerization of styrene." *Journal of Molecular Catalysis a-Chemical* **1998**, 128, (1-3), 167-190.

48. Oliva, L.; Pellecchia, C.; Cinquina, P.; Zambelli, A. "Preliminary Kinetic Investigation on Syndiotactic Polymerization of Styrene." *Macromolecules* **1989**, 22, (4), 1642-1645.
49. Chien, J. C. W.; Salajka, Z. "Syndiospecific polymerization of styrene. 1. Tetrabenzyl titanium methylaluminoxane catalyst." *Journal of Polymer Science Part a-Polymer Chemistry* **1991**, 29, (9), 1243-1251.
50. Chien, J. C. W.; Salajka, Z. "Syndiospecific polymerization of styrene. 2. Monocyclopentadienyltributoxy titanium methylaluminoxane catalyst." *Journal of Polymer Science Part a-Polymer Chemistry* **1991**, 29, (9), 1253-1263.
51. Choi, K. Y.; Chung, J. S.; Woo, B. G.; Hong, M. H. "Kinetics of slurry phase polymerization of styrene to syndiotactic polystyrene with pentamethyl cyclopentadienyl titanium trimethoxide and methyl aluminoxane. I. Reaction rate analysis." *Journal of Applied Polymer Science* **2003**, 88, (8), 2132-2137.
52. Lee, H. W.; Chung, J. S.; Choi, K. Y. "Physical transitions and nascent morphology of syndiotactic polystyrene in slurry polymerization with embedded Cp*Ti(OMe)₃/methyl aluminoxane catalyst." *Polymer* **2005**, 46, (14), 5032-5039.
53. Zambelli, A.; Oliva, L.; Pellecchia, C. "Soluble catalysts for syndiotactic polymerization of styrene." *Macromolecules* **1989**, 22, (5), 2129-2130.
54. Campbell, R. E.; Newman, T. H.; Malanga, M. T. "MAO based catalysts for syndiotactic polystyrene (sPS)." *Macromolecular Symposia* **1995**, 97, 151-160.
55. Longo, P.; Proto, A.; Oliva, L. "Zirconium catalysts for the syndiotactic polymerization of styrene." *Macromolecular Rapid Communications* **1994**, 15, (2), 151-154.
56. Xu, G. X.; Ruckenstein, E. "Syndiospecific polymerization of styrene using fluorinated indenyltitanium complexes." *Journal of Polymer Science Part a-Polymer Chemistry* **1999**, 37, (14), 2481-2488.
57. Schellenberg, J. "The syndiospecific polymerization of styrene in the presence of fluorine-containing half-sandwich metallocenes." *Journal of Polymer Science Part a-Polymer Chemistry* **2000**, 38, (13), 2428-2439.
58. Liu, J. F.; Ma, H. Y.; Huang, J. L.; Qian, Y. L. "Syndiotactic polymerization of styrene with CpTiCl₂(OR)/MAO system." *European Polymer Journal* **2000**, 36, (9), 2055-2058.
59. Tomotsu, N.; Ishihara, N. "Recent development of catalysts for syndiospecific polymerization of styrene." *Science and Technology in Catalysis 1998* **1999**, 121, 269-276.

60. Yim, J. H.; Chu, K. J.; Choi, K. W.; Ihm, S. K. "Syndiospecific polymerization of styrene over silica supported CpTiCl₃ catalysts." *European Polymer Journal* **1996**, 32, (12), 1381-1385.
61. Xu, J. T.; Zhao, J.; Fan, Z. Q.; Feng, L. X. "ESR study on SiO₂-supported half-titanocene catalyst for syndiospecific polymerization of styrene." *Macromolecular Rapid Communications* **1997**, 18, (9), 875-882.
62. Chien, J. C. W.; Salajka, Z.; Dong, S. "Syndiospecific polymerization of styrene. 3. catalyst Structure." *Macromolecules* **1992**, 25, (12), 3199-3203.
63. Burke, J., Solubility parameters: Theory and Application. In *The Book and Paper Group ANNUAL*, Jensen, C. W., Ed. The American Institute for Conservation: Washington, D.C., 1984; Vol. 3.
64. Hutchinson, R. A.; Ray, W. H. "Polymerization of Olefins through Heterogeneous Catalysis .8. Monomer Sorption Effects." *Journal of Applied Polymer Science* **1990**, 41, (1-2), 51-81.
65. Xie, T. Y.; Hamielec, A. E.; Wood, P. E.; Woods, D. R. "Experimental investigation of vinyl-chloride polymerization at high conversion - molecular-weight development." *Polymer* **1991**, 32, (6), 1098-1111.
66. Xie, T. Y.; Hamielec, A. E.; Wood, P. E.; Woods, D. R. "Experimental investigation of vinyl-chloride polymerization at high conversion - mechanism, kinetics and modeling." *Polymer* **1991**, 32, (3), 537-557.
67. Patel, C. B.; Grandin, R. E.; Gupta, R.; Phillips, E. M.; Reynolds, C. E.; Chan, R. K. S. "Partition-coefficients of vinyl-chloride between PVC-liquid-vapor phases." *Polymer Journal* **1979**, 11, (1), 43-51.
68. Chung, J. S.; Woo, B. G.; Choi, K. Y. "Syndiospecific polymerization of styrene with embedded metallocene catalysts." *Macromolecular Symposia* **2004**, 206, 375-382.
69. Kaminsky, W.; Winkelbach, H. "Influence of supported metallocene catalysts on polymer tacticity." *Topics in Catalysis* **1999**, 7, (1-4), 61-67.
70. Kaminsky, W.; Arrowsmith, D.; Strubel, C. "Polymerization of styrene with supported half-sandwich complexes." *Journal of Polymer Science Part a-Polymer Chemistry* **1999**, 37, (15), 2959-2968.
71. Niegisch, W. D.; Crisafulli, S. T.; Nagel, T. S.; Wagner, B. E. "Characterization techniques for the study of silica fragmentation in the early stages of ethylene polymerization." *Macromolecules* **1992**, 25, (15), 3910-3916.
72. Flörke, O. W., *Silica*. In Ullmann's encyclopedia of industrial chemistry, Wiley-VCH Verlag GmbH & Co. KGaA: 2005; Vol. A23, p 1-85.

73. Bergstra, M. F.; Weickert, G. "Ethylene polymerization kinetics with a heterogeneous metallocene catalyst - Comparison of gas and slurry phases." *Macromolecular Materials and Engineering* **2005**, 290, (6), 610-620.
74. Barton, A. F. M., *CRC handbook of solubility parameters and other cohesion parameters*. 2nd ed.; CRC Press: Boca Raton, 1991; p 739 p.
75. Young, R. J.; Lovell, P. A., *Introduction to polymers*. 2nd ed.; Chapman & Hall: London ; New York, 1991; p x, 443 p.
76. Odian, G., *Principles of polymerization*. 4th ed.; Wiley: New York ; Chichester, 2004; p xxiv, 812 p.
77. Novokshonova, L.; Kovaleva, N.; Meshkova, I.; Ushakova, T.; Krashennnikov, V.; Ladygina, T.; Leipunskii, I.; Zhigach, A.; Kuskov, M. "Heterogenization of metalorganic catalysts of olefin polymerization and evaluation of active site non-uniformity." *Macromolecular Symposia* **2004**, 213, 147-155.
78. Frauenrath, H.; Keul, H.; Hocker, H. "Deviation from single-site behavior in zirconocene/MAO catalyst systems, 1 Influence of monomer, catalyst, and cocatalyst concentration." *Macromolecular Chemistry and Physics* **2001**, 202, (18), 3543-3550.
79. Frauenrath, H.; Keul, H.; Hocker, H. "Deviation from single-site behavior in zirconocene/MAO catalyst systems, 2 Influence of polymerization temperature." *Macromolecular Chemistry and Physics* **2001**, 202, (18), 3551-3559.
80. Kou, B.; McAuley, K. B.; Hsu, C. C.; Bacon, D. W.; Yao, K. Z. "Mathematical model and parameter estimation for gas-phase ethylene homopolymerization with supported metallocene catalyst." *Industrial & Engineering Chemistry Research* **2005**, 44, (8), 2428-2442.
81. Ciardelli, F.; Altomare, A.; Michelotti, M. "From homogeneous to supported metallocene catalysts." *Catalysis Today* **1998**, 41, (1-3), 149-157.
82. van Grieken, R.; Calleja, G.; Serrano, D.; Martos, C.; Melgares, A.; Suarez, I. "The role of the hydroxyl groups on the silica surface when supporting metallocene/MAO catalysts." *Polymer Reaction Engineering* **2003**, 11, (1), 17-32.
83. Haukka, S.; Lakomaa, E. L.; Root, A. "An Ir and Nmr-Study of the Chemisorption of $TiCl_4$ on Silica." *Journal of Physical Chemistry* **1993**, 97, (19), 5085-5094.
84. Zhuravlev, L. T. "The surface chemistry of amorphous silica. Zhuravlev model." *Colloids and Surfaces a-Physicochemical and Engineering Aspects* **2000**, 173, (1-3), 1-38.

85. Juan, A.; Damiani, D.; Pistonesi, C.; Garcia, A. "The electronic structure and bonding of MAO on the SiO₂ (111) hydrated surface." *Macromolecular Theory and Simulations* **2001**, 10, (5), 485-490.
86. van Grieken, R.; Carrero, A.; Suarez, I.; Paredes, B. "Ethylene polymerization over supported MAO/(nBuCp)₂ZrCl₂ catalysts: Influence of support properties." *European Polymer Journal* **2007**, 43, (4), 1267-1277.
87. Soares, J. B. P.; Kim, J. D.; Rempel, G. L. "Analysis and control of the molecular weight and chemical composition distributions of polyolefins made with metallocene and Ziegler-Natta catalysts." *Industrial & Engineering Chemistry Research* **1997**, 36, (4), 1144-1150.
88. Soares, J. B. P.; Hamielec, A. E. "Deconvolution of chain length distributions of linear polymers made by multiple-site type catalysts." *Polymer* **1995**, 36, (11), 2257-2263.
89. Tannous, K.; Soares, J. B. P. "Gas-phase polymerization of ethylene using supported metallocene catalysts: Study of polymerization conditions." *Macromolecular Chemistry and Physics* **2002**, 203, (13), 1895-1905.
90. Ray, B.; Elhasri, S.; Thierry, A.; Marie, P.; Guenet, J. M. "Solvent-induced crystallization of syndiotactic polystyrene: Thermodynamics and morphology." *Macromolecules* **2002**, 35, (26), 9730-9736.
91. Daniel, C.; Alfano, D.; Venditto, V.; Cardea, S.; Reverchon, E.; Larobina, D.; Mensitieri, G.; Guerra, G. "Aerogels with a microporous crystalline host phase." *Advanced Materials* **2005**, 17, (12), 1515-1518.
92. Malik, S.; Rochas, C.; Deme, B.; Guenet, J. M. "Thermoreversible gelation of syndiotactic polystyrene in naphthalene." *Macromolecular Symposia* **2005**, 222, 73-79.
93. Malik, S.; Rochas, C.; Schmutz, M.; Guenet, J. M. "Syndiotactic polystyrene intercalates from naphthalene derivatives." *Macromolecules* **2005**, 38, (14), 6024-6030.
94. Daniel, C.; Avallone, A.; Guerra, G. "Syndiotactic polystyrene physical gels: Guest influence on structural order in molecular complex domains and gel transparency." *Macromolecules* **2006**, 39, (22), 7578-7582.
95. Guenet, J. M. "Microfibrillar networks: Polymer thermoreversible gels vs organogels." *Macromolecular Symposia* **2006**, 241, 45-50.
96. Malik, S.; Rochas, C.; Guenet, J. M. "Thermodynamic and structural investigations on the different forms of syndiotactic polystyrene intercalates." *Macromolecules* **2006**, 39, (3), 1000-1007.

97. Malik, S.; Roizard, D.; Guenet, J. M. "Multiporous material from fibrillar syndiotactic polystyrene intercalates." *Macromolecules* **2006**, 39, (18), 5957-5959.
98. Daniel, C.; Sannino, D.; Guerra, G. "Syndiotactic polystyrene aerogels: Adsorption in amorphous pores and absorption in crystalline nanocavities." *Chemistry of Materials* **2008**, 20, (2), 577-582.
99. Guerra, G.; Milano, G.; Venditto, V.; Musto, P.; De Rosa, C.; Cavallo, L. "Thermoplastic molecular sieves." *Chemistry of Materials* **2000**, 12, (2), 363-368.
100. Giordano, M.; Russo, M.; Cusano, A.; Cutolo, A.; Mensitieri, G.; Nicolais, L. "Optical sensor based on ultrathin films of delta-form syndiotactic polystyrene for fast and high resolution detection of chloroform." *Applied Physics Letters* **2004**, 85, (22), 5349-5351.
101. Giordano, M.; Russo, A.; Cusano, A.; Mensitieri, G. "An high sensitivity optical sensor for chloroform vapours detection based on nanometric film of delta-form syndiotactic polystyrene." *Sensors and Actuators B-Chemical* **2005**, 107, (1), 140-147.
102. Giordano, M.; Russo, M.; Cusano, A.; Mensitieri, G.; Guerra, G. "Syndiotactic polystyrene thin film as sensitive layer for an optoelectronic chemical sensing device." *Sensors and Actuators B-Chemical* **2005**, 109, (2), 177-184.
103. Annunziata, L.; Albunia, A. R.; Venditto, V.; Mensitieri, G.; Guerra, G. "Polymer/gas clathrates for gas storage and controlled release." *Macromolecules* **2006**, 39, (26), 9166-9170.
104. Ferrero, M. A.; Chiovetta, M. G. "Catalyst Fragmentation during Propylene Polymerization .1. The Effects of Grain-Size and Structure." *Polymer Engineering and Science* **1987**, 27, (19), 1436-1447.
105. Kakugo, M.; Sadatoshi, H.; Sakai, J.; Yokoyama, M. "Growth of polypropylene particles in heterogeneous Ziegler-Natta polymerization." *Macromolecules* **1989**, 22, (7), 3172-3177.
106. Estenoz, D. A.; Chiovetta, M. G. "A structural model for the catalytic polymerization of ethylene using chromium catalysts .1. Description and solution." *Polymer Engineering and Science* **1996**, 36, (17), 2208-2228.
107. Estenoz, D. A.; Chiovetta, M. G. "Olefin polymerization using supported metallocene catalysts: Process representation scheme and mathematical model." *Journal of Applied Polymer Science* **2001**, 81, (2), 285-311.
108. Debling, J. A.; Ray, W. H. "Heat and mass transfer effects in multistage polymerization processes - Impact polypropylene." *Industrial & Engineering Chemistry Research* **1995**, 34, (10), 3466-3480.

109. Hutchinson, R. A.; Chen, C. M.; Ray, W. H. "Polymerization of olefins through heterogeneous catalysis.10. Modeling of particle growth and morphology." *Journal of Applied Polymer Science* **1992**, 44, (8), 1389-1414.
110. Fink, G.; Steinmetz, B.; Zechlin, J.; Przybyla, C.; Tesche, B. "Propene polymerization with silica-supported metallocene/MAO catalysts." *Chemical Reviews* **2000**, 100, (4), 1377-1390.
111. Goretzki, R.; Fink, G.; Tesche, B.; Steinmetz, B.; Rieger, R.; Uzick, W. "Unusual ethylene polymerization results with metallocene catalysts supported on silica." *Journal of Polymer Science Part a-Polymer Chemistry* **1999**, 37, (5), 677-682.
112. Jang, Y. J.; Naundorf, C.; Klapper, M.; Mullen, K. "Study of the fragmentation process of different supports for metallocenes by laser scanning confocal fluorescence microscopy (LSCFM)." *Macromolecular Chemistry and Physics* **2005**, 206, (20), 2027-2037.
113. Sun, Y. S.; Woo, E. M. "Mechanisms of reorganization of lamellae in syndiotactic polystyrene." *Journal of Polymer Science Part B-Polymer Physics* **2000**, 38, (24), 3210-3221.
114. Sun, Y. S.; Woo, E. M. "Morphology and crystal structure of cold-crystallized syndiotactic polystyrene." *Polymer* **2001**, 42, (5), 2241-2245.
115. Woo, E. M.; Sun, Y. S.; Yang, C. P. "Polymorphism, thermal behavior, and crystal stability in syndiotactic polystyrene vs. its miscible blends." *Progress in Polymer Science* **2001**, 26, (6), 945-983.
116. Wang, C.; Lin, C. C.; Chu, C. P. "Crystallization and morphological features of syndiotactic polystyrene induced from glassy state." *Polymer* **2005**, 46, (26), 12595-12606.
117. Larobina, D.; Sanguigno, L.; Venditto, V.; Guerra, G.; Mensitieri, G. "Gas sorption and transport in syndiotactic polystyrene with nanoporous crystalline phase." *Polymer* **2004**, 45, (2), 429-436.
118. Milano, G.; Venditto, V.; Guerra, G.; Cavallo, L.; Ciambelli, P.; Sannino, D. "Shape and volume of cavities in thermoplastic molecular sieves based on syndiotactic polystyrene." *Chemistry of Materials* **2001**, 13, (5), 1506-1511.
119. Rizzo, P.; Lamberti, M.; Alburnia, A. R.; de Ballesteros, O. R.; Guerra, G. "Crystalline orientation in syndiotactic polystyrene cast films." *Macromolecules* **2002**, 35, (15), 5854-5860.
120. Pasztor, A. J.; Landes, B. G.; Karjala, P. J. "Thermal-Properties of Syndiotactic Polystyrene." *Thermochimica Acta* **1991**, 177, 187-195.

121. De Rosa, C.; Rizzo, P.; de Ballesteros, O. R.; Petraccone, V.; Guerra, G. "Crystal structure of the clathrate delta form of syndiotactic polystyrene containing 1,2-dichloroethane." *Polymer* **1999**, 40, (8), 2103-2110.
122. Daniel, C.; Guerra, G.; Musto, P. "Clathrate phase in syndiotactic polystyrene gels." *Macromolecules* **2002**, 35, (6), 2243-2251.
123. Musto, P.; Mensitieri, G.; Cotugno, S.; Guerra, G.; Venditto, V. "Probing by time-resolved FTIR spectroscopy mass transport, molecular interactions, and conformational ordering in the system chloroform-syndiotactic polystyrene." *Macromolecules* **2002**, 35, (6), 2296-2304.
124. Albunia, A. R.; Musto, P.; Guerra, G. "FTIR spectra of pure helical crystalline phases of syndiotactic polystyrene." *Polymer* **2006**, 47, (1), 234-242.
125. Reverchon, E.; Guerra, G.; Venditto, V. "Regeneration of nanoporous crystalline syndiotactic polystyrene by supercritical CO₂." *Journal of Applied Polymer Science* **1999**, 74, (8), 2077-2082.
126. Knoke, S.; Ferrari, D.; Tesche, B.; Fink, G. "Microkinetic videomicroscopic analysis of olefin polymerization with a supported metallocene catalyst." *Angewandte Chemie-International Edition* **2003**, 42, (41), 5090-5093.
127. Wagner, B. E.; Niegisch, W. D. *Polym Mater Sci Eng* **1991**, 64, 139-141.
128. Kim, S. H.; Somorjai, G. A. "Surface science of single-site heterogeneous olefin polymerization catalysts." *Proceedings of the National Academy of Sciences of the United States of America* **2006**, 103, (42), 15289-15294.
129. Tashiro, K.; Yoshioka, A. "Molecular mechanism of solvent-induced crystallization of syndiotactic polystyrene glass. 2. Detection of enhanced motion of the amorphous chains in the induction period of crystallization." *Macromolecules* **2002**, 35, (2), 410-414.
130. Gupper, A.; Chan, K. L. A.; Kazarian, S. G. "FT-IR imaging of solvent-induced crystallization in polymers." *Macromolecules* **2004**, 37, (17), 6498-6503.
131. Gowd, E. B.; Nair, S. S.; Ramesh, C.; Tashiro, K. "Studies on the clathrate (delta) form of syndiotactic polystyrene crystallized by different solvents using Fourier transform infrared spectroscopy." *Macromolecules* **2003**, 36, (19), 7388-7397.
132. Tashiro, K.; Ueno, Y.; Yoshioka, A.; Kobayashi, M. "Molecular mechanism of solvent-induced crystallization of syndiotactic polystyrene glass. 1. Time-resolved measurements of infrared/Raman spectra and X-ray diffraction." *Macromolecules* **2001**, 34, (2), 310-315.

133. Yoshioka, A.; Tashiro, K. "Thermally- and solvent-induced crystallization kinetics of syndiotactic polystyrene viewed from time-resolved measurements of infrared spectra at the various temperatures (1) estimation of glass transition temperature shifted by solvent absorption." *Polymer* **2003**, 44, (21), 6681-6688.
134. Menon, V. P.; Lei, J. T.; Martin, C. R. "Investigation of molecular and supermolecular structure in template-synthesized polypyrrole tubules and fibrils." *Chemistry of Materials* **1996**, 8, (9), 2382-2390.
135. Demoustier-Champagne, S.; Stavaux, P. Y. "Effect of electrolyte concentration and nature on the morphology and the electrical properties of electropolymerized polypyrrole nanotubules." *Chemistry of Materials* **1999**, 11, (3), 829-834.
136. Cepak, V. M.; Martin, C. R. "Preparation of polymeric micro- and nanostructures using a template-based deposition method." *Chemistry of Materials* **1999**, 11, (5), 1363-1367.
137. Arinstein, A.; Burman, M.; Gendelman, O.; Zussman, E. "Effect of supramolecular structure on polymer nanofibre elasticity." *Nature Nanotechnology* **2007**, 2, (1), 59-62.
138. Aleshin, A. N. "Polymer nanofibers and nanotubes: Charge transport and device applications." *Advanced Materials* **2006**, 18, (1), 17-27.
139. Zhu, L.; Xu, Y. Y.; Yuan, W. Z.; Xi, J. Y.; Huang, X. B.; Tang, X. Z.; Zheng, S. X. "One-pot synthesis of poly(cyclotriphosphazene-co-4,4'-sulfonyldiphenol) nanotubes via an in situ template approach." *Advanced Materials* **2006**, 18, (22), 2997-3000.
140. Cho, S. I.; Kwon, W. J.; Choi, S. J.; Kim, P.; Park, S. A.; Kim, J.; Son, S. J.; Xiao, R.; Kim, S. H.; Lee, S. B. "Nanotube-based ultrafast electrochromic display." *Advanced Materials* **2005**, 17, (2), 171-175.
141. Mulvihill, M. J.; Rupert, B. L.; He, R. R.; Hochbaum, A.; Arnold, J.; Yang, P. D. "Synthesis of bifunctional polymer nanotubes from silicon nanowire templates via atom transfer radical polymerization." *Journal of the American Chemical Society* **2005**, 127, (46), 16040-16041.
142. Lehmus, P.; Rieger, B. "Perspectives: Polymer chemistry - Nanoscale polymerization reactors for polymer fibers." *Science* **1999**, 285, (5436), 2081-2082.
143. Kageyama, K.; Tamazawa, J.; Aida, T. "Extrusion polymerization: Catalyzed synthesis of crystalline linear polyethylene nanofibers within a mesoporous silica." *Science* **1999**, 285, (5436), 2113-2115.
144. Tudor, J.; O'Hare, D. "Stereospecific propene polymerisation catalysis using an organometallic modified mesoporous silicate." *Chemical Communications* **1997**, (6), 603-604.

145. Tajima, K.; Ogawa, G.; Aida, T. "Novel molecularly hybridized polyethylene/silica composite materials: Polymerization of ethylene with supported titanocenes by mesoporous silicates." *Journal of Polymer Science Part a-Polymer Chemistry* **2000**, 38, 4821-4825.
146. Ye, Z. B.; Zhu, S. P.; Wang, W. J.; Alsyouri, H.; Lin, Y. S. "Morphological and mechanical properties of nascent polyethylene fibers produced via ethylene extrusion polymerization with a metallocene catalyst supported on MCM-41 particles." *Journal of Polymer Science Part B-Polymer Physics* **2003**, 41, (20), 2433-2443.
147. Nakajima, H.; Yamada, K.; Iseki, Y.; Hosoda, S.; Hanai, A.; Oumi, Y.; Teranish, T.; Sano, T. "Preparation and characterization of polypropylene/mesoporous silica nanocomposites with confined polypropylene." *Journal of Polymer Science Part B-Polymer Physics* **2003**, 41, (24), 3324-3332.
148. Lee, S. B.; Mitchell, D. T.; Trofin, L.; Nevanen, T. K.; Soderlund, H.; Martin, C. R. "Antibody-based bio-nanotube membranes for enantiomeric drug separations." *Science* **2002**, 296, (5576), 2198-2200.
149. Turunen, J. P. J.; Venäläinen, T.; Suvanto, S.; Pakkanen, T. T. "Novel use of mesoporous aluminas as supports for Cp_2ZrCl_2 and Cp^*ZrMe_3 : ethylene polymerization and formation of polyethylene nanofibers." *Journal of Polymer Science Part a-Polymer Chemistry* **2007**, 45, (17), 4002-4012.
150. Mitchell, D. T.; Lee, S. B.; Trofin, L.; Li, N. C.; Nevanen, T. K.; Soderlund, H.; Martin, C. R. "Smart nanotubes for bioseparations and biocatalysis." *Journal of The American Chemical Society* **2002**, 124, (40), 11864-11865.
151. Son, S. J.; Reichel, J.; He, B.; Schuchman, M.; Lee, S. B. "Magnetic nanotubes for magnetic-field-assisted bioseparation, biointeraction, and drug delivery." *Journal of The American Chemical Society* **2005**, 127, (20), 7316-7317.
152. Son, S. J.; Lee, S. B. "Controlled gold nanoparticle diffusion in nanotubes: Platform of partial functionalization and gold capping." *Journal of The American Chemical Society* **2006**, 128, (50), 15974-15975.
153. Li, F. Y.; Zhang, L.; Metzger, R. M. "On the growth of highly ordered pores in anodized aluminum oxide." *Chemistry of Materials* **1998**, 10, (9), 2470-2480.
154. Nair, S.; Naredi, P.; Kim, S. H. "Formation of high-stress phase and extrusion of polyethylene due to nanoconfinements during Ziegler-Natta polymerization inside nanochannels." *Journal of Physical Chemistry B* **2005**, 109, (25), 12491-12497.
155. Huang, B.; Cao, K.; Li, B. G.; Zhu, S. P. "Syndiospecific styrene polymerization with $\text{CpTiCl}_3/\text{MAO}$: Effects of the order of reactant addition on polymerization and polymer properties." *Journal of Applied Polymer Science* **2004**, 94, (4), 1449-1455.

156. Turunen, J. P. J.; Haukka, M.; Pakkanen, T. T. "Cocatalyst-originated aluminum residues in fibrous, very high molar mass polyethylene." *Journal of Applied Polymer Science* **2004**, 93, (4), 1812-1815.
157. Dong, X. C.; Wang, L.; Wang, W. Q.; Yu, H. J.; Wang, J. F.; Chen, T.; Zhao, Z. R. "Preparation of nano-polyethylene fibers and floccules using MCM-41-supported metallocene catalytic system under atmospheric pressure." *European Polymer Journal* **2005**, 41, (4), 797-803.
158. Gowd, E. B.; Shibayama, N.; Tashiro, K. "Structural changes in thermally induced phase transitions of uniaxially oriented delta(e) form of syndiotactic polystyrene investigated by temperature-dependent measurements of X-ray fiber diagrams and polarized infrared spectra." *Macromolecules* **2006**, 39, (24), 8412-8418.
159. Wang, C.; Hsu, Y. C.; Lo, C. F. "Melting behavior and equilibrium melting temperatures of syndiotactic polystyrene in alpha and beta crystalline forms." *Polymer* **2001**, 42, (20), 8447-8460.
160. Wang, C.; Cheng, Y. W.; Hsu, Y. C.; Lin, T. L. "Lamellar morphology and equilibrium melting temperature of syndiotactic polystyrene in beta-crystalline form." *Journal of Polymer Science Part B-Polymer Physics* **2002**, 40, (15), 1626-1636.
161. Wang, C.; Chen, C. C.; Hung, C. H.; Lin, K. S. "Lamellar morphologies and crystal stability of syndiotactic polystyrene in alpha-crystalline form." *Polymer* **2004**, 45, (19), 6681-6689.
162. Crank, J.; Park, G. S., *Diffusion in polymers*. Academic Press: London, New York, 1968; p xii, 452 p.